Characteristics of Gravity Waves in the Middle Atmosphere Revealed with the MU Radar, Rocketsondes and Lidars

by

Yasuhiro Murayama

January, 1993

Characteristics of Gravity Waves in the Middle Atmosphere Revealed with the MU Radar, Rocketsondes and Lidars

by

Yasuhiro Murayama

January, 1993

Acknowledgements

The author wishes to express his sincere appreciation to Professor Shoichiro Fukao for his guidance and supervision in the present work, and for the careful reading of the manuscript. The author also wishes to express his hearty gratitude to Emeritus Professor Susumu Kato for his comments, advice and encouragement regarding the present work. The author deeply thanks Professors Iwane Kimura and Hiroshi Matsumoto for their helpful advice and suggestions for the present work.

Special thanks are due to Dr. Toshitaka Tsuda for a number of stimulating discussions, and his kind guidance and continuous encouragement throughout the present work, and for careful reading of the manuscript.

The MU radar belongs to and is operated by the Radio Atmospheric Science Center, Kyoto University. The countless efforts to maintain and operate the MU radar of all the staff of the center and the operators from Mitsubishi Electric Corporation are gratefully acknowledged.

The author is indebted to Dr. K.-I. Oyama of the Institute of Space and Astronautical Science for the meteorological rocket experiments at the Kagoshima Space Center, Uchinoura. Professor D. Offermann of the University of Wuppertal coordinated the DYANA campaign, during which the rocket soundings were conducted. The rocket experiments at KSC were conducted in collaboration with ISAS and DLR (German Aerospace Research Establishments) during the DYANA campaign. The author is also indebted to Drs. M. Shiotani, H. Kanzawa and F. J. Schmidlin for their collaboration regarding the campaign and their comments.

The author thanks Dr. H. Nakane and the staff of the National Institute for Environmental Studies for the Rayleigh lidar observations, for kindly providing the obtained data and for the helpful comments on the data processing. Dr. R. Wilson is warmly thanked for the helpful comments, and a number of discussions on the lidar data treatment and gravity wave analyses.

The author is grateful to Drs. Takehiko Aso and Mamoru Yamamoto, who carefully read the manuscript, and gave comments and encouragement. The helpful comments of and discussions on gravity wave analyses with Drs. T. E. VanZandt and Kaoru Sato are warmly acknowledged. The author thanks Drs. Toru Sato and Manabu D. Yamanaka for the comments on the rocketsonde data analysis as well as the useful discussions, and also Dr. Takuji Nakamura for the discussions on the gravity wave analyses and his technical support. The author thanks Dr. T. Takami, and Messrs. T. Adachi, M. Tsutsumi and H. Hashiguchi for the helpful discussions and their technical support regarding computer software.

Part of the computations in the present work was performed at the Data Processing Center, Kyoto University. Part of the present work was supported by Grant-aid for JSPS Fellows.

Abstract

This thesis is devoted to the observational study of gravity wave characteristics in the middle atmosphere (from 10 to 100 km), as revealed by observations with the MU radar at Shigaraki (35°N, 136°E), combined with nearby rocketsonde experiments at Uchinoura (31°N, 131°E), and Rayleigh lidar measurements at the National Institute for Environmental Study, Tsukuba (36°N, 140°E), as complementary observations.

For maintenance of the realistic general circulation and temperature distribution in the middle atmosphere, momentum deposition due to gravity wave breaking was theoretically predicted to play an important role, which has stressed the importance of observational studies on gravity waves. As a wave dissipation process, the saturation of gravity waves has been proposed, which is considered to contribute to breaking of the waves and consequently to the mean flow acceleration. A spectrum model of saturated gravity waves has been further proposed, which explains previous observations.

The MU radar and rocketsonde observations showed an increase with height in the vertical scale and amplitude of dominant gravity waves, which can be understood from gravity wave saturation. Vertical wavenumber spectra of horizontal winds showed that the spectral shape was gradual in the lower stratosphere, became steeper with increasing height and then agreed with the saturated spectrum model with a slope value of –3 in the upper mesosphere. Wind velocity variance obtained from integration of the spectra increased with altitude in the stratosphere and lower mesosphere, and was as large as the saturation model value in the upper mesosphere. It is suggested that gravity waves are not fully saturated in the stratosphere, while in the mesosphere they are well described by the saturation model.

Detailed investigation of vertical profiles of the wind velocity variance was conducted. The variance generally increased with altitude in the stratosphere, diminished just above the stratopause, and greatly increased again in the lower mesosphere. Mean variance profiles in the upper mesosphere indicated fairly constant values, implying that wave amplitudes were restricted by the wave saturation. The kinetic energy of gravity waves per unit volume, that was deduced from the variance, decreased with altitude in the stratosphere and upper mesosphere, while it was fairly constant just above the stratopause, indicating that the wave dissipation may not be significant there.

We presented climatological results pertaining to spectra of the wave-induced wind field observed with the MU radar. Monthly frequency spectra were obtained in both the troposphere–lower stratosphere and the mesosphere. The spectral shape for stratospheric vertical winds was flat in summer and steep with negative values in winter, while the spectral density tended to be small and large in summer and winter, respectively. The mesospheric spectra showed

a flat slope and smaller density at the equinoxes, but a steep slope and larger density at the solstices. The spectral slopes for vertical winds in both height ranges became steeper as the mean wind intensity increased, likely because of the Doppler shifting of gravity waves due to the mean wind. The slopes of oblique wind spectra seemed nearly constant ($-5/3$) throughout a year in both height ranges.

Every monthly spectrum vs. vertical wavenumber in the mesosphere was shown to agree well with the saturated spectrum model, suggesting gravity wave saturation throughout the year in the mesosphere. In a case study in August, saturated gravity waves in the lower stratosphere showed the dominant component at low frequency ($\sim$ 14 hr).

Seasonal variation of wind velocity variance with periods of 5 min–2 hr in the mesosphere was observed with the MU radar, which showed semiannual variation with a persistent maximum in summer and a secondary peak in winter, and with equinoctial minima. Zonal momentum flux induced by gravity waves exhibited annual variation, being eastward and westward in summer and winter, respectively, while meridional flux showed no significant seasonal cycle. Typical zonal mean flow accelerations were eastward and westward in summer and winter, respectively, suggesting deceleration of mean zonal winds, which agreed with theoretical predictions.

The variance for the period range of 5 min–21 hr in the lower stratosphere showed clear annual variation with a maximum and a minimum in winter and summer, respectively, and coincided with that for the jet stream intensity, implying an important role of the jet in gravity wave excitation. The kinetic energy for the short period (5 min–2 hr) range was enhanced near the mean wind peak height ($\sim$ 12 km). The long period (2–21 hr) component showed clear annual variation with winter maxima in the middle troposphere and lower stratosphere, which was larger within the troposphere, likely implying wave excitation in the troposphere. Analysis of vertical wind fluctuations suggested that these long period waves may be Doppler shifted in the lower stratosphere in winter. The negative zonal momentum flux in the lower stratosphere implied that the upward propagating gravity waves mostly traveled westward, while no significant seasonal variation for meridional flux.

From Rayleigh lidar observations at Tsukuba, the potential energy of gravity waves was obtained in the upper stratosphere and lower mesosphere, which suggested an annual cycle with a winter maximum in the upper stratosphere. The mean values at Tsukuba reasonably well agreed with the lidar results at two observation sites in France, which were previously published, although the Tsukuba results (at 36°N) tended to be slightly larger than those in France (at 40°N).

Contents

List of Figures

List of Tables

Chapter 1

General Introduction

1.1 The Middle Atmosphere

The earth's atmosphere is a spherical gaseous layer surrounding the earth, which is divided into four layers according to the vertical structure of the atmospheric temperature (Fig. 1.1).

The lowest part is the troposphere, where the temperature decreases with altitude at a nearly constant lapse rate of about 6.5 K/km. Various meteorological phenomena occurring in this region greatly affect the environment of humans. The decrease in temperature ceases at the tropopause, which is located at 10–15 km, depending on the latitude and season.

The stratosphere exists above the tropopause, where the temperature increases with altitude up to about 45–50 km. The upper limit of the stratosphere is called the stratopause, corresponding to a local maximum of the temperature profile caused by the absorption of solar ultraviolet (UV) radiation in the ozone layer. The temperature again decreases in the height region above the stratopause, which is called the mesosphere. The minimum temperature is detected at the mesopause height of around 90 km. The thermosphere lies above the mesopause, where the temperature of the neutral atmosphere rapidly increases because of the absorption of solar extreme ultraviolet radiation and X-rays.

The region consisting of the stratosphere, mesosphere and lower thermosphere (∼10–110 km) is called the middle atmosphere. In the middle atmosphere, we can find many kinds of wind motions with various spatial and time scales, such as general circulations, planetary waves, tides, gravity waves, and turbulence. The most important heat source in this region is the ozone layer, which forms warmer and cooler poles around the stratopause in summer and winter, respectively.

The general circulations in the troposphere and middle atmosphere are un-

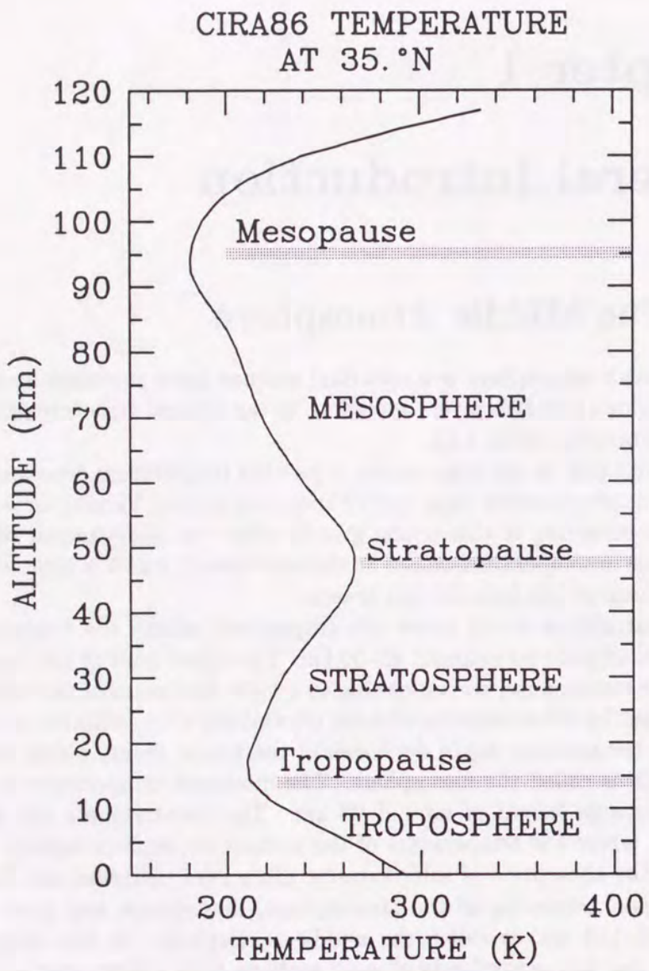

Figure 1.1: Vertical profile of annual mean temperature of the earth's atmosphere at 35°N [CIRA, 1986].

derstood to be principally thermally driven by solar heating. From observations, significant seasonal and meridional variations were inferred in the net radiative heating that mainly arises from the difference between the heating due to solar radiation and infrared emission. Correspondingly, the temperature and wind circulation show large seasonal and meridional variability.

The observed distribution of the zonal mean temperature in January is shown in Fig. 1.2a, the data being taken from CIRA (COSPAR International Reference Atmosphere) 1986. In the troposphere, temperature is highest, with a value of about 300 K, at the tropical surface, because the heating due to the incoming solar radiation is maximum in the equatorial surface region. The equatorial tropopause, being less than 200 K, is cooler than both the polar ones, which is thought to be due to the adiabatic expansion due to the tropical convective upward flow. From the ground up to the height of about 10 km, the temperature decreases monotonously from the equator toward both poles, and roughly speaking, the meridional gradient seems symmetric with respect to the equator. On the other hand, an antisymmetric temperature distribution is found in the middle atmosphere. We notice that temperature at the stratopause height (∼50 km) monotonously increases from the north (winter) pole of about 250 K to the south (summer) pole in excess of ∼280 K, as can be predicted from the solar heating in the ozone layer. However, at the mesopause height (∼80–90 km) it decreases from the winter (∼210 K) to the summer pole (∼140 K), reversing the meridional gradient above 70 km.

The zonally averaged zonal wind velocity of CIRA 1986 in Fig. 1.2b indicates two different jet steam structures in the troposphere and middle atmosphere in each hemisphere. The troposphere jets in the northern and southern hemispheres are always eastward, which are located over latitudes centered at 30°N and 40°S with stronger and weaker intensities, respectively.

In the middle atmosphere, the eastward and westward winds are dominant in winter and summer, respectively, at middle latitudes. The zonal wind amplitude increases with altitude up to 50–70 km. This wind structure exhibits the reversal of the sign of the vertical shear there, and decreases with altitude to form the weak wind layer near the mesopause height (about 80–90 km). Above the mesopause, the wind direction conversely becomes westward and eastward in winter and summer, respectively.

These wind systems can principally be understood as being connected to the meridional distribution of temperature by the thermal wind relation. The hemispheric symmetry and antisymmetry of the zonal circulations in the troposphere and middle atmosphere, respectively, in Fig. 1.2b can be recognized to coincide with those of the meridional gradient of temperature in Fig. 1.2a. However, despite the consistency between the temperatures and zonal winds, peculiar fea-

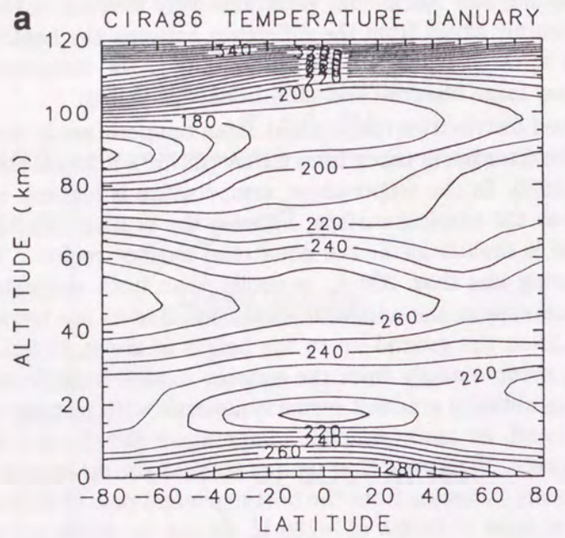

Figure 1.2: Height-latitude cross section of zonal mean (a) temperature in K and (b) eastward wind velocity in ms^{-1} in January, taken from CIRA 1986. Positive latitudes are in the northern hemisphere.

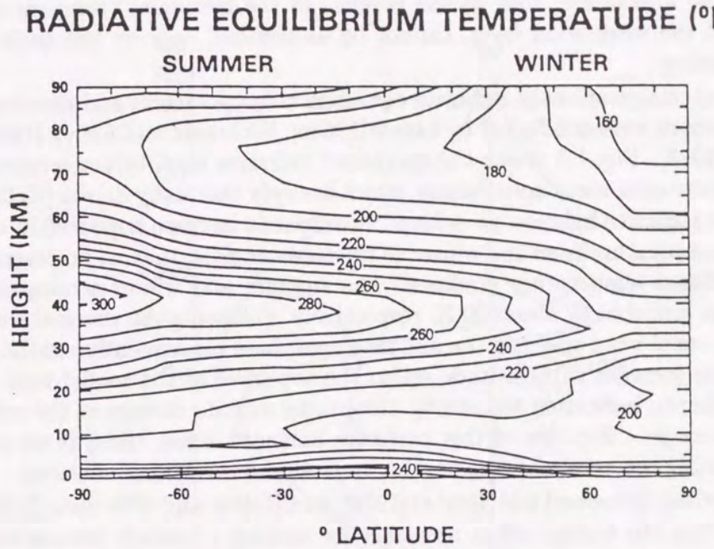

Figure 1.3: Radiative equilibrium temperature (top) and zonal wind (bottom) (after Geller [1983]).

tures near the mesopause, such as the reversal of the meridional temperature gradient and the weak wind layer, cannot be understood only on the basis of the solar heating.

Numerical computations of radiative equilibrium temperatures and accompanying zonal winds were conducted by Leovy [1964a], Wehrbein and Leovy [1982], and Geller [1983]. Fig. 1.3 shows the computed radiative equilibrium temperatures and geostrophic mean zonal winds, which are only thermally driven [Geller, 1983]. In the radiative balance, an evident monotonous increase appeared in the mesopause temperature from the winter to the summer pole, that is, no reversal of the meridional temperature gradient. The summer and winter stratopause was too warm and cool by about 20 K, respectively. Following the thermal wind relation, the zonal wind speed in the middle atmosphere consequently exhibited a monotonous increase with altitude up to the top level of the model field in both hemispheres, indicating too strong amplitudes and no closure of the middle atmosphere jet. Because of this perfectly balanced state, there is no net radiative heating, no accelerations, and no vertical and meridional motions.

Leovy [1964b], Schoeberl and Strobel [1978], and Holton and Wherbein [1980] pointed out that the lacking effect necessary for making a realistic atmosphere was a dynamical process of zonal momentum dissipation. They introduced the Rayleigh friction term as a body force for deceleration of the zonal mean flow, but that term was just a mathematical formulation and not based on any physical consideration.

Employing this Rayleigh drag, they could successfully obtain a more realistic atmosphere, showing, for instance, the reversal of the meridional temperature gradient and the weak zonal wind layer near the mesopause. The cold summer and warm winter mesopauses could be understood as manifestations of adiabatic expansion cooling and compression heating due to the upward and downward vertical motions, respectively, in the polar mesosphere. They were accompanied by meridional winds from the summer toward the winter pole at the mesopause height.

The deceleration of the zonal mean wind was found to be crucial for the middle atmosphere circulation to obtain the realistic features of temperatures and winds. Giving the physical mechanism of zonal wind deceleration introduced in the previous models as Rayleigh friction, Lindzen [1981], Holton [1982], and Matsuno [1982] proposed the deposition of vertical flux of horizontal momentum associated with the breaking of internal gravity waves.

Matsuno [1982] introduced internal gravity waves that are excited in the troposphere and propagate upward with an isotropic spectrum for the horizontal propagation direction. Also, using the eddy diffusion coefficient, he achieved realistic middle atmosphere circulation in his model. Fig. 1.4 shows the simu-

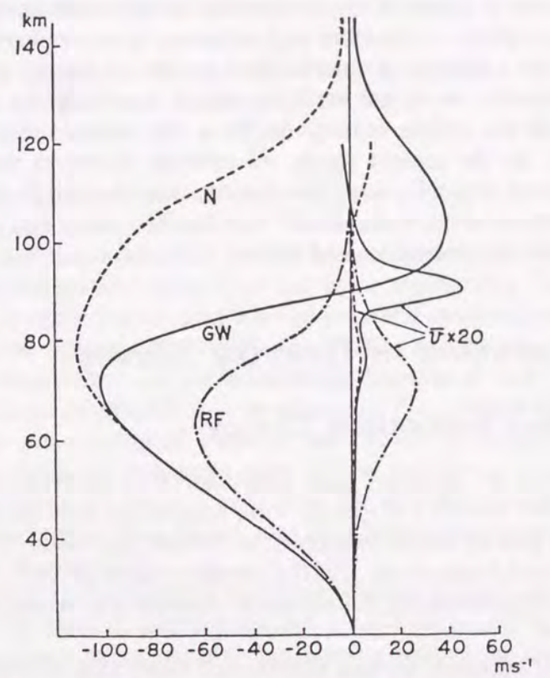

Figure 1.4: Vertical profiles of simulated zonal and meridional wind velocity at the summer solstice for three different cases, which included the effect of only eddy viscosity (N), only Rayleigh friction (RF), and gravity wave breaking and eddy viscosity (GW) (after Matsuno [1982]).

lated profile of wind velocity for three cases with the effect of only eddy viscosity (N), only Rayleigh friction (RF), and gravity wave breaking and eddy viscosity (GW). For case (N), the strongest amplitude of zonal winds appeared even in the thermosphere, while reasonable zonal winds with a closed jet stream and a weak wind layer above 80 km were found for case (RF), although the westward wind did not reverse toward the eastward direction, vanishing in the thermosphere. Only in case (GW), including the acceleration due to the convergence of wave-induced momentum flux, did the zonal wind show the closure of the jet stream with a weak wind layer around 85 km and further the reversal of the wind direction in the lower thermosphere, as found in observations such as CIRA 1986.

The theoretical studies to date predicted a very important role of internal gravity waves in terms of the momentum budget and energy transport in the middle atmosphere. Coinciding with advances in atmospheric measurement techniques, so far a number of observational studies on gravity waves have been conducted. However, we do not yet have enough knowledge on the behavior of gravity waves in the middle atmosphere for a full understanding of the global wind motions. In the present thesis, we attempt to reveal the seasonal and altitude variations of gravity wave characteristics in the middle atmosphere, using wind and temperature observations with the MU radar and complementary techniques such as rocketsondes and lidars.

1.2 Saturation of Gravity Waves

1.2.1 Linear Saturation Theory

In this subsection, we introduce basic equations of the gravity wave, and briefly describe the basic concepts of gravity wave saturation, and the saturated spectrum model of gravity waves developed by Dewan and Good [1986] (hereafter called DG86), and Smith et al. [1987] (hereafter called SFV87). Subsequently, some different approaches to the saturated spectrum in recent papers will be briefly reviewed.

Assuming an adiabatic inviscid process and small scale motions, the perturbation equations for atmospheric motions can be derived from the fundamental equations for the atmospheric dynamics such as the equation of motion, first law of thermodynamics, continuity equation and equation of state for an ideal gas. To a good approximation, inertial effects are not important and motions can be taken to be two-dimensional, for example, in an x-z plane. Assuming that a gravity wave is a plane wave, we can derive the dispersion relation of a gravity wave when $f^2 < \omega^2 < N^2$, as follows:

$$m^2 \approx \frac{N^2 - \omega^2}{\omega^2 - f^2} k^2 \tag{1.1}$$

where N and f are the Brunt-Väisälä and inertial frequencies, respectively, and ω is the intrinsic frequency of the wave (frequency observed in the frame moving with the background flow), which can be written as $\omega = k(c - \overline{u})$, where c and $\overline{u}$ are the horizontal phase velocity of the gravity wave and horizontal mean wind speed in the direction of wave propagation, respectively. m and k represent the vertical and horizontal wavenumbers.

The polarization equations among the variables of gravity waves can be derived from the basic equations as follows:

$$v' = -i\frac{f}{\omega}u' \tag{1.2}$$

$$w' = \frac{k}{m}u' \tag{1.3}$$

$$\theta' = -i\frac{k}{m\omega}\frac{\partial\overline{\theta}}{\partial z}u' \tag{1.4}$$

where u' and v' are the parallel and perpendicular components of wave-induced horizontal wind fluctuations relative to the wave propagation direction, w' is the wave-induced vertical wind, and θ is the potential temperature. The prime ($'$) and the overbar denote the perturbation and mean quantities, respectively. Equation (1.2) shows that the phase difference between u' and v' is 90°, and that the ratio of the amplitudes is proportional to f/ω, indicating that the tip of the horizontal wind vector of a gravity wave draws an elliptical locus, and that the gravity wave is a transverse wave. Phase and group velocities derived from these equations show that a gravity wave has downward phase velocity and upward group velocity simultaneously, that is, it transports energy upward with downward phase propagation.

Owing to exhaustive theoretical and observational studies, our understanding of the gravity wave characteristics has greatly increased in the last few decades, the consensus being reached that a major part of the meso-scale wind fluctuations in the middle atmosphere can be interpreted as superposition of many gravity waves. In order to describe the complicated structures of the fluctuations caused by the superposed waves, VanZandt [1982] introduced model spectra satisfying the linear dispersion relations of gravity waves, which were originally proposed for oceanic gravity wave observations [Garrett and Munk, 1975; Pinkel, 1981].

For instance, a vertical wavenumber spectrum of horizontal wind velocity can be expressed as

$$F_u(m/m_*) = C/[1 + (m/m_*)^t], \tag{1.5}$$

where m_* is the characteristic wavenumber, C is a constant, and t is the asymptotic logarithmic slope of the high wavenumber portion of the spectrum [Desaubies, 1976].

In observations of gravity wave spectra, the higher wavenumber portion exhibited that the spectral intensity and slope tend to be invariant, regardless of the meteorological conditions, season or place [e.g., Endlich and Singleton, 1969; Dewan et al., 1984; Vincent, 1984; Smith et al., 1985].

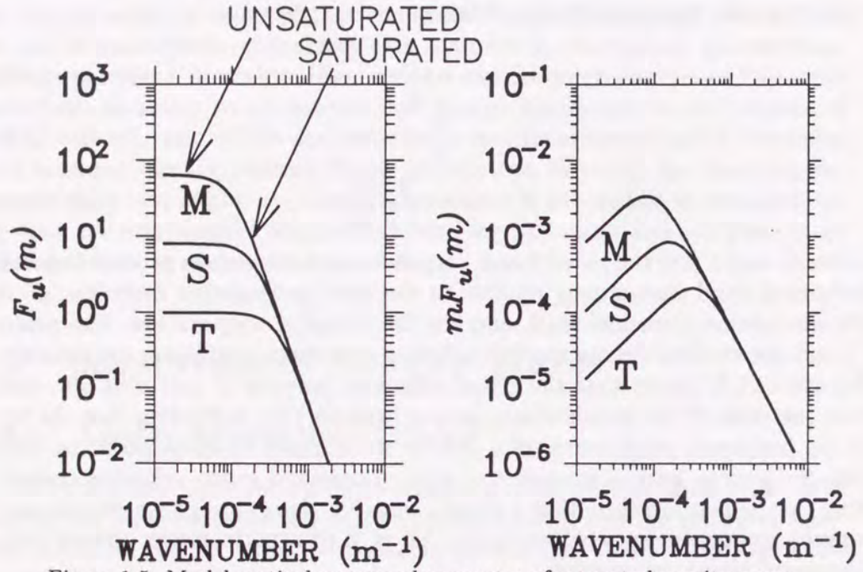

Figure 1.5: Model vertical wavenumber spectra of saturated gravity waves in normal (left) and energy content forms (right) [Smith et al., 1987]. The high wavenumber portion of the spectrum with a slope of -3 is thought to be caused by the saturated gravity waves, while the flat region is unsaturated. Three curves labeled 'T', 'S', and 'M' schematically represent spectra at lower, middle and higher altitudes, respectively.

As illustrated in Fig. 1.5, the logarithmic spectral slope was observationally estimated to have a value of around -3 for large wavenumbers, where gravity waves are thought to be saturated, while the spectrum is flat in the unsaturated range at smaller wavenumbers.

Spectrum Model of Saturated Gravity Waves

Based on the linear saturation theory for gravity waves, DG86 derived a saturated spectrum model vs. vertical wavenumber for wave-induced horizontal wind fluctuations, which obeys the wave amplitude limitation due to turbulence production associated with atmospheric instabilities [Hodges, 1967]. DG86, who firstly gave a physical explanation for the observed vertical wavenumber spectra, proposed the model assuming that 1) the observed spectra are understood to arise from a succession of gravity wave packets; 2) individual wave packets

are saturated individually, employing the concept of the breaking of a monochromatic wave; and 3) the band width of each wave packet is proportional to the center wavenumber.

Also employing these assumptions, SFV87 extended the argument of DG86, and developed a model considering the effect of superposition of many gravity waves. They both derived that the slope value of -3 for the saturated spectrum.

We briefly review derivation of the spectrum model following the description of SFV87. With a convective instability approach for superposition of many gravity waves, it is considered that the integration of the total gravity wave spectrum over all wavenumbers provides the vertical gradient value of the temperature field at the convective instability limit.

Convective instability for the total temperature field occurs for the superadiabatic state; $\theta_z < 0$, where θ is the potential temperature. The subscript z indicates the vertical derivative. When all the temperature fluctuations can be expressed as the sum of the sinusoidal waves, this convective instability limit leads to the relation between the variance of fluctuations and the mean of θ;

$$\frac{\overline{\theta_z^2}}{2} = \overline{\theta_z'^2}. \tag{1.6}$$

The variance of θ_z' on the right-hand side of (1.6) can be given as the integral of the vertical wavenumber spectrum over vertical wavenumber (m);

$$\frac{\overline{\theta_z^2}}{2} = \int F_{\theta z}(m)dm = \int m^2 F_\theta(m)dm = \int \frac{m^2\overline{\theta_z^2}}{pN^2} F_u(m)dm \tag{1.7}$$

where $F_{\theta z}(m)$, $F_\theta(m)$ and $F_u(m)$ are the one-dimensional spectra of θ_z, θ and horizontal wind velocity, respectively. p is the ratio of the kinetic to the potential energy of gravity waves.

They subsequently substituted the spectrum model used by VanZandt [1985] for $F_u(m)$ in (1.7), using the spectral slope of -3, and conducted integration to obtain the spectrum model for the saturated portion at higher wavenumbers $m \gg m_*$, as;

$$F_u^s(m) = \frac{N^2}{6m^3} \quad (m \gg m_*), \tag{1.8}$$

where m_* is the characteristic vertical wavenumber of the spectrum, and the value of p is taken to be $5/3$, which was empirically determined [Desaubies, 1976; VanZandt, 1982, 1985].

Here the underlying idea of the linear saturation theory is schematically illustrated. Figure 1.6 shows profiles of wind velocity, u, and vertical wind shear squared, $|\partial u/\partial z|^2$, for the two monochromatic gravity waves indicated by

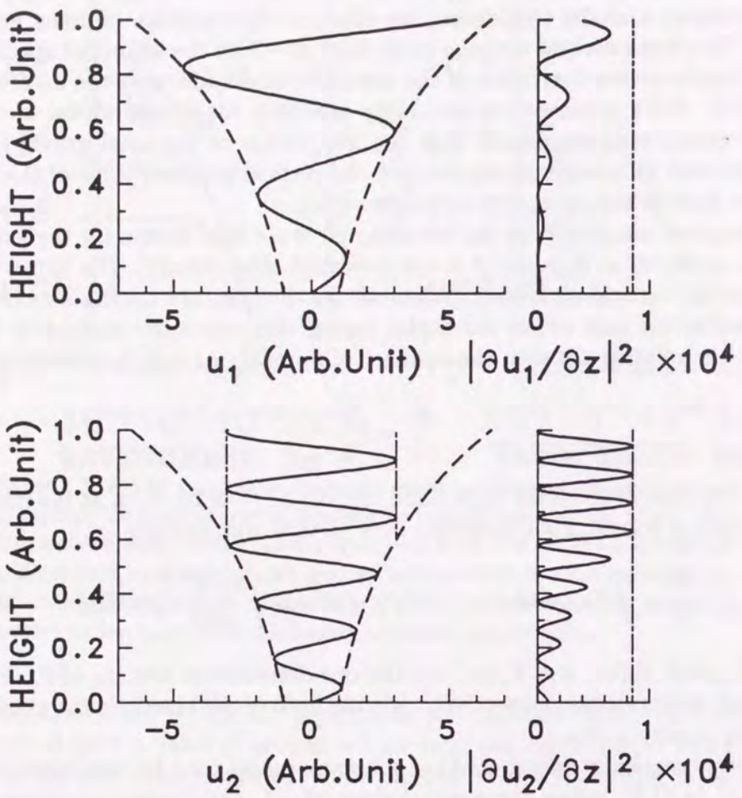

Figure 1.6: Schematic profiles of wind velocity, u, (left) and vertical wind shear squared, $|\partial u/\partial z|^2$, (right) for gravity waves with long (top) and short (bottom) vertical wavelengths, respectively. The dashed curve shows asymptotical growth of the wave amplitude due to the exponential decrease of the atmospheric density. Wave 2 is assumed to reach the saturation condition when $|\partial u/\partial z|^2$ becomes as large as the value indicated by the vertical chained line.

subscript numbers, 1 and 2, which correspond to waves with small and large vertical wavenumbers, m_1 and m_2, respectively. When gravity waves propagate upward, conserving their energy, both u_1 and u_2 increase similarly in proportion to $\exp(z/2H)$, where H is the density scale height in an isothermal atmosphere. On the other hand, $|\partial u/\partial z|^2$ increases as $[(1/2H)^2+m^2]\exp(z/2H)$. When $1/2H$ is much smaller than m, $|\partial u/\partial z|^2$ becomes proportional to m^2, so that the shear intensity becomes much larger for the wave with m_2 than that with m_1. An upward propagating wave becomes unstable when it reaches an altitude where the local stability becomes lower than some threshold. Since the atmospheric stability is inversely proportional to $|\partial u/\partial z|^2$, a wave with a larger m more easily becomes unstable. As a result, a wave with a larger m becomes unstable at lower altitudes and its amplitude remains at a constant value. Thus, the spectrum amplitudes for large wavenumbers are limited to saturated values, while those for unsaturated components increase as the altitude increases.

It is noteworthy that the energy content graph in Fig. 1.5 suggests that the wave component at the bend of the spectrum, which has just reached the saturation condition, exhibits the largest energy. In other words, such a component is most dominantly detected in the wind velocity profiles.

Figure 1.5 also predicts that the dominant vertical scale of gravity waves generally increases as they propagate upward. For example, if we assume an altitude difference of $5H$ between the lower stratosphere and the mesosphere, the wave amplitudes for an unsaturated component are expected to increase by a factor of $\exp(5H/2H) = 12.2$, that is, the spectral densities increase by a factor of $\exp(5H/H)$. In such a case, Fig. 1.5 suggests that the wavenumber corresponding to the bend of spectra decreases by a factor of $\exp(5H/3H) = 5.3$. These model predictions will be compared with the observed characteristics of gravity waves in Chapters 3 and 4.

Other Approaches to the Saturated Spectrum

Besides the arguments regarding the linear saturation theory, nonlinear wave-wave interaction is considered in theoretical studies of gravity wave saturation [e.g., Fritts, 1985; Weinstock, 1984, 1990; Hines, 1991a, b, c].

Studies on the gravity wave nonlinear process [e.g., Fritts, 1985; Weinstock, 1984] have been concentrated on the dissipation process associated with wave-wave interactions. Weinstock [1984] theoretically presented a vertical wavenumber spectrum of saturated gravity waves, but it resulted in too much elimination of short-vertical scale waves because his wave dumping was too strong. Weinstock [1990] improved his model and successfully derived a more realistic model including the saturated and unsaturated spectral portions.

Hines [1991a] considered that the three assumptions used by DG86 and SFV87 were controversial, although their models reasonably agree with observations. Hines [1991b] firstly proposed the non-dissipative wave-wave interaction to obtain the saturated spectrum model. He did not require dissipative nonlinearity but the advective nonlinear wave-wave interaction, where the small-scale (low intrinsic phase speed) waves are thought to be Doppler-shifted by the larger-scale gravity waves in the gravity wave spectrum, resulting in the Doppler-spread of the vertical wavenumber spectrum. On statistical treatment of many superposed waves, despite the crude approximation, the advective nonlinearity could successfully explain the slope of nearly -3 at high wavenumbers without a dissipative process, although dissipation with instabilities played a minor role there. However, as he noted, Hines's [1991b] model needs to be improved with more careful treatment of nonlinearity and dissipation.

1.2.2 A Brief Review of Gravity Wave Observations

It is now widely accepted that meso-scale wind fluctuations in the middle atmosphere are caused by gravity waves, which are mainly excited in the lower atmosphere due to, for example, the unstable behavior of and/or the interaction of the topography with a jet stream, and various meteorological disturbances such as fronts, typhoons, thunder storms and cumulonimbus convections.

Recently developed remote sensing techniques, such as the Mesosphere-Stratosphere-Troposphere (MST) radar, partial reflection (PR) radar and Rayleigh and resonance lidars, can monitor the middle atmosphere on the continuous basis with time and height resolutions of about 1–10 min and 0.1–2 km, respectively [e.g., Woodman and Guillén, 1974; Ecklund et al., 1979; Chanin and Hauchecorne, 1981]. Rocket sounding techniques employing light-weight payloads (datasonde and inflatable sphere) can provide wind velocity and temperature with good height resolution of tens meters–a few kilometers in the stratosphere and mesosphere [Bollermann, 1970; Schmidlin, 1986], although it is difficult to obtain temporally continuous data.

Evidence of quasi-monochromatic gravity waves have been observed by a number of authors [e.g., Rastogi and Bowhill, 1976; Sato and Woodman, 1982; Maekawa et al., 1984; Manson and Meek, 1988; Yamamoto et al., 1987, 1988b; Fritts et al., 1988;Tsuda et al., 1990a]. Quasi-monochromatic inertial gravity waves in the mesosphere observed with the MU and Poker Flat radars by Yamamoto et al. [1988b] and Fritts et al. [1988] indicated clear downward phase progressions, which were accompanied with the downward motion of strong echo region. They suggested turbulence production due to gravity waves, implying gravity wave saturation. In particular, Yamamoto et al. showed that convective

and dynamical instabilities might occurred associated with the dominant gravity waves, which showed plausible evidence of occurrence of the gravity wave saturation.

Also quasi-monochromatic gravity waves have been observed in the lower stratosphere by atmospheric radars [Sato and Woodman, 1982; Maekawa, et al., 1984; Fritts et al., 1988]. Fritts et al. conducted simultaneous observations with the MU radar and balloon sondes and concluded saturation of short vertical-scale (2–3 km) gravity waves in the lower stratosphere. Nevertheless, there appeared controversy about interpretation of the tropopausal and lower stratosphere gravity waves in recent studies on their characteristics [Maekawa et al., 1984; Hines, 1989; Cornish and Larsen, 1989].

Although dominant gravity waves are detected in the observed wind and temperature field, these profiles normally show complicated fluctuations, indicating superposition of many waves and therefore can best be examined by spectrum analysis [e.g., Dewan et al,1979; Balsley and Carter, 1982; Vincent, 1984; Meek et al., 1985; Smith et al, 1985; Tsuda et al., 1990a; Wilson et al., 1991a, b].

As for frequency spectrum of wind motions, the mesospheric wind spectra observed by Tsuda et al. [1990a] could be well explained by the gravity wave spectrum model by VanZandt [1985]. On the other hand, other observations reported serious discrepancy in shape and intensity with the model for the vertical wind component [e.g., Gage et al., 1986]. In order to understand the spectral shape deformation for vertical wind velocity, Scheffler and Liu [1986] and Fritts and VanZandt [1987] showed the spectrum model including the effect of the Doppler shifting of gravity waves due to the mean wind.

Fritts and Wang [1991] showed good agreement of the observed mesospheric spectra with the Doppler-shifted frequency spectrum model improved by themselves. VanZandt et al. [1991] reported that the variability of vertical wind spectrum shape in the troposphere and lower stratosphere over flat terrain could be understood from the Doppler-shifted gravity wave spectrum model. While, VanZandt et al. suggested the probability that the spectra observed near mountains may be enhanced in intensity and deformed in shape due to the effect of the topography.

Besides these case studies, climatological analyses based on long-term observations were conducted and revealed variability of gravity wave activity [Hirota, 1984; Meek et al., 1985; Vincent and Fritts, 1987; Wilson et al., 1991b; Senft and Gardner, 1991].

Using rocket sounding datasets at thirteen stations, Hirota [1984] showed seasonal and latitudinal variation of gravity wave activity in the height range of about 20–65 km. A seasonal cycle was annual at latitudes higher than about 30 °N and semiannual at lower latitudes centered around 20°N.

Seasonal variation was also studied by observations with the MF partial reflection (PR) radars [Meek et al., 1985; Ebel et al., 1987; Vincent and Fritts, 1987] and with Rayleigh and resonance Na lidars [Wilson et al., 1991b; Senft and Gardner, 1991]. A brief review of gravity wave climatology was made by Reid [1986]. In mesospheric results by Meek et al. [1985], Ebel et al. [1987], and Vincent and Fritts [1987] by means of radars, the variance of wave-induced horizontal winds tended to show semiannual and annual variation with maxima near solstices for the shorter and longer period components with wave periods less and more than a few hours, respectively, being regardless of latitude and technique.

While the observed wind velocity variance corresponds to the kinetic energy of gravity waves, the potential energy of gravity waves can be inferred from the atmospheric density or temperature. From density observations with Rayleigh lidars, Wilson et al. [1991b] estimated the potential energy of gravity waves with vertical scales less than 15 km, and revealed annual variation of the wave energy in the stratosphere while semiannual cycles in the mesosphere. From the mesospheric Na density observed with a resonance lidar, Senft and Gardner [1991] inferred the air density fluctuations due to gravity waves and showed semiannual variation of gravity wave activity.

Unlike the above statistical analyses of gravity wave climatology, Nakamura et al. [1993b] extracted dominant gravity wave components from mesospheric long-term observation with the MU radar. The variance of horizontal wind velocity of the dominant waves showed annual variation with maximum centered in September–October and minimum in January, which showed quite different from the statistical results.

Direct measurement of upward flux of horizontal momentum due to gravity waves with atmospheric radars became available through a technique developed by Vincent and Reid [1983]. Momentum flux is proportional to the difference between the radial wind velocity variances simultaneously obtained with two oblique antenna beams with the same zenith and opposite azimuthal angles.

Murphy [1990] estimated mesospheric momentum flux in January 1985–March 1986 over Adelaide. Positive values of the zonal component in summer, autumn and spring, while negative zonal flux in winter, only for the 8–60 min component, although no clear seasonal cycle appeared for the longer period components. His zonal mean flow acceleration seriously scattered in intensity and sign, although the acceleration in some cases seemed to be comparable to the Coriolis torque expected from observed meridional winds. Nakamura et al. [1993b] showed momentum flux of dominant gravity waves in the mesosphere observed with the MU radar. The zonal flux direction tended to be eastward and westward in summer and winter, respectively, and yet mean flow acceleration

was not shown in their analysis.

From the linear dispersion relation and the frequency spectrum model, Fritts [1984] suggested that the momentum flux induced by gravity waves is proportional to ω^{-p} (p is chosen to be, e.g., 5/3 or 2), which indicates that the fraction by waves with periods less than 2 hr is about 2/3 of the total flux. This reasonably agreed with the observation by Fritts and Vincent [1987], but further observations of the various frequency components are required for examination of the Fritts' suggestion. Another observation of mesospheric momentum flux by Nakamura et al. [1993a] showed that the component with the wave periods longer than tens minutes was rather dominant.

Excitation sources of gravity waves are said to be in the lower atmosphere due to the various disturbances in the troposphere and lower stratosphere. However little is known about characteristics of excitation sources of gravity waves, that is, intensity, temporal and spatial scales and variability of the sources, and spectrum of excited waves, and what is most responsible for forcing to the mesospheric winds through momentum transport. So it is thought to be necessary to observe and collect information on the gravity wave behaviors relevant to the processes which are possible wave sources.

A number of aircraft observations of wind velocity and temperature showed that the wind and temperature fluctuations were significantly larger over rough terrain than over ocean, where the determinations over flat terrain was intermediate values [Nastrom et al., 1987; Jasperson et al., 1990]. Using the same database, Nastrom and Fritts [1992] reported the variance over rough terrain with values over 50 times larger than flat terrain. Fritts and Nastrom [1992] classified the same data into five cases. The variance of winds and temperature were about 5–10 times larger for the determinations near topography, about 3–7 times larger near frontal, convective and jet stream, than the value in no source regions.

Chapter 2

Observational Techniques

2.1 The MU Radar

The MU (Middle and Upper atmosphere) radar is an ultra-sensitive VHF Doppler radar which detects echoes scattered by the refractive index fluctuations due to atmospheric turbulence in the troposphere and middle atmosphere as well as incoherent scattering echoes in the thermosphere. It was constructed in a hilly area at Shigaraki, Shiga prefecture, Japan (34°51'N, 136°06'E) [Fukao et al., 1985a, b]. The MU radar provides information of the atmospheric dynamics such as three-dimensional wind velocities and turbulence intensity in the troposphere and middle atmosphere in the height ranges of 2–25 and 60–90 km. It also have been contributed to the ionospheric studies in the height region of 100–400 km as an IS (Incoherent Scatter) radar.

The MU radar is a monostatic pulse Doppler radar at 46.5 MHz with maximum peak and average transmitting powers of 1 MW and 50 kW, respectively. A block diagram of the MU radar system is presented in Fig. 2.1 [Fukao et al., 1985a]. The MU radar employs an active phased array, which composes a circular array of 475 3-element crossed Yagi's, giving an antenna aperture of 8330 m^2. The one way half-power full width of the main beam is 3.7°. Each antenna element is connected to individual solid-state transceiver modules (TR modules), which are accommodated in six booths located surrounding the antenna array. Each TR module is equipped with a solid state transmitter, a receiver preamplifier, a T/R switch and a digital phase shifter. The whole antenna array is separated into 25 groups, each of which consisting of 19 antenna elements with the same number of TR modules. Two orthogonal linear, right and left handed circular polarizations are available. The band width of the transmitter is 1.65 MHz, permitting us to make the shortest pulse width of 1 μs, corresponding to the height resolution of 150 m.

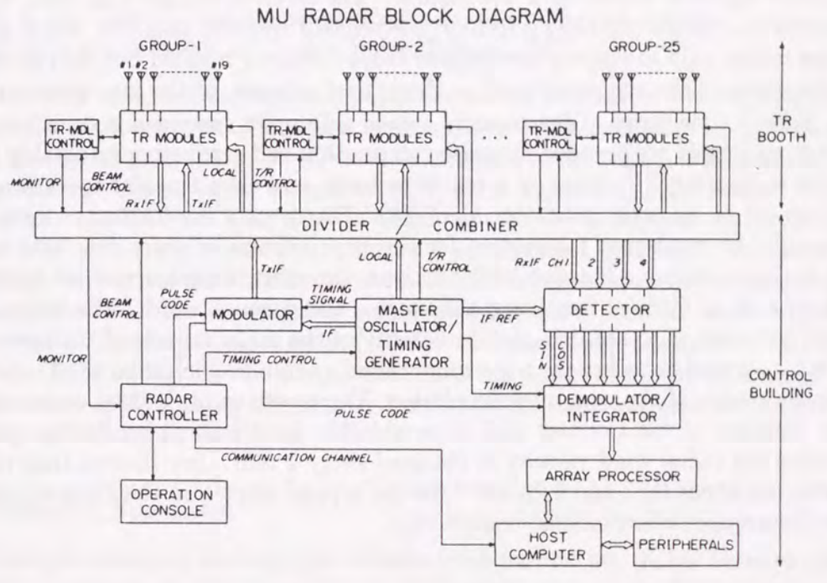

Figure 2.1: Block diagram of the MU radar system (after Fukao et al., [1985a]).

The circular array configuration with a diameter of 103 m makes nearly uniform side lobe level with respect to the azimuthal angle. The antenna element is located at the grid point of the equilateral triangular grid with the element spacing of 4.5 m, corresponding to 0.698 in radar wavelength. No grating lobes appear until the main lobe is steered in the direction at a zenith angle as large as 40°.

The MU radar observation is under full control of a system -installed computer. The MU radar is versatile in allowing us to steer the antenna beam in at most 256 directions that is chosen from 1657 directions within the zenith angle of 30°. The overall operation of the MU radar is supervised by a computer called a "radar controller", which is an engineering workstation HP9000/300. The radar controller sends observation parameters to the radar hardware, and also to a timing generator to control the pulse scheme. On the radar controller, we can easily change The various observation parameter such as height ranges, the number and directions of antenna beam, inter-pulse period (IPP) (2500 times a

second at maximum), and so on.

The received radar echoes are down-converted to the IF (Intermediate Frequency) signal at 5MHz by a TR module. The received signals from each TR module can be distributed up to four independent receiver channels, which enables us not only to employ the Doppler beam swinging method but also to use other observation techniques such as the spaced antenna, or the interferometry.

From a time series of the received signal, a Doppler spectrum is calculated. Received signals are decoded for pulse compression and are further integrated in order to improve S/N ratio on a real time basis, and then Doppler spectra are calculated by an array processor MAP-300. The spectra are further processed through the incoherent integration for the improvement of their detectability. By fitting a Gaussian function to the spectra, the spectral parameters are determined such as Doppler frequency, echo power and spectral width. The Doppler shift corresponds to the line-of-sight velocity of the mean motion of turbulence that is assumed to be frozen to the wind, therefore resulting in radial wind velocity. By means of the computer simulation, Yamamoto et al. [1988a] estimated the accuracy of the Doppler shift determination by the Gaussian fitting. Assuming the radial wind velocity is obtained every 1 min, they showed that the errors are about 0.12 and 0.20 ms^{-1} for the typical spectra in the stratosphere and mesosphere observations, respectively.

2.2 Spectral Analysis Techniques for the MU Radar Data

Since the MU radar can provide temporally and vertically continuous wind velocity data, spectral analysis can be applied to them with respect to frequency or vertical wavenumber. In the present work, we calculate these one dimensional spectra of wind velocity fluctuations observed with the MU radar. So in this section, we briefly describe the principle of the spectral analysis, as well as the data reduction procedures for the MU radar observations in the two height ranges in the troposphere–lower stratosphere and in the mesosphere. The same principle of the spectral analysis will be also applied to data obtained from rocketsondes and lidars, for calculation of vertical wavenumber spectra.

Spectrum Calculation

Power spectral densities are often calculated from the squared values of Fourier coefficients obtained through FFT (Fast Fourier Transform) of time or spatial series of data points. However, if the observed data series include missing values,

FFT cannot be directly applied to the data. Avoiding this difficulty, we applied the method stated by Blackman and Tukey [1959] to the observed data series with some missing data points in order to calculate the power spectral density. We briefly describe the spectrum calculation procedure employed in this work, following the principle of Blackman and Tukey [1959].

From a data series of a certain physical quantity in terms of time or altitude, an ACF (auto-correlation function) is calculated with a maximum lag that must be smaller than the number of the total samples of the series. The maximum lag must be chosen to be enough small to make no missing ACF value. After multiplying ACF with a lag window (Hanning window) to increase confidence of the ACF values, the power spectral density is calculated by using FFT. In computing the vertical wavenumber spectrum which is expected to vary over a large range, the data was prewhitened before calculating the ACF to make reliable estimates. The original data series $\{x_i\}$ becomes prewhitened data series $\{\tilde{x}_i\}$ by using the formula $\tilde{x}_i = x_i - \beta x_{i-1}$, where β is the degree of prewhitening, which was taken as 0.95. After the Fourier transform the spectrum was compensated for prewhitening by recoloring.

Frequency Spectrum

Although frequency spectra can be calculated for the MU radar observations both in the two height ranges in the mesosphere and in the troposphere and lower stratosphere, the data qualities were significantly different between them. So the data reductions for those height regions were slightly different despite the identical principle of derivation of the power spectral density.

For the observations in the troposphere and lower stratosphere, we calculated frequency spectra for each range gate (height resolution of 0.15 km) with a maximum lag of 400 data points (~period of 32 hr), discarding a spectrum if a data gap was more than 60% of the entire observation period for each range gate. The spectra were then averaged in a height region with a thickness of 1.5 km.

On the other hand, for the mesospheric observations with the MU radar, for eight–twelve hours each day, frequency spectra were calculated from time series of vertical and oblique wind velocities which were constructed in a layer with a thickness of 1km in the height region of 60-90km. Since mesospheric echoes are normally found in several vertically-separated regions, spectra were not necessarily determined in every height range. If more than 75% of the data points was missing from a layer, then that layer was excluded from the spectral analysis. The maximum lag of 25 was used for determining frequency spectra,

the prewhitening being not applied.

Vertical Wavenumber Spectrum

For the mesospheric observations, we obtained a vertical wavenumber spectrum after averaging the wind data every two hours at each height. Although we should remove the background wind which may include waves with periods of more than the inertial period (~21 hours at 35°N), we only subtracted a linear trend from the profile because it is difficult to correctly estimate mean winds from the mesospheric data which covers only for eight–twelve hours a day. We avoided computing a spectrum of the profile whose missing ratio exceeds 85%. The prewhitening was employed for the calculations of the vertical wavenumber spectra.

In the lower stratosphere and troposphere, unlike the mesospheric data, the MU radar can provide data without gap during night, so we could average the wind for more than 21 hr to obtain the mean wind velocity. We subtracted the mean wind from the total wind to extract the gravity wave component.

2.3 Rocketsonde

Although the MU radar can provide excellent data with good time and height resolutions in the troposphere and middle atmosphere, there exists a gap region (about 25–60 km) in its observable height range. Because of the lack of the air and electron density in this gap region, echo signal is too weak to be detected by the MU radar. So we need some complementary measurement techniques in the upper stratosphere and lower mesosphere in order to cover the whole height range of the middle atmosphere. In this section, we briefly describe the meteorological rocket sounding system, as a complementary technique of the MU radar observation, which provides data used for analyses in later chapters.

The meteorological rocket sounding system has been one of important techniques of *in situ* measurement of wind velocity and temperature in the middle atmosphere since its first attempt in the late 1940's and efforts for reducing costs and sizes in 1950's [e.g., Bollermann, 1970; Schimidlin, 1986]. Even after development of the sensitive VHF and UHF radars for the wind observation such as the MU radar, the rocket-borne measurement have remained the available and useful technique for the wind and temperature observations in the stratosphere and mesosphere [e.g., Smith and Fritts, 1984; Murayama et al., 1992a].

In this study we utilized rocketsonde data that were obtained at the Kagoshima Space Center of the Institute of Space and Astronautical Science (ISAS) at Uchinoura, Japan (31°15'N, 131°05'E). We employed three different kinds of the

rocket sounding systems; MT-135 and Super Loki equipped with datasondes and Viper with a falling sphere.

Datasonde Experiment (MT135 and Super Loki Systems)

Datasonde system is one of rocket-bourne sounding techniques, which the payload contains sensors to probe atmospheric parameters which

The MT-135 rocket system, which was developed in Japan, provides temperature and horizontal wind velocity at heights up to about 60–70 km. The configuration of the rocket MT-135 is schematically shown in Fig. 2.2a, whose body is mostly occupied by a solid-propellant rocket motor, and its nose cone provides a volume for the datasonde (Meisei Electric Co. Ltd.) which is equipped with a transponder and a temperature sensor. During the descend of the datasonde, it is decelerated by means of the cloth parachute.

Figure 2.3 shows a schematic illustration of the rocket sounding with a datasonde. A datasonde is ejected from a rocket at a top height (50–60 km for MT-135) that depends on the elevation angle of launching, total mass of the system, etc. The range and azimuthal and elevation angles of the descending datasonde is determined with a tracking radar on the ground. The tracking data result in the locations of the sonde during its descending, and further enable horizontal wind velocity as calculated from the velocity of the sonde. The temperature values that are measured by a sensor built in the sonde are transmitted to a ground station and are recorded there. The fundamental data-processing procedures for the rocketsonde experiments were described in detail by Bollermann [1970] and Schmidlin [1986].

For the MT-135 experiments, the tracking data are recorded on a magnetic tape every 100 ms. After averaging the tracking data for 1 s, the location of the datasonde was calculated in the Cartesian coordinate system, resulting in horizontal wind velocity delineated from the time derivatives of horizontal displacement of the sonde. The datasonde for MT-135 is equipped with a transponder that transmits the signal of the temperature measurement to the ground-station. The transmitted signal is received by the same facility as the tracking radar, and is recorded on a magnetic tape.

The Super Loki system, which were developed in USA, was equipped with a datasonde (Space Data Corp.) including a temperature sensor as well as the MT-135 system, being adjusted so as to reach the altitude up to about 73 km at maximum for the experiments at Uchinoura [Offermann et al., 1989]. The vehicle of Super Loki system shown in Fig. 2.2b is a two-stage rocket, which is composed of a portion of a propellant rocket motor (lower thick part) and

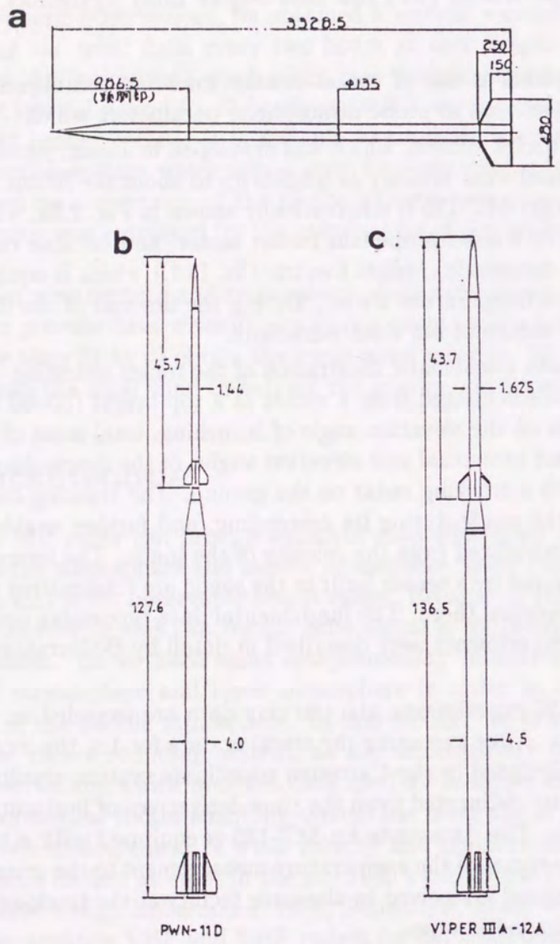

Figure 2.2: Configurations of the meteorological rockets of (a) MT-135 (units in mm), (b) Super Loki and (c) Viper (units in inches).

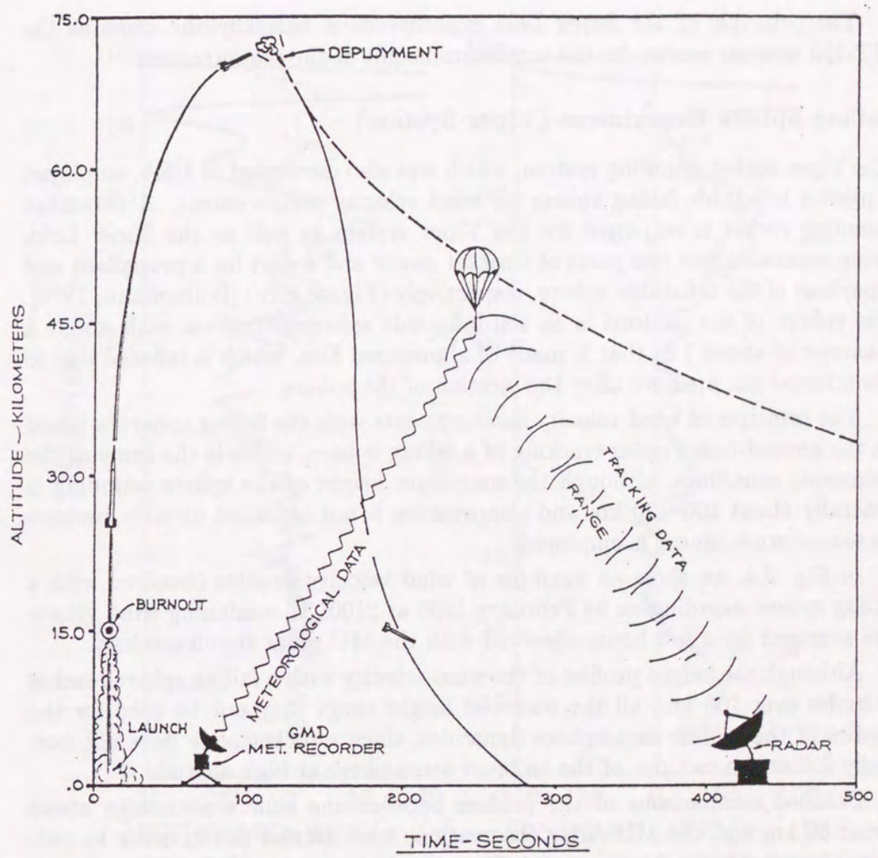

Figure 2.3: Schematic of meteorological rocket sounding system [after Bollermann, 1970].

a dart for a datasonde (upper thin part) [Bollermann, 1970]. The decelerator of the datasonde for the Super Loki system is a special parachute, a kind of the self-inflation parachute, which is called "Starute" that is made of partly metalized film and form the structure by means of the internal gas pressure after the payload ejection.

The principle of the Super Loki experiments is basically the same as the MT-135 system, except for the maximum height of the measurement.

Falling Sphere Experiment (Viper System)

The Viper rocket sounding system, which was also developed in USA, employed a passive inflatable falling sphere for wind velocity measurement. A two-stage sounding rocket is employed for the Viper system as well as the Super Loki, being separated into two parts of a rocket motor and a dart for a propellant and a payload of the inflatable sphere, respectively (Figure 2.2c) [Bollermann, 1970]. The sphere of the payload is an self-inflatable spherical balloon with about a diameter of about 1 m that is made of aluminized film, which is inflated due to the internal gas pressure after the ejection of the sphere.

The principle of wind velocity measurements with the falling sphere is based on the ground-based radar tracking of a falling sphere, which is the same as the datasonde soundings, although the maximum height of the sphere sounding is generally about 100–120 km and temperature is not obtained directly because no temperature sensor is employed.

In Fig. 2.4, we show an example of wind velocity profiles observed with a falling sphere sounding on 24 February 1990 at 2100LT, combining wind velocities averaged for a few hours observed with the MU radar simultaneously.

Although the height profiles of the wind velocity with a falling sphere reaches altitudes over 100 km, all the observed height range may not be used for the studies of the middle atmosphere dynamics, since a rocketsonde does not normally follow the motions of the ambient atmosphere at high altitude.

Detailed comparisons of the profiles between the sphere soundings above about 60 km and the MU radar observations were carried out in order to estimate the reliable height range and the measurement error of the falling sphere soundings [Murayama et al., 1992b].

The profiles of the sphere sounding in Fig. 2.4 were made after the low pass filtering with a cutoff period of 15 s on the time series of the record sampled every 1 s. The descending speed of the falling sphere exponentially decreases below about 80 km height with the altitude decreasing, which is, for example, as large as about 500 and 200 ms^{-1} at about 80 and 60 km altitudes, respectively. So the vertical resolution of the smoothed profile depends on the altitude, being

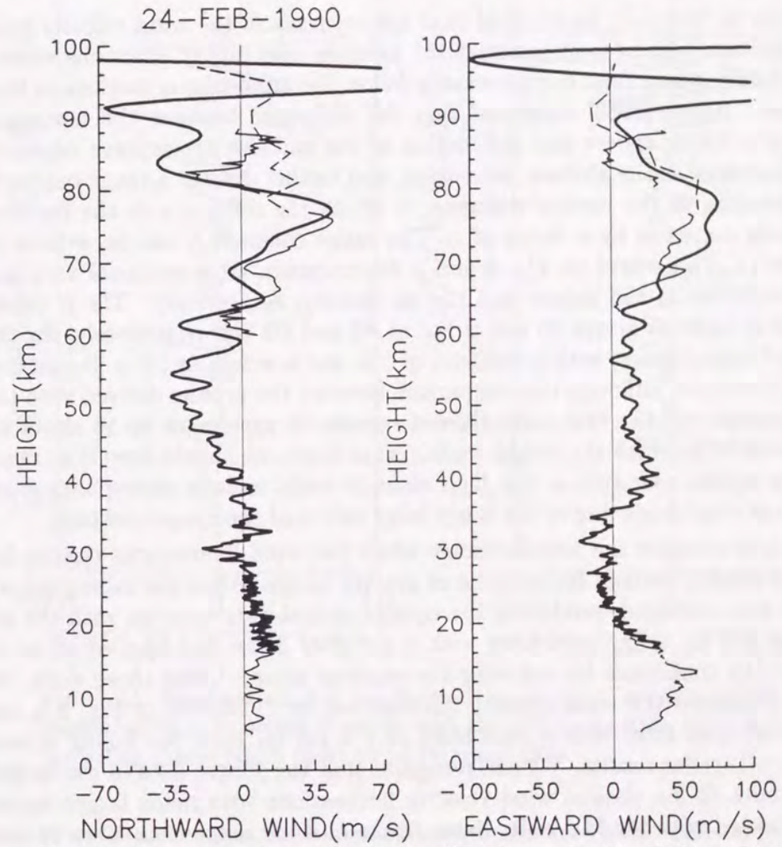

Figure 2.4: Horizontal wind velocity profiles observed with a falling sphere sounding on 24 FEB, 1990 (thick solid line), with simultaneous MU radar observation (thin solid and dashed lines for MST and meteor wind observations, respectively).

estimated as 8 and 3 km at the altitudes of 80 and 60 km, respectively. Comparing the profiles of the rocketsonde and MU radar observations in Fig. 2.4, we found that both zonal and meridional wind velocities agreed well up to about 80 km despite of their differences in the observation locations and intervals, the latter differing as large as about 8 hr.

It can be generally understood that the accuracy of the wind velocity measurement seems to become worse as the altitude goes higher, since the motion of the falling sphere does not necessarily follow the atmospheric motions at high altitudes. Hyson [1968] suggested that the difference between the horizontal speed of a falling sphere and the motion of the ambient atmosphere exponentially decreases as the altitude decreasing, and further defined a range constant, corresponding to the vertical distance, in which the difference in the horizontal speeds decreases by a factor of e. The range constant h can be written as $h = 2m/(C_d S\rho)$, where m, C_d, S and ρ denote mass, cross sectional area and drag coefficient of the sphere and the air density, respectively. The h values become as large as about 20 and 2 km at 80 and 60 km, respectively, for the standard falling sphere with a diameter of 1 m and a weight of 160 g [Schmidlin, 1986]. Therefore, although the comparison between the profiles derived with the falling sphere and the MU radar showed reasonable agreement up to about an altitude of 80 km with the height resolution of 8 km, we should keep it in mind that the sphere sounding at the high altitude could include discrepancy from the actual wind fields due to the fairly large values of the range constant.

We now examine the altitude range where the wind fluctuations can be delineated reliably enough for analysis of gravity waves. After the falling sphere profiles were averaged, producing the equally spaced data samples with the interval of 300 m, a low pass filter with a cutoff of 3 km was applied so as to increase the confidence by reducing the random noise. Using these data, we further extracted the wind velocity fluctuations, as illustrated in Fig. 2.5, using a band pass filter with a pass band of 4–6 km for both the falling sphere and the MU radar results. We can recognize that the sphere data in the height range above 70 km showed wind velocity fluctuations with much larger values than detected with the MU radar data. In the altitude range from 50 to 70 km, amplitudes of the fluctuations obtained with the falling sphere for meridional components grew with height from about 2 to 14 ms^{-1}, exceeding the MU radar results by about 6 ms^{-1} above 60 km, while the zonal components showed a reasonable consistency with the MU radar profile up to 65 km.

Within the altitude range of the direct comparison of the profiles between the sphere and the MU radar experiments, we were unable to clearly define the reliable height region suitable for the analysis of gravity waves with vertical scales down to a few km. Therefore, we describe these fluctuations in terms of the

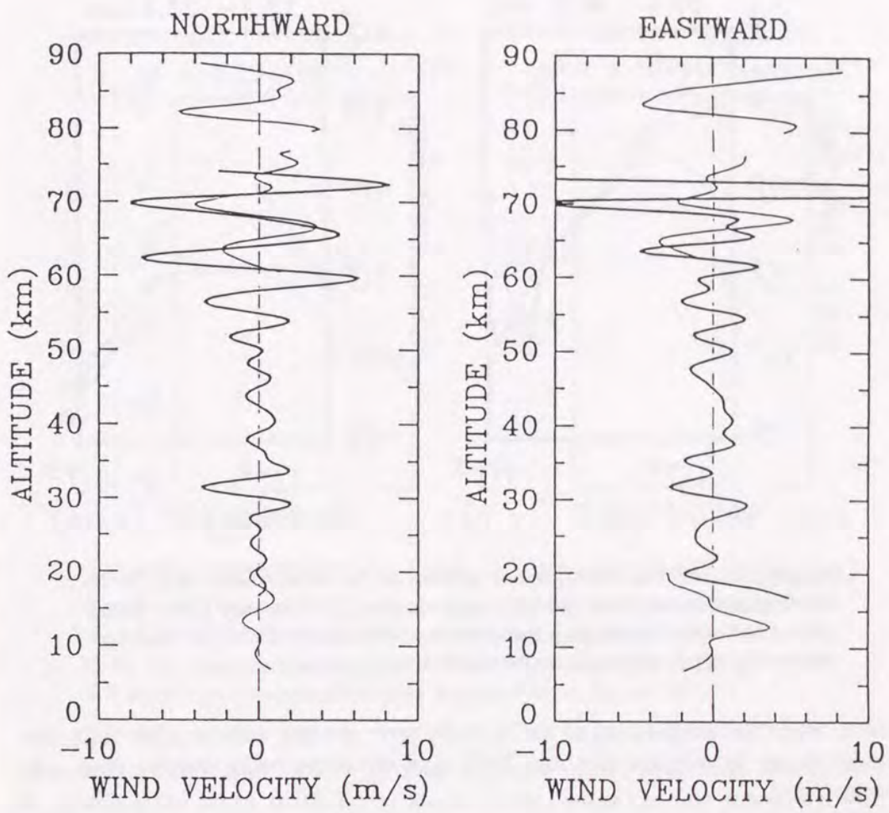

Figure 2.5: Band-passed (4–6 km) fluctuations of (right) zonal and (left) meridional wind velocities observed with the MU radar (thin lines) and the falling sphere (thick lines) on 24 February 1990.

vertical wavenumber spectra, whose statistical characteristics were empirically well established through a theoretical model as well as the earlier experimental results [e.g., Smith et al., 1985; Tsuda et al., 1989].

Figure 2.6 shows the vertical wavenumber spectra of horizontal wind velocity observed with the MU radar in comparison with the model spectrum, which show the fairly representative behavior in each height region. That is, the model is considered to give the upper limit of the spectral density at each wavenumber. The mesospheric spectra agreed well with the model value in the wavenumber region of 1.1×10^{-4}–7×10^{-4} c/m for both the zonal and meridional compo-

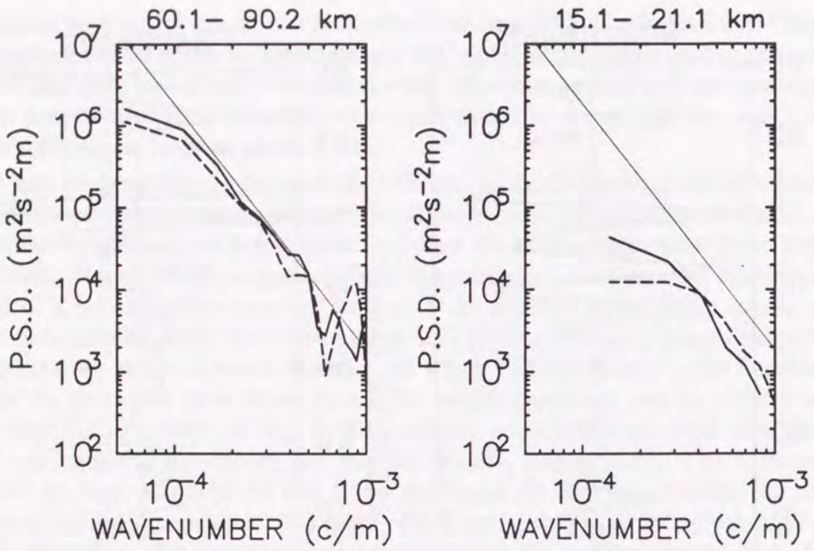

Figure 2.6: Vertical wavenumber spectra at 60–90 km (left) and 15–22 km (right) derived from the MU radar data on 24 February 1990. Zonal and meridional components are presented as solid and dashed lines, respectively. Slant solid lines represent the model spectrum.

nents, while the amplitudes of the stratospheric spectra were smaller than the model values by a factor of about 3–10, and the slope being smaller than −3, respectively.

While, Fig. 2.7 presents vertical wavenumber spectra determined from the falling sphere results on 24 February 1990 in two height regions at 50–60 and 56–66 km, partially overlapping with each other. The spectra of the zonal and meridional components in the 50–60 km height range showed amplitudes smaller than the model value by a factor of about 7 and 2, respectively, and slightly gradual slopes of about –1.7 for both components, which reasonably interpolated the spectra collected with the the MU radar in the regions above and below. On the other hand, in the height range of 56–66 km, the spectral amplitudes of the zonal component were larger than the model values by a factor of about 7, although meridional component appeared similar to the model. Therefore, we could consider that the wind velocity profiles above about 60 km obtained from the falling sphere experiment may not be used for the analysis of the gravity waves.

To summarize the direct comparisons between the falling sphere and the MU

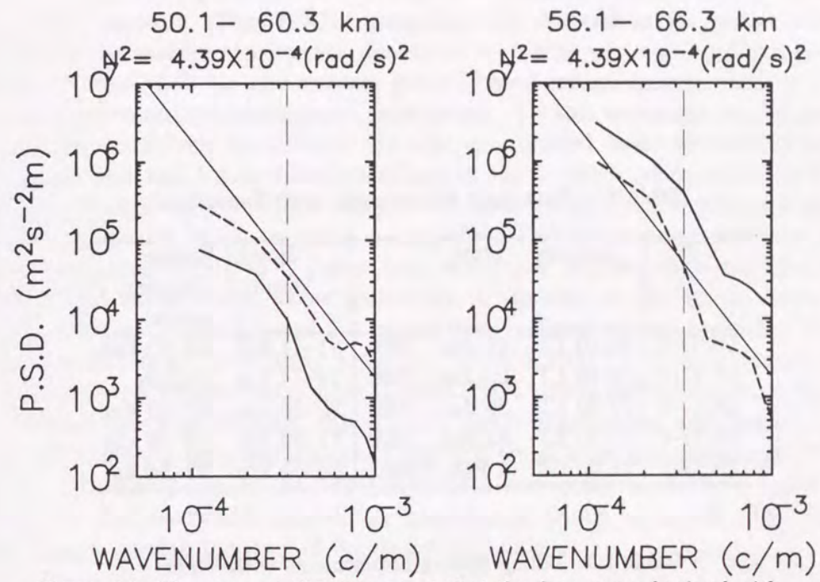

Figure 2.7: The same as Fig. 2.6 except that the data were obtained with the DUS-9 on 24 February 1990 and the height ranges of 50–60 (left) and 56–66 km (right). Vertical dashed lines indicate the cutoff vertical scale of 3 km of the low-pass filter that was applied to the winds.

radar results, the wind velocity profiles with the sphere soundings can be used for profiling the mean winds up to about 80 km, when the fine structures with vertical scales less than about 8 km were smoothed out. While, the maximum height for the studies of the gravity wave characteristics, having scales down to a few km, should be restricted to about 60 km, below which the height resolution was reasonably good for describing the characteristics of gravity waves. Note, however, that the latter conclusion was inferred from the investigation on the behavior of the vertical wavenumber spectra.

Campaign Observations

Through international cooperation, the Solar Terrestrial Energy Program (STEP) is currently being conducted in order to obtain a quantitative understanding of the coupling processes between different height regions of the atmosphere through studies on the dominant mechanisms responsible for the energy and mass transfer. Campaign observations of DYANA (DYnamics Adapted Net-

Table 2.1: Datasonde Experiments with Super Loki

No.	Launch Time		Height Range	
			Wind	Temperature
DUD-1	21:10 LT	17 Jan. 1990	21–71 km	20–55 km
DUD-2	21:10 LT	20 Jan. 1990	23–74 km	Failure
DUD-3	21:00 LT	29 Jan. 1990	20–55 km	32–56 km
DUD-4	21:25 LT	31 Jan. 1990	17–52 km	22–56 km
DUD-5	21:00 LT	5 Feb. 1990	20–53 km	22–54 km

Table 2.2: Falling Sphere Experiments with Viper

No.	Launch Time		Height Range
DUS-8	21:00 LT	17 Feb. 1990	18–107 km
DUS-9	21:00 LT	24 Feb. 1990	15–111 km
DUS-10	21:00 LT	26 Feb. 1990	20–107 km

Table 2.3: Datasonde Experiments with MT135

Rocket	Launch Time		Height Range	Results	
				Wind	Temp.
MT135-44	11:25LT	11, Sep. 1985	12–63 km	Good	No good
MT135-45	11:20LT	20, Aug. 1986	16–58 km	Good	Good
MT135-47	11:00LT	9, Sep. 1987	17–58 km	Good	No good
MT135-48	13:00LT	9, Sep. 1987	17–57 km	Good	Good

work for the Atmosphere), were conducted in January–March 1990, as one of the STEP projects. The DYANA campaign was devoted to the global observation of the middle atmosphere dynamics by means of internationally coordinated rocket, balloon and various ground-based measurements with radars, lidars, passive optical instruments, and so on. To this campaign, a Japanese group has extensively contributed through coordinated observations including the Super Loki and Viper rocket soundings in Japan which are described in this section [Oyama, 1992]. All the information concerning the scientific activities conducted by the Japanese group during the DYANA campaign was summarized by Oyama [1991]. The Super Loki and Viper systems were employed in the DYANA experiments, whose rocket launch schedule at Uchinoura, Japan is summarized in Tables 2.1 and 2.2, respectively. Based on the campaign time schedule, the rocket launchings were done around 2100 LT at each station, so the rocket experiments contributed to the DYANA were carried out at night.

Independently of DYANA, the MT-135 rocket experiments were carried out also at Uchinoura, as summarized in Table 2.3, which were cooperated with MU radar. The launchings of the MT-135 rockets were made in daylight hours in Japan, so the observation periods for mesospheric winds by means of the MU radar could overlap the time of the rocket soundings.

Background Conditions during the Dyana Campaign

General Characteristics of Wind Velocity and Temperature Profiles

The mean horizontal winds and temperatures in the middle atmosphere during the DYANA campaign were revealed by the observations with the MU radar and rocketsondes Super Loki and Viper. We here show the background conditions of the middle atmosphere during the campaign period when gravity wave behaviors will be analyzed in later chapters [Murayama et al, 1992b].

We present in Fig. 2.8 the observed profiles of horizontal wind velocity in the height range of 20 to 60 km, eight profiles for the eastward and northward wind velocity being shown. The general behavior of the zonal component can be described as follows: its amplitude was fairly small at the lowest altitude, i.e., at 20 km, it became westward, and then reversed direction toward the east at higher altitudes. The meridional component showed small amplitudes below 35 km throughout the observation period, and was generally southward (equatorward) above 35–40 km, the amplitudes ranging from 5 to 15 ms^{-1}.

Simultaneously illustrated in the bottom panel of Fig. 2.8 are the model zonal winds taken from the CIRA 1986 model at 30°N, where the profiles were linearly interpolated from the monthly values by assuming that the model represents the profile in the middle of each month. Note that we present only the zonal mean

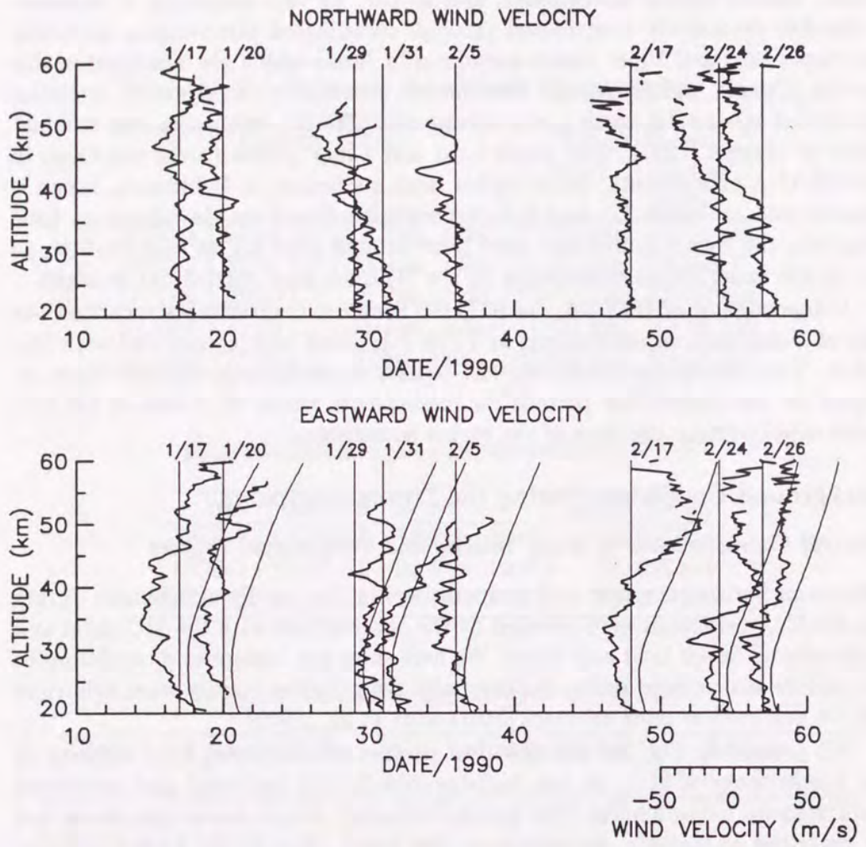

Figure 2.8: Profiles of northward (top) and eastward (bottom) wind velocity obtained with rocketsondes at 20–60 km. Note that the vertical reference line, indicating 0 ms^{-1} for each profile, shifts according to the date of the year of the experiment. The zonal winds taken from the CIRA 1986 model in January and February at 30°N are also indicated by thin lines.

values of the CIRA 1986 model, although the model includes the climatological patterns of the planetary waves with longitudinal wavenumbers 1 and 2, which, however, normally have significant effects on the zonal winds in winter.

In fact, a part of the discrepancy in the zonal winds between the observations and the model can be explained by considering the behavior of planetary waves. In particular, the westward winds demonstrated in the stratosphere in Fig. 2.8, for instance, on 17 and 20 January, seemed to be caused by the effect of planetary waves with longitudinal wavenumber 1, whose effect frequently becomes dominant in winter, enhancing the Aleutian high [e.g., Matsuno and Shimazaki, 1981].

However, the most striking feature of the zonal winds during the DYANA campaign seemed to be represented by the fairly large time variations. In order to exhibit more clearly these variations, Figs. 2.9 and 2.10 show contour plots of the zonal and meridional winds, respectively, obtained by combining the profiles in Fig. 2.8 and the MU radar results in the mesosphere, where a low-pass filter with a cut-off at 8 km was applied in order to remove small scale fluctuations caused by gravity waves.

The altitude of the zonal wind reversal from westward toward the east was 40–45 km at the beginning of the observation period, but it rapidly dropped to below 40 km in the sixth profile and became as low as 35 km at the end of February. Moreover, although the height region of the westward winds was extended to 20–50 km on 17 January 1990, it was only 20–35 km at the end of the observation period.

While for the third and fourth profiles in Fig. 2.8 obtained on 29 and 31 January, the westward winds in the stratosphere almost completely disappeared, but they became slightly eastward in the entire height range, exhibiting the discontinuous time variations of the zonal winds in comparison with other profiles. Note that the discontinuous behavior of the zonal winds at the end of January 1990, being deviated from the general tendency of the zonal winds, can be more easily recognized in Fig. 2.9. The time variation of the profiles, excluding the third and fourth ones, suggests that the phase speed of the downward progression of the zonal wind reversal is to be about −0.3 km/day. The contour plots for the meridional winds in Fig. 2.10 generally reflect the variation of the zonal winds. In particular, southward winds of more than 15 ms^{-1} were detected at the end of January, which coincides with the discontinuous behavior of the zonal component in Fig. 2.9.

The temperature profiles during the first half of the DYANA campaign period are illustrated in Fig. 2.11 being derived from the four DUD soundings listed in Table 1. The zonal mean profile taken from the CIRA 1986 model in January at 30° N is also plotted in Fig. 2.11 for reference. Below about 40 km the first profile

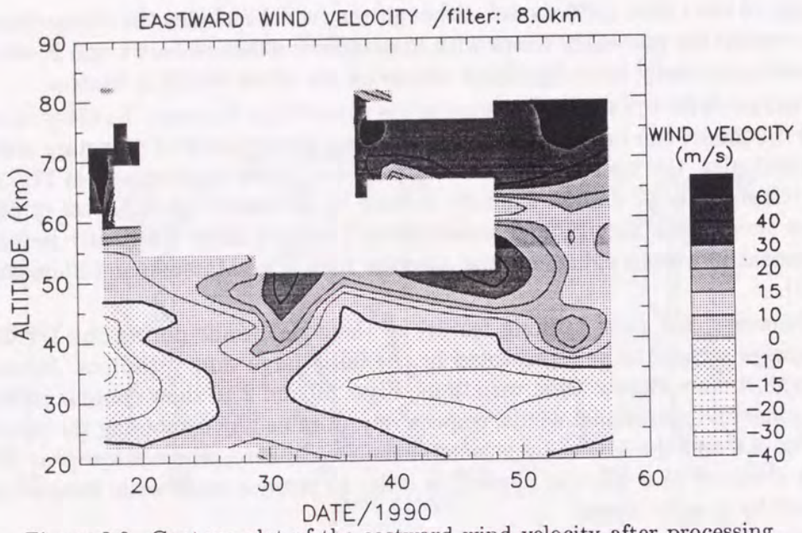

Figure 2.9: Contour plot of the eastward wind velocity after processing with a low-pass filter, having a cut-off at 8 km, for each sounding shown in Fig. 5, combined with the daily mean profiles observed with the MU radar on 16–19 January, and 6, 7 and 9 February 1990.

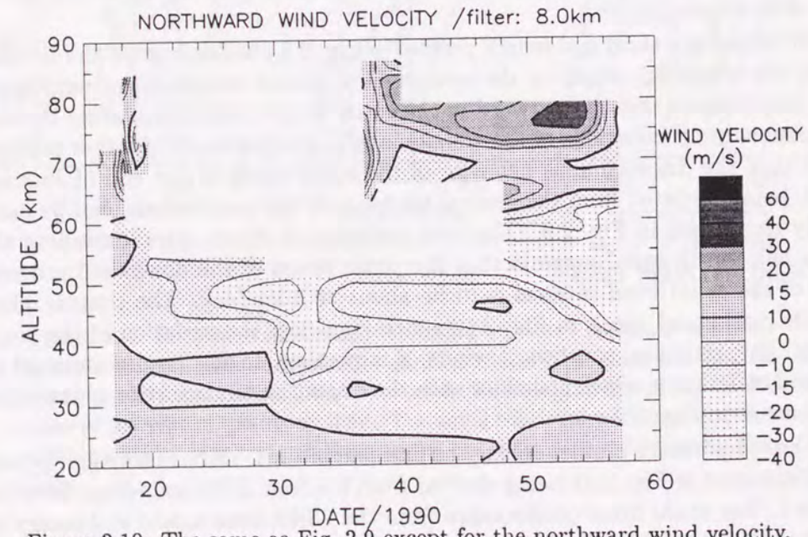

Figure 2.10: The same as Fig. 2.9 except for the northward wind velocity.

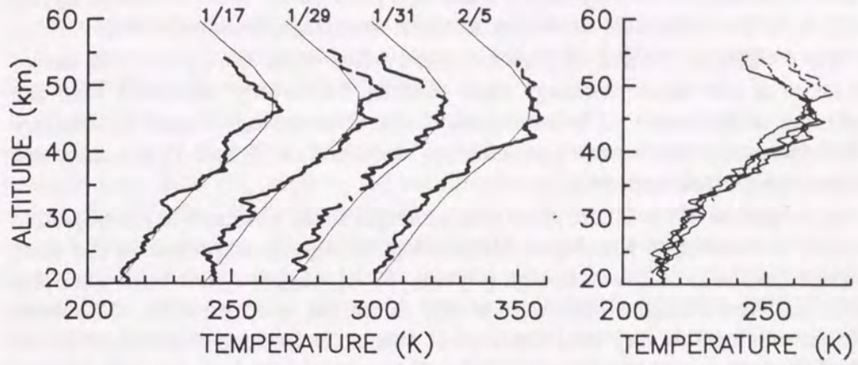

Figure 2.11: Temperature profiles obtained with the Super Loki rocketsondes at 20–60 km. The successive profiles are shifted by 30°C in the left panel, while all the profiles are simultaneously illustrated in the right panel in order to show the time variations. The thin lines show the CIRA 1986 model profile in January at 30°N.

agreed reasonably well with the model, although fluctuations were recognized, while the other three profiles showed smaller temperature values than the model by 5–10 K. Moreover, the altitude region with the lower temperature expanded from 22–35 km on 29 January to 22–40 km on 31 January, and further to 20–41 km on 5 February.

The maximum temperature in each profile was detected at 45–50 km, but the location of the stratopause cannot simply be determined because of the complicated structure, exhibiting many peaks and dips. In addition, the temperature profiles in the mesosphere involved quite large fluctuations. For example, by comparing the profiles collected on 29 and 31 January, it can be recognized that there was a large decrease in the mesospheric temperature profile within the three day period, the maximum difference between the extreme values being about 20 K above 48 km.

Effect of a Minor Stratospheric Sudden Warming

It was reported that a minor stratospheric warming, accompanied by a significant temperature increase at 60°N, occurred at the beginning of February 1990 [Hirooka et al., 1992]. Although the direct manifestation of a stratospheric warming is normally confined to the high latitude region [e.g., Andrews et al.,

1987], its effect can reach down to the middle and low latitudes (for example, at 30°N), as reported during major warmings [Kanzawa, 1980; Gille and Lyjak, 1984], or in the numerical model for a minor warming [Matsuno, 1984].

The profiles on 29 and 31 January were collected in the period just before the onset of the minor warning, while that on 5 February coincided with the beginning of the event. The westward winds, detected on 17 and 20 January well before the minor warming event, were weakened on 29 and 31 January, and the eastward winds appeared.

Investigation of the 10 mb geopotential height maps obtained in the objective analysis conducted at the Japan Meteorological Agency, reported in the data catalogue of the DYANA campaign [Oyama, 1991], suggests that both the polar vortex and the Aleutian high were stably dominant in the middle of January 1990, producing the very cold winter, but the latter became diminished at the end of January and then recovered in late February. In other words, the present minor warming occurred in such a way that the Aleutian high was weakened for half month, approximately coinciding with the minor warming event, which reasonably explains the changes in the zonal wind structure seen in Figs. 2.8 and 2.9.

It is also noteworthy that the expansion of the cold temperature region in the stratosphere below 35 km, as detected in the profiles obtained on 29 January–5 February in Fig. 2.11, in comparison with that on 17 January, seemed to be explained by the effect of the minor warming. That is, the decrease in the stratospheric temperature seemed to occur at middle latitudes, maintaining the heat balance during the minor warming by compensating for the temperature increase at higher latitudes [e.g., Matsuno and Shimazaki, 1981].

Using the data-base employed for routine weather prediction, Hirooka et al. [1992] found that the planetary waves with zonal wavenumber 1 were conspicuously enhanced at 60°N from 20 January to 10 February, coinciding with the minor stratospheric warming. Such planetary waves were, at least in part, responsible for a part of the disturbed behavior of the mesospheric temperature fluctuations detected in Fig. 2.11.

To summarize, the characteristics of the background conditions during the DYANA period, which include the structure of horizontal winds and temperatures, showed the significant variations within the 40 days of the DYANA observation period. The observed variations in the profiles of both the zonal winds and temperatures seemed to be caused by the effect of the stratospheric warming, together with the enhanced activity of planetary waves.

Wind Profiles by Two Successive MT135 Experiments with a 2 hr Interval

From Table 2.3, we notice that two MT-135 rockets, numbered as MT135-47 and MT135-48 launched at 1100 and 1300JST, respectively, on 9 September 1987, could successfully collect successive wind profiles with an interval of two hours. So it is expected that temporal variation of the wind field in two hours can be delineated from the rocket wind profiles.

The trajectories of the sondes which are projected on a horizontal plane are plotted, in Fig. 2.12, for the MT135-47 and 48 experiments on 9 September 1987. Straight lines from the origin in the south-eastward direction correspond to the ascent of the rocket, while the wave-like curve shows the movement of the sonde ejected from the rocket. The mean wind direction was generally westward, which agreed with the basic features of the general circulation in the summer middle atmosphere. The wave-like structure was very similar for the two trajectories, exhibiting fluctuations with an apparent horizontal scale of about 8 km, which, however, can not be interpreted as the horizontal wavelength of wave motions

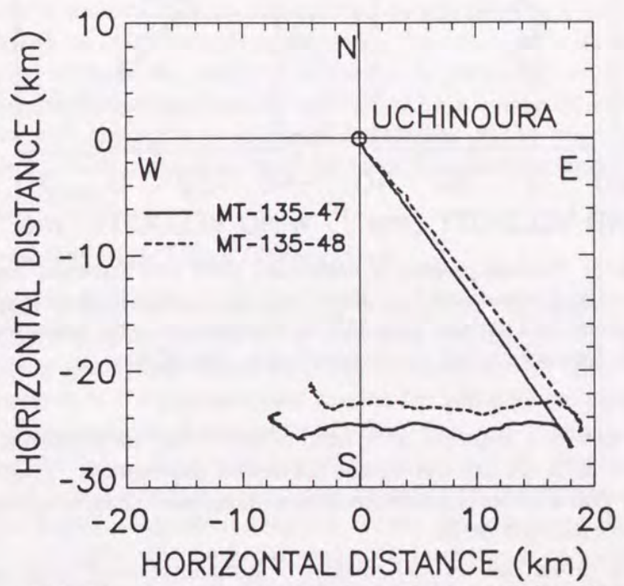

Figure 2.12: The trajectories projected on a horizontal plane for a series of rocketsonde experiments (MT135-47 and 48) at the Kagoshima Space Center, Uchinoura at 1100 and 1300 JST on 9 September 1987. A straight line shows the ascent of a rocketsonde, while a wave-like trajectory is detected during the descending motion of the rocketsonde ejected from the meteorological rocket.

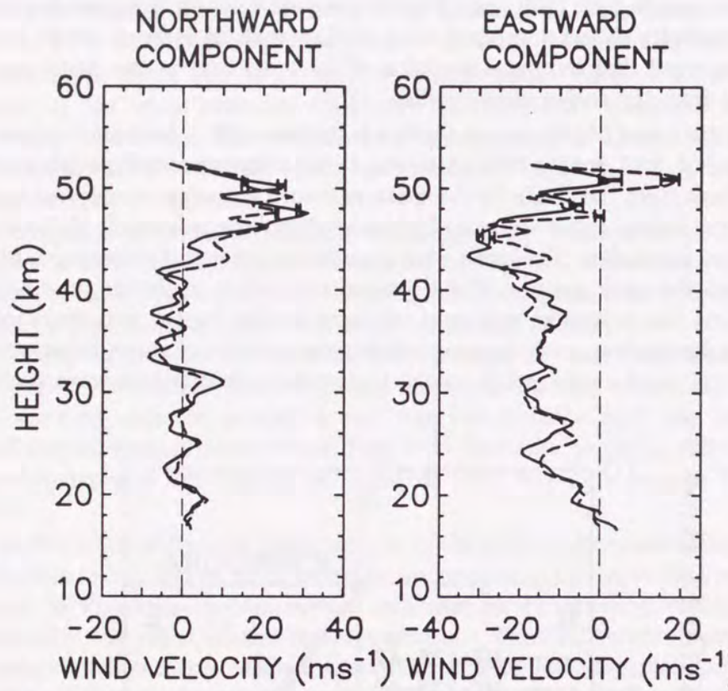

Figure 2.13: Vertical profiles of northward (left) and eastward (right) wind velocity obtained with MT135-47 (solid line) and MT135-48 (dashed line) launched at 1100 and 1300 JST on 9 September 1987, respectively. The error bars are plotted at altitudes higher than 45 km.

because they were not observed at a fixed altitude, the rocketsondes descending from about 55 to 10 km during the horizontal movements. Trajectories in Fig. 2.12 show that a series of rocketsonde soundings were done in spatial regions located closely with each other.

Figure 2.13 shows the vertical profiles of horizontal wind components detected by MT135-47 and 48, where estimation errors are indicated by a horizontal bar at altitudes higher than 45 km. Below 45 km the estimation error was not more than 1 ms^{-1} for the eastward component, while it was smaller than 0.3 ms^{-1} for the northward component. The profiles demonstrate the similarity in vertical structures of the large-scale winds as well as wave-like structures with vertical scales of approximately 2 km at 17–22 km altitude, and of 4–5 km at

22–33 km for both the northward and eastward components. Since the spatial differences of those measurements were small as shown in Fig. 2.12, downward phase progressions of the wind motions can be interpreted as time evolution. The phase progressions are seen in almost all the height range, so that these wind fluctuations are recognized to be caused by systematic wind motions of atmospheric waves, possibly by gravity waves.

2.4 Rayleigh Lidar

The lidar data of the density and temperature used in this study, were obtained from Rayleigh scattering observations with the lidar of the National Institute of Environmental Studies (NIES), Tsukuba, Japan (36°N, 140°E) [Nakane et al., 1992a], which was originally designed for DIAL (DIfferential Absorption Lidar) observation of ozone employing 6 wavelength laser beams [Sugimoto et al., 1989; Nakane et al., 1992b].

Advances in laser technology has enabled development of a Rayleigh lidar as a ground-based remote sensing instrument for the atmospheric density and temperature observation in the middle atmosphere. In particular, profiles with good time and height resolutions have been obtained by Rayleigh lidars in the upper stratosphere and mesosphere, and used for studies of the middle atmosphere dynamics [e.g., Chanin and Hauchecorne, 1981; Hauchecorne and Chanin, 1982; Wilson et al., 1990].

Principle of Rayleigh Lidar Observation

A lidar (LIght Detection And Ranging) is designed on the basis of the principle similar to that of a radar, despite of the operating frequency in the optical range. A laser pulse is weakly backscattered in the atmosphere, and then the scattered light is processed in the ground-based station to detect its strength and range. When the wavelength of the transmitted light does not coincide with that of atmospheric resonance, the backscattered signal is due to Rayleigh scattering by molecules and Mie scattering by aerosols depending on the existence of aerosols. At altitudes higher than around 30 km where the scattering due to aerosol is normally negligible, the backscattered echo intensity is proportional to the atmospheric density. Thus the atmospheric density, ρ, can be derived by using a equation,

$$\rho(z) = C\frac{S(z) - B(z)}{T(z,\infty)^2} \tag{2.1}$$

where S is the received signal at a height z in a constant solid angle, and B is the background noise signal due to the sky noise and the dark current (usually the

dark current is much smaller than the sky noise). While, $T(z,\infty)$ is the atmospheric transmission between a height z and the top of the atmosphere, which is estimated along the transmitted and received beam for the used wavelength including the attenuating effect by ozone and Rayleigh scattering [Chanin and Hauchecorne, 1984]. C is a normalization constant, which is known to have large temporal variability due to, for instant, weather condition and fluctuation of the transmitted laser power. So C is often calibrated by fitting the signal with the model atmosphere around the 30–35 km height, or with radiosonde observations.

The height range of the signal usable for the atmospheric observations have the upper limit altitude at which the Signal-to-Noise ratio becomes enough small. The lower limit is determined from the height region where Mie scattering contaminates, which usually becomes 30–35 km depending on the aerosol density.

It is known that the number of the received photons obeys the Poisson distribution, so the statistical error (the standard deviation) of the signal S is equal to the square root of S. So we can write the relative uncertainty in the density as;

$$\frac{\delta\rho}{\rho} = \frac{\sqrt{S(z)}}{S(z) - B(z)}. \tag{2.2}$$

We briefly show the derivation of temperature from the air density following the description by Chanin and Hauchecorne [1984], Hauchecorne [1983] and Wilson [1989]. We assume that the atmosphere is in the hydrostatic equilibrium, satisfying the equation of state for the ideal gas;

$$dP(z) = -\rho(z)g(z)dz \tag{2.3}$$

$$P(z) = R\rho(z)T(z) \tag{2.4}$$

where P, T and g are the pressure, temperature and gravitational acceleration, respectively, and R is the gas constant per unit mass for the atmosphere. Combining (2.4) and (2.3), we have

$$\frac{dP(z)}{P(z)} = d[\ln P(z)] = -\frac{g(z)}{RT(z)}dz. \tag{2.5}$$

Therefore, we can recognize that the differentiation of $\ln P$ with respect to height is a function of temperature and independent of any constants in the measurement system.

When we consider the discrete layers of the atmosphere with a thickness of Δz, and assume that g and T are constant in the i-th layer at a height z_i ($i = 1, 2, ...N$; $z_{i+1} > z_i$), (2.5) leads to the temperature value expressed by P;

$$T(z_i) = \frac{g(z_i)\Delta z}{R\ln\left[\frac{P(z_i - \Delta z/2)}{P(z_i + \Delta z/2)}\right]}. \tag{2.6}$$

Here we introduce a variable X_i as;

$$X_i \equiv \frac{\rho(z_i)g(z_i)\Delta z}{P(z_i + \Delta z/2)} = \frac{\rho(z_i)g(z_i)\Delta z}{\sum_{j=i}^{N}\rho(z_i)g(z_i)\Delta z + P(z_N + \Delta z/2)}. \tag{2.7}$$

Using X_i, the pressure ratio in the logarithm in (2.6) can be written as $[1 + X_i]$, so that the temperature value at a height of z_i is given as;

$$T(z_i) = \frac{g(z_i)\Delta z}{R\ln[1 + X_i]}. \tag{2.8}$$

In (2.7), it is necessary to determine the pressure value at the highest altitude, $P(z_N + \Delta z/2)$, from the model atmosphere. We assume that the observation and the model atmosphere have the same values of temperature both of which are averaged for a height range of δz at around z_N, where δz is taken to be 4.8 km. δz can be written as $\delta z = k\Delta z$ ($k = 32$ when Δz =0.15 km). Using (2.5), this condition results in a relation between the observed and model pressure values;

$$\frac{dP(z_N)}{P(z_N)} = \frac{dP_m(z_N)}{P_m(z_N)} \tag{2.9}$$

where P_m is the model pressure. This can be rewritten as

$$\frac{P(z_N - \delta z) - P(z_N)}{P(z_N)} = \frac{P_m(z_N - \delta z) - P_m(z_N)}{P_m(z_N)}. \tag{2.10}$$

So that we find that $P(z_N)$ is given as

$$P(z_N) = \frac{P_m(z_N)}{P_m(z_N) - P_m(z_N - \delta z)}\sum_{j=N-k}^{N}\rho(z_j)g(z_j)\Delta z \tag{2.11}$$

From this expression of $P(z_N)$, we notice that both the denominator and numerator in (2.7) have the term of the observed density ρ, which means the proportional factor in ρ vanishes in the calculation of X_i, and therefore for $T(z_i)$.

As noted in the above temperature derivation, calculation of the term X_i requires the ratio of the observed values of the density, so that absolute value of temperature can be determined by this method as far as the initial value of the pressure $P(z_N + \Delta z/2)$ can be much smaller than the integral of the density in (2.7).

The statistical error of temperature can be derived from the error of the density in (2.2) as;

$$\frac{\delta T(z_i)}{T(z_i)} = \frac{\delta\ln|1 + X_i|}{\ln|1 + X_i|} = \frac{\delta X_i}{(1 + X_i)\ln(1 + X_i)}, \tag{2.12}$$

where

$$\left(\frac{\delta X_i}{X_i}\right)^2 = \left(\frac{\delta\rho(z_i)}{\rho(z_i)}\right)^2 + \left(\frac{\delta P(z_i+\Delta z/2)}{P(z_i+\Delta z/2)}\right)^2, \tag{2.13}$$

and

$$\delta P(z_i+\Delta z/2)^2 = \delta P(z_N+\Delta z/2)^2 + \sum_{j=i+1}^{N} (\delta\rho(z_i)g(z_i)\Delta z)^2. \tag{2.14}$$

The uncertainty of the pressure at the top of the Nth layer, $\delta P(z_N+\Delta z/2)$, is taken to be about 15%, since the temperature variation throughout the year at the top height of the observation (about 70–90 km) is considered to be generally within 15% of the annual mean value.

Experimental Setup

A block diagram of the NIES ozone lidar system is shown in Fig. 2.14. The NIES ozone lidar is composed of two subsystems, which are the low altitude (LA) system for the troposphere observation and the high altitude (HA) system for the stratosphere and mesosphere. In the LA system, laser beams with three wavelengths of 277, 313 and 292 nm are emitted from a KrF excimer laser

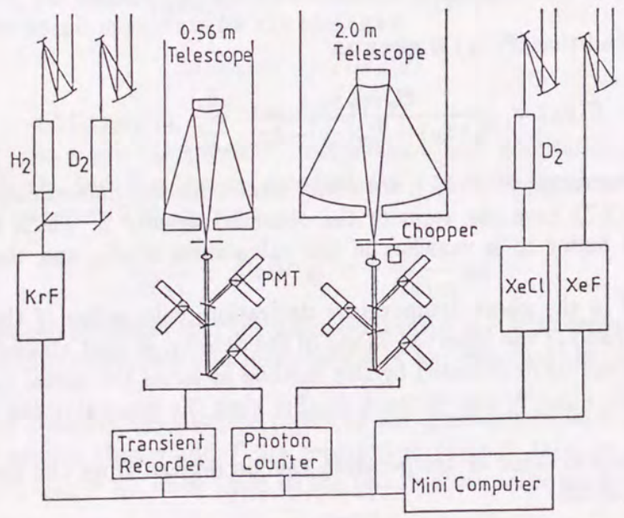

Figure 2.14: Schematic diagram of the NIES ozone lidar system [Sugimoto et al., 1989].

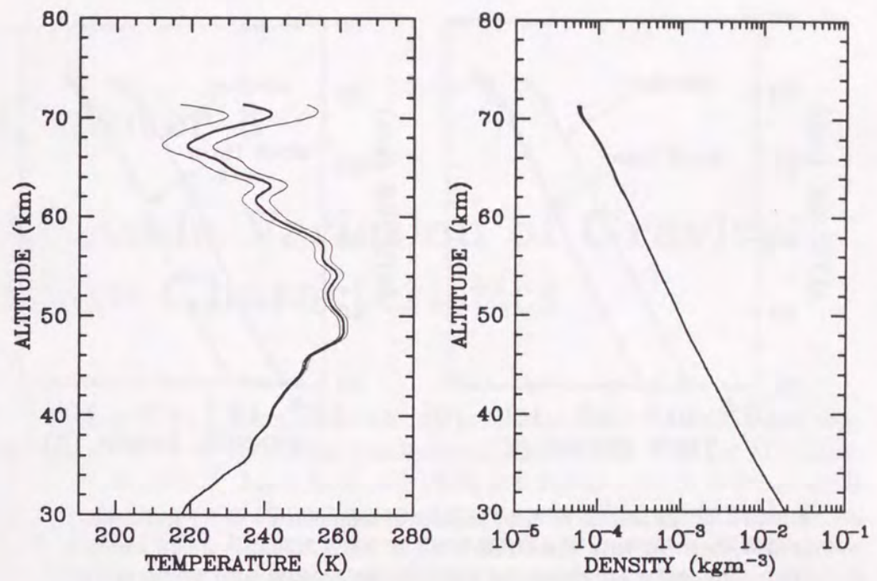

Figure 2.15: An example of temperature (left) and density (right) with height and time resolutions of 3 km and 1 hour, respectively, observed with the NIES lidar at 2034–2134JST on 28 January 1991. Thin lines indicate uncertainty of temperature (1 standard deviation).

through Raman shifters and their scattered light is received with a telescope of 0.56 m in diameter. The HA system employs the XeCl and XeF excimer lasers to emit light with wavelengths of 308, 339 and 351 nm and a receiving telescope with the diameter of 2 m.

A laser beam pulse at each wavelength in each subsystem is detected by two photomultiplier tubes (PMTs) which are used for high sensitivity (HS) and low sensitivity (LS) channels to keep wide dynamic range of detectable signal. The HS channel utilizes about 92% of the signal for each wavelength.

In order to avoid too strong echoes from the near field which results in a saturation of PMTs and signal induced noise [Iikura et al., 1987], the HA system is equipped with a mechanical chopper rotating with a frequency of 188 Hz, which provides timing signals for other instruments in the lidar system.

In order to obtain the air density and temperature used in this thesis, we utilized the data with a wavelength of 351 nm obtained from the HS channel in

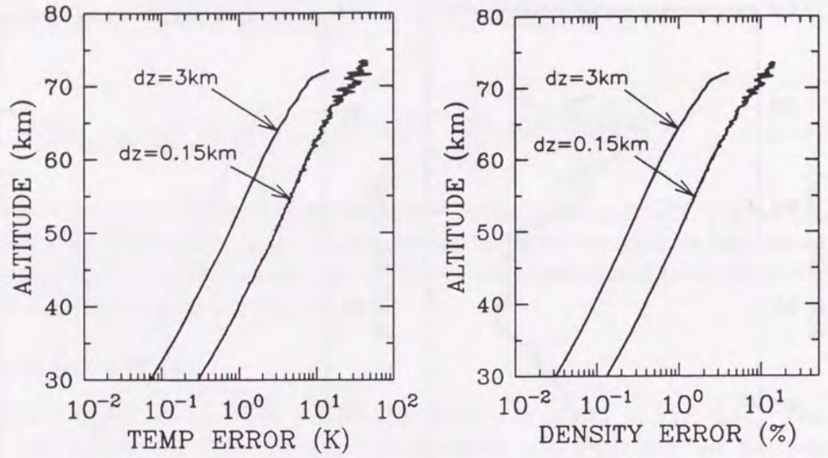

Figure 2.16: Examples of error profiles of temperature (left) and density (right) observed with the NIES lidar at 2034–2134JST on 28 January 1991. The errors are shown for hourly mean profiles with height resolutions of 3 and 0.15 km.

the HA system. An example of the observed profiles of hourly mean temperature and density with a height resolution of 3 km is shown in Fig. 2.15. In the derivation of the temperature values, the US standard atmosphere 1976 was employed for extinction correction and the pressure values near the top height, $P_m(z_N)$ and $P_m(z_N - \delta z)$. Statistical errors of the observed density and temperature depend on the number of photons detected in a range gate with a thickness of Δz during an integration time of signal, Δt. So the accuracy depends on the time and height resolution, the observation height, the weather condition such as existence of clouds, and adjustment of the optical system.

For the observation with a constant time and height resolution, the accuracy decrease with height because of the decrease in strength of the detected signal. Figure 2.16 presents examples of the temperature and density errors for the observation at 2034–2134JST on 28 January 1991. The error of hourly mean temperature with a height resolution of Δz=0.15 km was estimated to be about 0.3 and 8 K at 30 and 60 km, respectively. The error of hourly mean density with Δz=0.15 km was about 0.15 and 2.5 % at 30 and 60 km, respectively.

Chapter 3

Altitude Variation of Gravity Wave Characteristics

In this chapter we present wind velocity profiles in the stratosphere and mesosphere obtained by combining simultaneous observations with the MU radar, rocketsondes MT135, Super Loki and Viper and radiosondes in order to study the altitude variation of characteristics of gravity waves [Murayama et al., 1992a; Tsuda et al., 1992a]. In particular, we present in this chapter the altitude variation of dominant vertical scales and vertical wavenumber spectra of wind velocity profiles, and their interpretation in terms of the saturated gravity wave theory.

3.1 Altitude Increase in the Dominant Vertical Scales

We showed in the end of Section 2.3 that wind velocity fluctuations observed with two rocketsondes with an interval of two hours exhibited downward phase progression, and so was recognized to be caused by atmospheric waves.

Figure 3.1 shows a vertical profile of horizontal wind velocities observed on 11 September 1985 with MT135-44 rocketsondes at 14–56 km, with a routine rocketsonde at Ryori (39°02'N, 141°50'E) in the 20–57 km height region, with the MU radar in two separate regions, i.e., at 5–25 km and 60–90 km, and with routine radiosondes at Sendai (38°16'N, 140°54'E) and Kagoshima (31°34'N, 130°33'E) in the 0–25 km range [Murayama et al., 1992a]. The estimation errors of the wind velocities were smaller than 0.5 and 0.7 ms^{-1} for the rocket sounding and the MU radar measurement, respectively, in the entire altitude ranges.

The zonal wind velocity profiles observed with the MU radar and radiosondes reflect the vertical and latitudinal structures of the jet stream in the troposphere

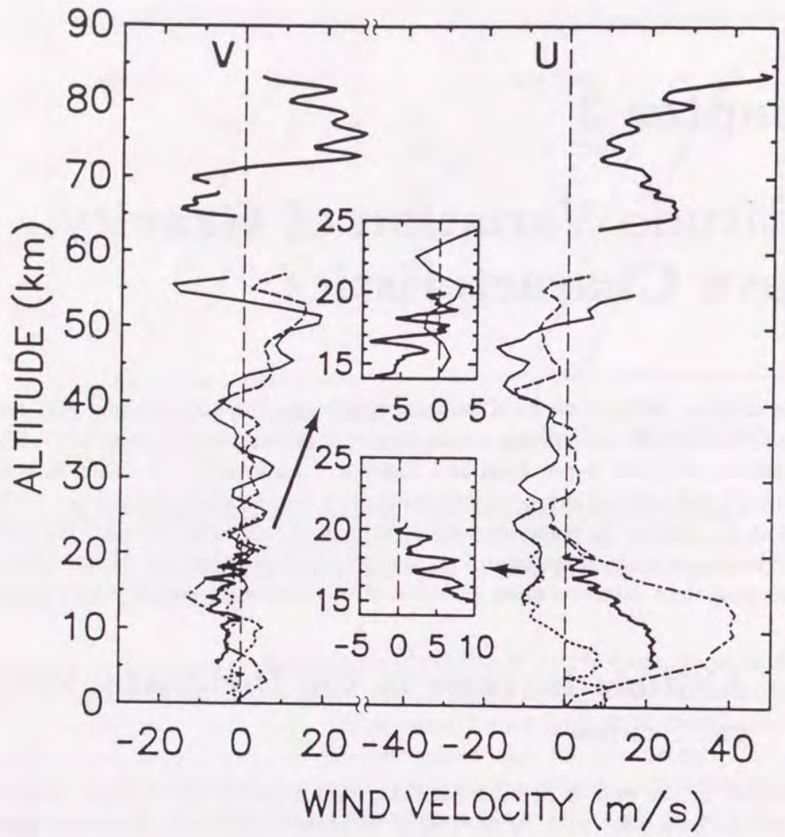

Figure 3.1: Vertical profiles of northward (left) and eastward (right) wind velocity observed on 11 September 1985 with the MU radar (thick solid lines at 5–25 km and 60–90 km), rocketsonde MT135-44 launched at 1125 JST (thin solid lines at 14–56 km), a rocketsonde launched from Ryori at 1101 JST (long dashed lines at 20–57 km), and radiosondes launched from Sendai (chained lines at 0–24km) and Kagoshima (dotted lines at 0–26 km) at 0830 JST, respectively. The enlarged profiles are plotted for the MU radar and the rocketsonde soundings in the height range of 14–25 km.

and lower stratosphere. The jet stream has an eastward peak of 40 ms^{-1} centered at 12 km at Sendai (38°16'N), decreases in amplitude to about 20 ms^{-1} with a maximum at lower altitude over Shigaraki (34°51'N) and becomes as small as 10 ms^{-1} at Kagoshima (31°34'N), which indicates that the jet stream lay over the northern part of Japan in September.

Wind velocity perturbations in the troposphere seem to be suppressed due to a small N_b^2. In the lower stratosphere, the MU radar observations clearly show fluctuations in amplitudes and the vertical scale of about 2–3 ms^{-1} and 2 km, respectively, in both eastward and northward wind profiles. Note that the height resolution of the routine radiosondes is approximately 1 km, while that of the MU radar observations is 150 m in the lower atmosphere. Therefore, the fine structure of wind fluctuations detected with the MU radar is not correctly determined with radiosonde observations, the latter being biased toward the perturbations with vertical scales larger than the dominant components.

In the 17–35 km region the rocketsonde observation at Uchinoura shows predominance of a gravity wave with a vertical scale of approximately 5 km. There is clear correlation between the zonal and meridional components. The wave amplitude of the meridional wind increases from 3 ms^{-1} at 17 km to 6 ms^{-1} at around 30 km. The zonal component has a similar amplitude, but its growth is not obvious. The lowest part of the rocketsonde profile might also be affected by the poor height resolution. However, the dominant vertical scale of gravity waves at around 30 km altitude seems to be about 5 km.

At 35–55 km altitude, the rocketsonde observations show the overlapping of at least two waves with vertical scales of about 5 km and 15 km, where the amplitude of the former is likely to be similar to that detected in the 17–35 km region, and for the latter it becomes as large as 15 ms^{-1}. The dominant vertical scale there seems to range from 5 to 15 km.

The wind velocity profile above 60 km observed with the MU radar shows a dominant wave with a vertical scale of approximately 15–20 km. The wave amplitude of the meridional component is about 20 ms^{-1}, which is larger than the zonal one ranging from 10 to 12 ms^{-1}. On the basis of a series of the MU radar observations, Tsuda et al. [1990a] reported that the dominant wave is not repeated as a function of local time, so it is not due to atmospheric tides, but is likely a manifestation of upward propagating gravity waves. The mesospheric profile also consists of smaller scale fluctuations with amplitudes ranging up to 5 ms^{-1}.

Besides the rocket observations in September, another example of snapshot profiles of the simultaneous observations with the MU radar and rockets are also shown in Fig. 3.2, which were collected on 17 February 1990, with a falling sphere at 18–60 km, and the MU radar in two regions at 5–25 km and 60–90 km

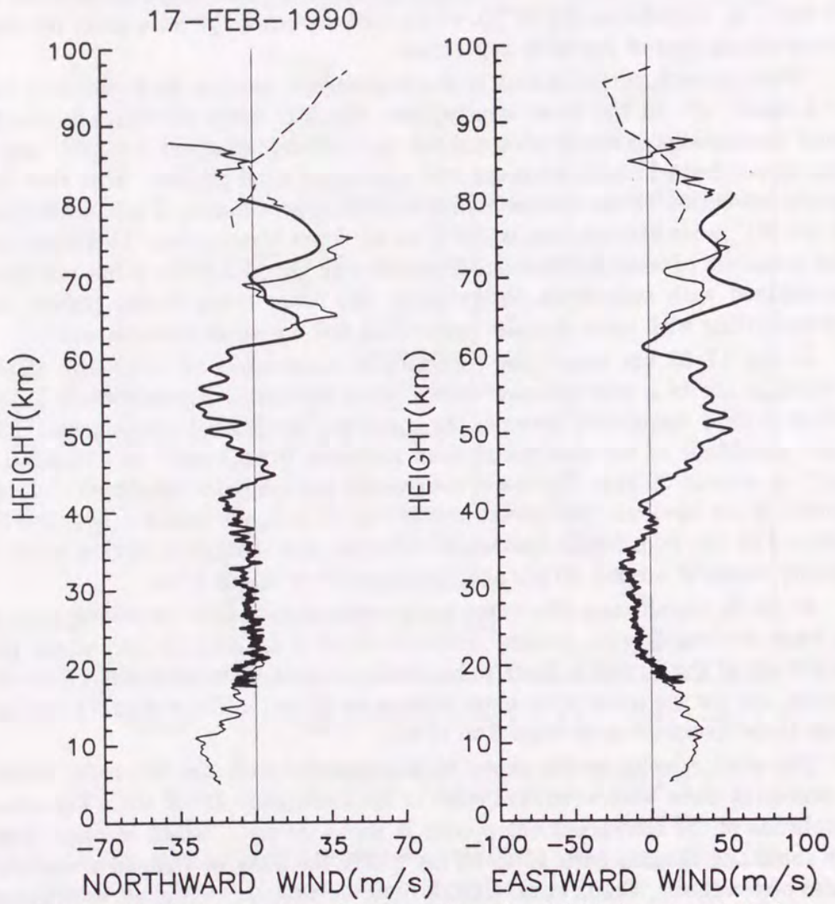

Figure 3.2: Vertical profiles of (left) northward and (right) eastward wind velocity observed with the sphere and the MU radar on 17 February 1990. The thick solid line indicates the sphere data, while the other lines represent MU radar observations, i.e., the MST observations in the height regions of 5–22 and 60–90 km for 1738–1838LT and 1214–1340LT, respectively (thin solid lines), and the meteor wind observation for 1908–2302LT (thin dashed line).

[Tsuda et al., 1992a].

Note that the observations with the rocketsonde and the MU radar were not conducted during the same periods of a day. For instance, there is up to 9 hours difference between the profiles obtained with the rocketsonde and the mesospheric observations with the MU radar, because the latter were limited to during the daytime.

Superimposed on the fundamental structures of the wind velocity and temperature profiles, fluctuations with vertical scales ranging from a few to several km can generally be also recognized as in September 1985, showing fairly good correlations between the zonal and meridional components. The dominant vertical scales of the fluctuations generally increased with altitude. The amplitudes of the fluctuations also increased greatly with altitude such that they were a few ms^{-1} below about 20 km, 5–10 ms^{-1} near 40 km and 20–30 ms^{-1} above 60 km.

The two sets of wind velocity profiles obtained by combining radar and rocket observations clearly showed that the vertical wavelength as well as the amplitude of the dominant gravity wave increases with altitude, indicating no substantial discrepancy between the observations in September and February. The ratio of the dominant vertical scales between the mesospheric and lower stratospheric results was about 4–10, and the ratio of the amplitudes was about 5–10, which can be generally interpreted as the saturation of upward propagating gravity waves, as described in section 1.2.

3.2 Vertical Wavenumber Spectra

Spectra in Summer (August 1986 and September 1987)

Although dominant components of gravity waves are detected in each height region by using Fig. 3.1, the wind velocity profiles obviously include many waves with various vertical wavenumbers. In this section vertical wavenumber spectra of wind fluctuations are calculated from simultaneous MU radar and rocketsonde observations, and are compared with the model spectrum proposed by Dewan and Good [1986] and Smith et al. [1987].

Since the amplitudes of the model spectrum depend on the background values of N_b^2, we first determine N_b^2 in each height region from the vertical derivative of temperature profiles observed with rocketsondes and radiosondes. However, simultaneous temperature measurements in the height range of the mesospheric MU radar observations were not performed, so we assumed $N_b^2 = 3.35 \times 10^{-4}$ and 3.45×10^{-4} rad^2s^{-2} in August and September at 35°N, respectively, on the basis of the CIRA 1986 model atmosphere.

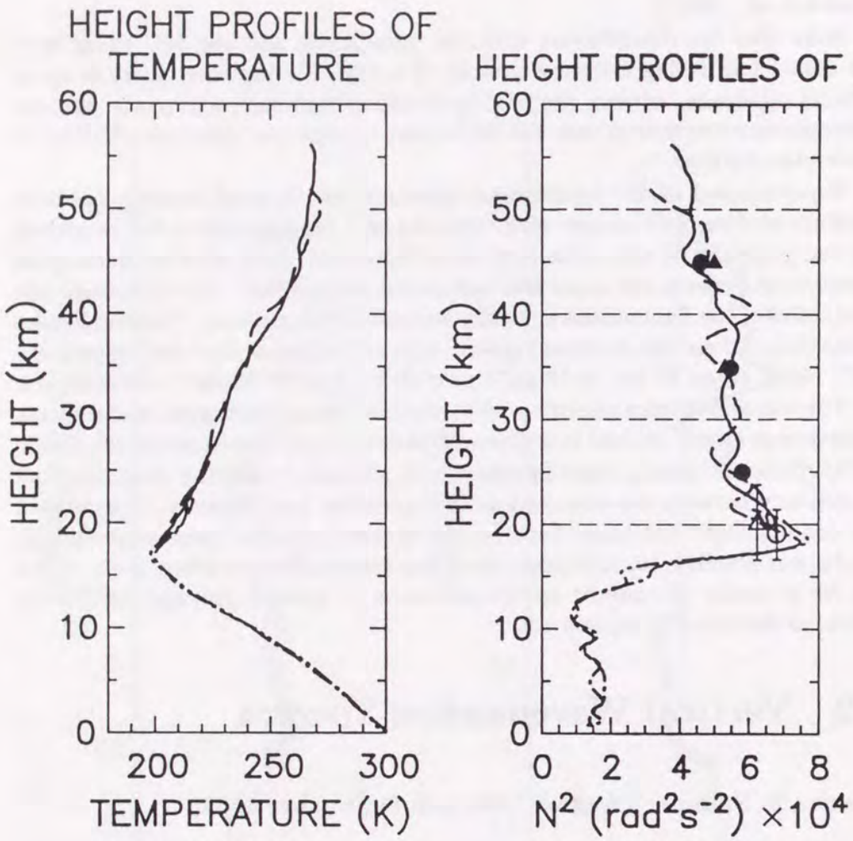

Figure 3.3: The vertical profiles of temperature, T (K) (left), and Brunt-Väisälä frequency squared, N_b^2 (rad^{2}s^{-2}) (right). Solid and dashed lines are the profiles at 17–55 km obtained from rocketsonde MT135-45 launched on 20 August 1986 and rocketsonde MT135-48 on 9 September 1987, respectively. The solid circles and triangles indicate the mean values of N_b^2 at 20–30 km, 30–40 km and 40–50 km altitudes for MT135-45 and MT135-48, respectively.

The vertical bars with an open circle and triangle indicate N_b^2 in the lower stratosphere determined from routine radiosonde soundings in the 0–21 km and 0–24 km altitudes at Shionomisaki at 0830 JST on 20 August 1986 (chained) and 9 September 1987 (double-chained), respectively.

Figure 3.3 shows both the temperature and N_b^2 profiles observed with rocketsondes MT135-45 and 48 on 20 August 1986 and 9 September 1987, respectively, and those with radiosondes launched from Shionomisaki at 0830 JST on 20 August 1986 and 9 September 1987. The mean values of N_b^2 on 20 August 1986 can be inferred to be 6.81×10^{-4}, 5.80×10^{-4}, 5.43×10^{-4} and 4.58×10^{-4} rad^{2}s^{-2} in the height regions of 17–24 km, 20–30 km, 30–40 km and 40–50 km, respectively. On 9 September 1987, N_b^2 was 6.25×10^{-4}, 5.76×10^{-4}, 5.34×10^{-4} and 4.96×10^{-4} rad^{2}s^{-2} in the respective four height ranges.

We present two sets of vertical wavenumber spectra for both zonal and meridional wind fluctuations in five height ranges observed with the MU radar and rocketsondes, where the details of the spectral analysis technique are as described by Tsuda et al. [1989]. Figure 3.4a shows spectra determined with rocketsonde MT135-45 and the MU radar at 1000–1200 JST on 20, August 1986, while Fig. 3.4b corresponds to the mean spectra of determinations with MT135-47 and 48, and the MU radar observations during 1000–1200 and 1200–1400 JST on 9 September 1987. The height ranges are (A) 17–24 km, (B) 20–30 km, (C) 30–40 km, (D) 40–50 km and (E) 65-85 km, where the MU radar observations give spectra in the lowest and highest altitude ranges. The straight lines in Fig. 3.4 are the corresponding model spectra $F_u^s(m)$ calculated by using N_b^2 in each height range plotted in Fig. 3.3. Note that in Fig. 3.4 vertical scales for spectra indicated as (A), (C) and (E) are shown on the left, while those for (B) and (D) are on the right, respectively. A 90% confidence interval for each spectrum is shown as a vertical bar in Fig. 3.4, which is calculated by using a method described by Blackman and Tukey [1959].

The spectra in region (A) are quite similar for the two observation periods; their logarithmic slopes were about -1.3, which are much smaller than the model prediction (-3), furthermore, the observed spectral amplitudes were smaller than the model for $m < 2 \times 10^{-3}$ cyc/m by a factor of roughly 10^{-2}. On the other hand, the spectra in region (E) showed fairly good agreement with the model as to both slope and amplitudes, except for in the large wavenumber range of the zonal component in Fig. 3.4a.

So far we have shown the characteristics of gravity waves determined from the MU radar observations, i.e., those in the mesosphere are well organized according to the saturated gravity wave theory, while in the lower stratosphere gravity waves are not fully saturated. The large change in the spectral shape between regions (A) and (E) can be interpolated from the rocketsonde results determined in the intermediate height ranges. In region (B), where the lower part of the height range overlaps with that in region (A), the spectral slopes are again more gradual than -3 and the spectral amplitudes are considerably smaller than the model. The origin of spectral peaks near $m = 1 \times 10^{-3}$ cyc/m

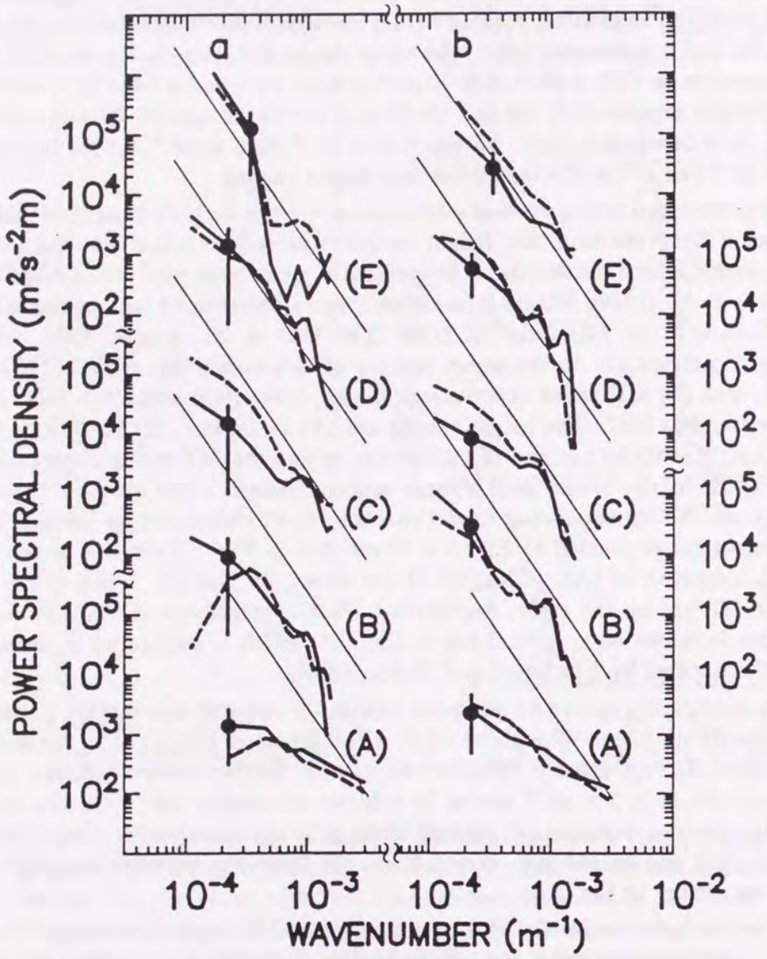

Figure 3.4: Vertical wavenumber spectra of the meridional (dashed) and zonal (solid) wind fluctuations observed with the rocketsondes and the MU radar. The (a) left and (b) right spectra present the results obtained on 20 August 1986 with MT135-45, and on 9 September 1987 with MT135-47 and 48, respectively. The model spectrum is also plotted by using N_b^2 shown in Fig. 3.3. Vertical axis for (A), (C) and (E) is plotted on the left, while that for (B) and (D) is shown on the right. A vertical bar indicates 90% confidence interval.

in both Fig. 3.4a and b is not clearly understood, but they might be due to the poor height resolution of the rocketsonde sounding, because these enhancements are not indicated by the MU radar observations in region (A).

In region (C), the spectral slopes and amplitudes are still more gradual and smaller than the model, respectively, although the spectra approach the model values. The entire shape of the spectra in region (D) becomes fairly close to the model curve; the slope is approximately –3 and the amplitudes agree relatively well with the model except for the enhancement for $m > 8 \times 10^{-4}$ cyc/m. It is noteworthy that the meridional component has larger amplitudes than the zonal one at a small wavenumber (large vertical scales).

The overall structures of these spectra are quite similar in each height region despite the difference in observation years, suggesting small year-to-year variation in the behavior of gravity waves. The spectral slope becomes steeper with a higher altitude, and reaches –3, which is predicted with the model at about 40–50 km, in the upper stratosphere.

The spectral amplitudes are generally smaller than the model in the lower stratosphere, although the discrepancy is relatively smaller at higher altitude regions, then the amplitudes become fairly close to the model values in the upper stratosphere and mesosphere. A bend in spectra at small wavenumbers, which is expected from the saturation theory in Fig. 1.6 seems to appear at low altitude regions, however, one is not recognized in the mesosphere within the observed wavenumber range.

The wind velocity variance, $\overline{u'^2}$, is calculated by integrating the spectra in the wavenumber range from m_1 to m_2 as

$$\overline{u'^2} = \int_{m_1}^{m_2} F_u(m)\mathrm{d}m. \tag{3.1}$$

Note that the wavenumber ranges are not the same for five height regions, that is, (m_1, m_2)= (2.3×10^{-4} m^{-1}, 3.2×10^{-3} m^{-1}) and corresponding scales 4.4 to 0.3 km for the region (A), (1.1×10^{-4} m^{-1}, 1.6×10^{-3} m^{-1}), 9.0 to 0.6 km for (B), (C) and (D), and ($1.7 \times^{-4}$ m^{-1}, $1.5 \times^{-3}$ m^{-1}) and 6.0 to 0.7 km for (E). Now we define in the following the normalized variance, α, as a ratio of the observed variance to a theoretical prediction assuming that gravity wave components for $m_1 \le m \le m_2$ are saturated

$$\alpha = \frac{\int_{m_1}^{m_2} F_u(m)\mathrm{d}m}{\int_{m_1}^{m_2} F_u^s(m)\mathrm{d}m} = \frac{\overline{u'^2}(\text{observation})}{\overline{u'^2}(\text{theory})} \tag{3.2}$$

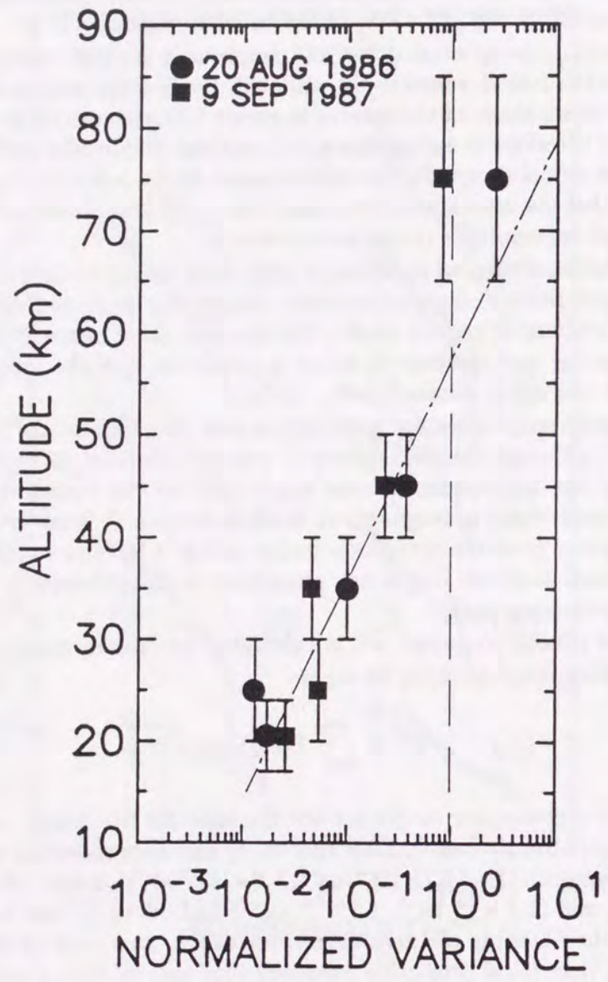

Figure 3.5: Height variation of the normalized variance (see text). The circles and squares denote the observations on 20 August 1986 and 9 September 1987, respectively, the vertical bars indicating the height regions. The chained line approximates the exponential growth of the normalized variance in the stratosphere.

The mean value of α between the meridional and zonal determinations is plotted in Fig. 3.5. When α reaches the unity, wind fluctuations are described by the saturated gravity wave theory.

α in region (A) was about 1.5×10^{-2} and 2.5×10^{-2} on 20 August 1986 and 9 September 1987, respectively. In region (C) α ranged from 0.05 to 0.1. α in region (B), which partially overlaps (A), is generally in between those in regions (A) and (C). α increases to 0.2–0.4 in region (D), clearly showing the asymptotical growth of α. While in region (E), α on 9 September 1987 is close to unity, that on 20 August 1986 slightly exceeds 1. The overall height profile in Fig. 3.5 indicates the clear tendency that α increases with altitude, and asymptotically approaches unity.

The normalized variance due to gravity waves in the stratosphere increase their amplitudes propagating upward and are hence considered not to be fully saturated. Their growths on 20 August 1986 and 9 September 1987 can be approximated by the chained line in Fig. 3.5 in the height region of 17–50 km. Assuming that the Brunt-Väisälä frequency is constant in the stratosphere, the e-folding height H_E of the exponential growth for the wind velocity variance with vertical scales smaller than about 10 km can be inferred as about 9 km from the figure. The values of α in the mesosphere were close to unity, suggesting that the mesospheric wind fluctuations are well described by the saturated gravity wave model. It is clear that α in the mesosphere was significantly smaller than the linearly extrapolated value based on the stratospheric results, implying that the gravity waves cease increase of wave amplitudes in the mesosphere, due to wave saturation.

Spectra in Winter (January and February 1990)

We conducted similar spectral analyses for observations with the MU radar and rockets in January and February 1990, during the DYANA campaign. We again separated the entire height range into five altitude regions, with a thickness of about 10 km, having a nearly constant N^2 value; the lower stratosphere at 17–23 km (A), the middle stratosphere at 22–32 km (B), the upper stratosphere at 33–43 km (C), the lower mesosphere at 47–56 km (D) and the upper mesosphere at 65–85 km (E). We used the MU radar data for the regions (A) and (E) and the rocketsonde soundings for the other height regions. The mean values of N^2 were 6.53×10^{-4} (A), 4.85×10^{-4} (B), 4.88×10^{-4} (C) and 3.48×10^{-4} (D) $(\mathrm{rad/s})^2$, respectively, which were estimated from the mean temperature profile obtained with the rocketsonde soundings and routine radiosondes. Note that N^2 in region E was assumed to be 3.45×10^{-4} $(\mathrm{rad/s})^2$ from the CIRA 1986 model, since a simultaneous temperature profile was not available.

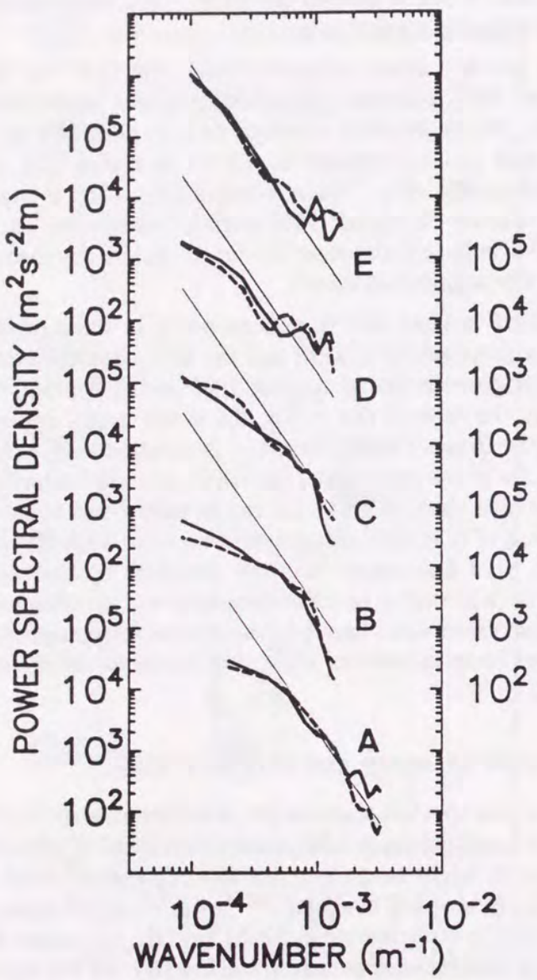

Figure 3.6: Vertical wavenumber spectra of the meridional (dashed) and zonal (solid) wind fluctuations observed with rocketsondes and the MU radar. The top and bottom spectra correspond to the mean results for the entire MU radar observations during the DYANA campaign, while the middle three spectra are the means of eight determinations from the rocketsonde measurements (see text). The model spectrum is also plotted, using the observed N^2 (see text for details).

The spectra were first determined in the five height ranges by using the individual profiles, and then the mean of the eight spectra was calculated, as illustrated in Fig. 3.6, where the straight lines, having a logarithmic slope of –3, are the corresponding model saturated spectra obtained with (1.8), which were calculated by using the N^2 values in each height range. Note that the analyzed wavenumber range in the lower stratosphere was greatly different from the others because of the better height resolution and the smaller height range.

There was a large change in the spectral shape between the lowest and highest regions, but the variations seemed to be fairly well interpolated by the results for the intermediate height ranges. The spectral amplitudes for small wavenumbers, for example, m=2×10^{-4} cyc/m (or 5 km in wavelength, λ_z) showed a clear increase with altitude, i.e., they were 2–3×10^4 (m^3/s^2) in regions A and B, increased to 4–8×10^4 and 6–8×10^4 (m^3/s^2) in C and D regions, respectively, and then finally became 2–3×10^5 (m^3/s^2) in region E.

By comparing the observed values with the model prediction, it can be suggested that the wave components with m=2×10^{-4} cyc/m (λ_z=5 km) were not saturated in the lower stratosphere, being one-tenth of the model value, therefore they were able to increase in amplitude with altitude in the stratosphere and lower mesosphere, and finally reach their saturation values in the upper mesosphere. On the other hand, the spectral amplitudes with larger m did not show an increase with altitude, but they were fairly constant in all the height ranges, indicating that the spectral amplitudes were limited by the saturated values, which is consistent with the theoretical prediction.

Moreover, the spectral shape varied with the wavenumber, that is, the spectral slope was generally gradual for a small m, where the gravity waves were not fully saturated, while it became steeper for a large m, approaching the model value of –3. However, the spectral shape also changed with altitude, which can be recognized by the mean slope for $m \leq 4\times10^{-4}$ cyc/m, which was estimated to be –0.7, –1.0, –1.8, –2.6 and –3.0 from the lower to higher regions in Fig. 3.6, respectively.

In other words, the wavenumber range of the saturated components increased with altitude. In the stratosphere only the gravity waves with a large wavenumber were saturated, while all the components within the entire observed wavenumber range seemed to satisfy the saturation condition in the upper mesosphere. The general characteristics of the spectra described above are again quite similar to the results in August and September with MT135 rockets.

We now quantitatively estimate the increase in the gravity wave energy per unit mass by analyzing the integrated wind velocity variance from the spectra in the two wavenumber ranges; (i) $10^{-4} \leq m \leq 2\times10^{-4}$ (or $5 \leq \lambda_z \leq 10$ km) and (ii) $2\times10^{-4} \leq m \leq 10^{-3}$ (or $1 \leq \lambda_z \leq 5$ km). The wind velocity variance normalized as

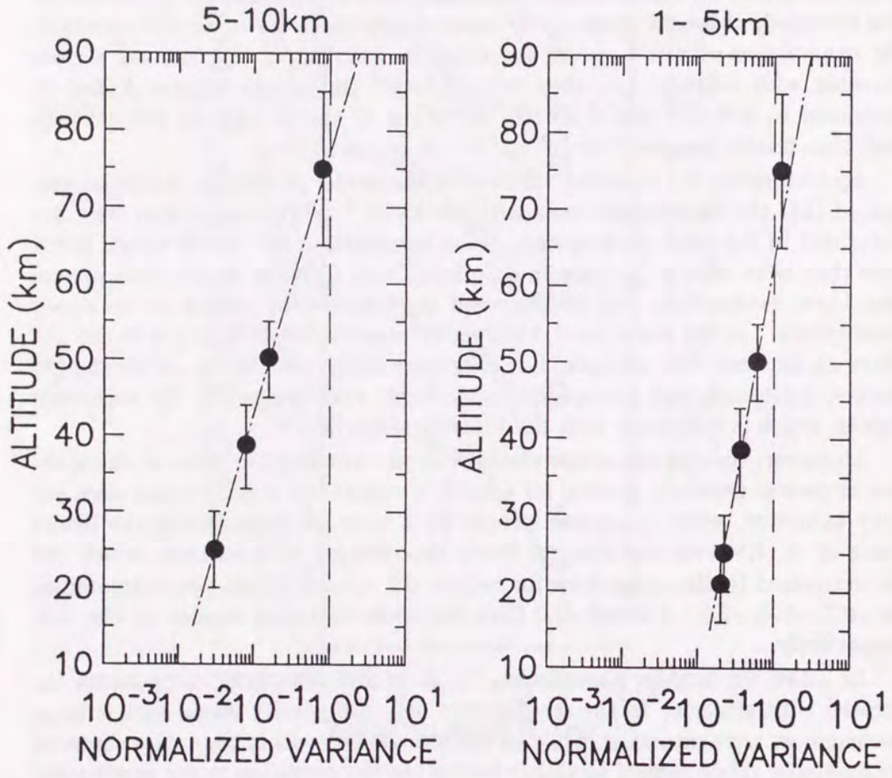

Figure 3.7: Height variation in the normalized variance in the two wavenumber ranges, i.e., (i) $10^{-4} \leq m \leq 2 \times 10^{-4}$ cyc/m (5–10 km) (left) and (ii) $2 \times 10^{-4} \leq m \leq 10^{-3}$ cyc/m (1–5 km) (right). The dot-dash lines indicate the asymptotic increase in the observed values.

to the model value is shown in Fig. 3.7, being the mean value between the zonal and meridional components, which indicates the index of the gravity wave saturation in the corresponding wavenumber ranges [Murayama et al., 1992a]. The integrated variance in the lower stratosphere is not shown in Fig. 3.7a, because the observed wavenumbers were not extended widely enough to include range (ii).

Although the two sets of results in Fig. 3.7 similarly showed the exponential growth of the variance with altitude, the scale height was greatly different between the wavenumber ranges (i) and (ii), which can be estimated to be about 15 km and 25 km, respectively. Note also that the values in the upper mesosphere were close to unity in the two wavenumber ranges, suggesting that the gravity wave energy was limited by the saturated value predicted by the model.

If a gravity wave were free from any breaking processes including wave saturation, its wind velocity variance, or the wave energy per unit mass, should increase exponentially with a scale height equal to that for the density decrease (approximately 7 km in the middle atmosphere). The observed scale height in wavenumber range (ii) was obviously larger than this value, indicating that the rate of energy loss was greater for gravity waves with a smaller λ_z. Moreover, even in wavenumber range (i), the scale height was twice larger than the density scale height, suggesting that a part of the gravity waves also lost its energy in the course of the upward propagation.

Comparison between Summer and Winter Results

From the results so far in this section, we can find seasonal difference between the vertical wavenumber spectra observed in summer (August and September in 1985–1987) and winter (January–February 1990).

From vertical wavenumber spectra in summer and winter in Figs. 3.4 and 3.6, respectively, the spectra (A) in the lower stratosphere in winter showed steeper spectral slopes than in summer. The amplitudes in winter at wavenumbers higher than 6×10^{-4} cyc/m were as large as the model values and larger than in summer. In the height range of (B), the amplitudes in winter at wavenumbers of 6×10^{-4}–1×10^{-3} cyc/m were as large as the model value, which was larger than the summer spectra. So it is suggested that gravity waves with vertical wavelengths around 1 km tended to be saturated in winter in the lower stratosphere, while those in summer were not fully saturated.

For the spectra (E) in the upper mesosphere, the spectral densities in both in summer and winter agreed well with the model values except for the zonal component at wavenumbers higher than 5×10^{-4} cyc/m in Fig. 3.4, implying

that gravity waves with vertical wavelengths of about 1–10 km were saturated in both summer and winter.

The normalized variances in summer and winter in Figs. 3.5 and 3.7, respectively, suggest the seasonal difference of the height variation of gravity wave energy. Although the integration ranges in Fig. 3.5 which were the entire wavenumber ranges were different from the ranges (i) and (ii) in Fig. 3.7, it is possible to compare the altitude increases in summer with the winter results in the integration range (i) (5–10 km) because the low wavenumber component is generally dominant.

We can find that the normalized variance in the stratosphere and lower mesosphere in summer increased with the scale height H_E of about 9 km, which was more rapid than in winter in Fig. 3.7 (i) with H_E of 15 km. Although the mesospheric values were around unity in both summer and winter, the extrapolated value from the stratospheric growth in summer was much larger than the value of unity in winter. So it is suggested that gravity wave energy in the stratosphere and lower mesosphere in summer tended to increase with altitude more rapidly than in winter, and gravity waves in the mesosphere, however, remained about the values inferred from the saturated spectrum model both in summer and in winter probably due to the gravity wave saturation.

3.3 Significance of the Stratopause on the Upward Propagation of Gravity Waves

Profiles of Wind Velocity Variance

We are interested in this section in the fine structure of the height variations of the gravity wave energy. The spectral analysis presented in the previous section may not be suitable for this purpose, since it requires a fairly large height range, covering the large vertical scales in the wavenumber spectra. We present here profiles of the wind velocity variance, which were calculated from the wind velocity profiles after processed through band-pass filters. The data analyzed in this section are obtained from the Super Loki and Viper rocket observations at Uchinoura during the DYANA campaign, and the simultaneous MU radar observations. Wind velocity fluctuations were extracted through the band-pass filter and then were running-averaged with the vertical scale of the larger cutoff scale of the pass-band, to results in the wind velocity variance vs. height. We have selected three different pass-bands of 3.5–1.5 km, 6.0–4.0 km and 12.0–6.0 km (these scale ranges are hereafter referred to as (a), (b) and (c), respectively).

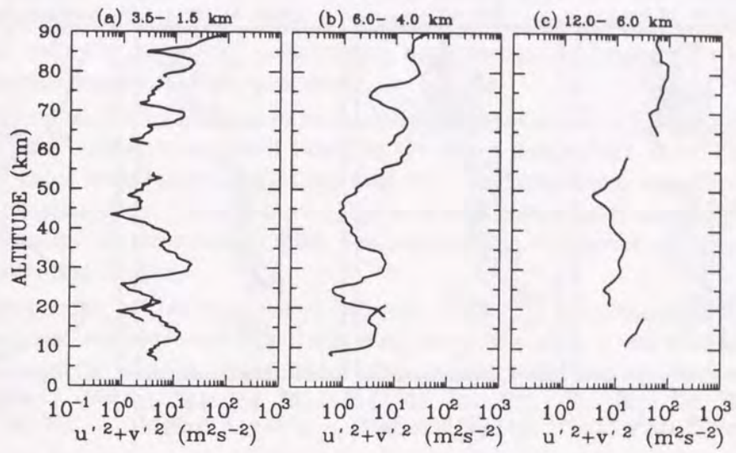

Figure 3.8: Profiles of the wind velocity variance, $\overline{u'^2}+\overline{v'^2}$, observed on 24 February 1990 with a rocketsonde at 15–60 km and the MU radar in two height ranges, 5–20 km and 60–90 km. Before calculation of $\overline{u'^2}+\overline{v'^2}$, band-pass filters with pass-bands of 3.5–1.5 km (left), 6.0–4.0 km (center) and 12.0–6.0 km (right) were applied.

The sum of the wind velocity variance between the zonal and meridional components, $\overline{u'^2}+\overline{v'^2}$, is shown in Fig. 3.8 for the measurements 24 February 1990. Although the statistical results as to the wind velocity variance shown in Fig. 3.7 exhibited asymptotic growth, being approximated by the exponential curve with the constant scale heights, the detailed profile of $\overline{u'^2}+\overline{v'^2}$ in Fig. 3.8 involved great variability.

The values of $\overline{u'^2}+\overline{v'^2}$ below 20 km, detected with the MU radar, ranged up to 10 (m^2/s^2) in scale range (a), while they were about 1/3 in range (b), which is consistent with the fact that the vertical scales of the dominant gravity waves are 2–3 km there, as shown in the previous section. It is noteworthy that the considerably large $\overline{u'^2}+\overline{v'^2}$ values in range (c) and a part of (b) were reflected by the vertical structure of the jet stream, therefore, they did not fully represent the gravity wave energy in the lower atmosphere.

Comparison of the absolute values of $\overline{u'^2}+\overline{v'^2}$ between the three scale ranges may not be very meaningful, because the bandwidths for the three ranges are not uniform. However, investigations of their height variations would be quite interesting. The profiles in Fig. 3.8 were fairly continuous between the rocket-

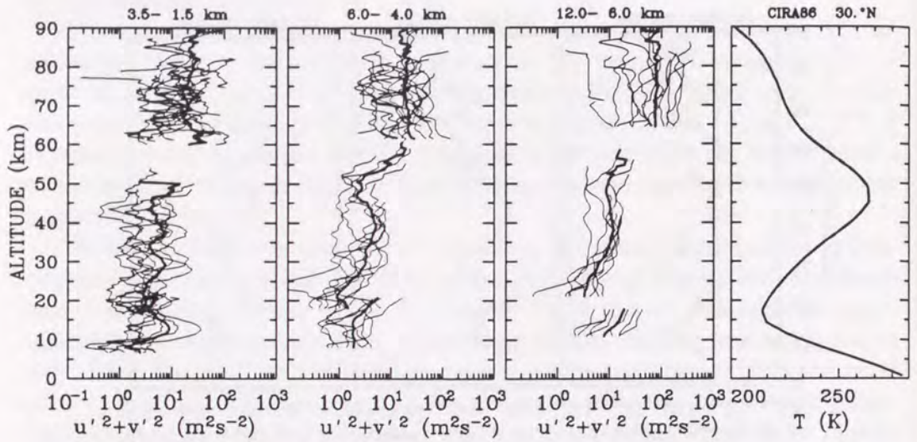

Figure 3.9: The same as Fig. 3.8 except that all the profiles were obtained during the DYANA period. The thick line indicates the mean value. A temperature profile taken from the CIRA 1986 model is also illustrated.

sonde and the MU radar observations, suggesting the overall consistency of the profiles obtained with the two different observation techniques. The values of $\overline{u'^2}+\overline{v'^2}$ became decreased at 20–25 km in all the three scale ranges, and then showed enhancement near 30 km. They again became small near 45 km, and then increased exponentially at 45–60 km altitude, showing a continuous profile to the values in the mesosphere obtained with the MU radar. The values of $\overline{u'^2}+\overline{v'^2}$ above 60 km did not show significant height variations, and they had a rather constant value in the entire height range. The maximum $\overline{u'^2}+\overline{v'^2}$ values in range (a) were nearly the same between the lower stratosphere and the mesosphere, while they increased by a factor of about 10 in ranges (b) and (c).

Figure 3.9 presents all the profiles of $\overline{u'^2}+\overline{v'^2}$, collected during the DYANA campaign, together with the mean values in each scale range, where the zonal mean temperature derived from the CIRA 1986 model is also illustrated. The general characteristics of $\overline{u'^2}+\overline{v'^2}$ profile, described concerning Fig. 3.8, are more generally recognized by the mean profile in Fig. 3.9. In particular, the mean profile corresponding to scale range (b) most clearly exhibited the variations, that is, $\overline{u'^2}+\overline{v'^2}$ showed a decrease near 20 km, rapidly increased at 20–28 km, and then showed a rather gradual increase up to 40 km.

Then the values of $\overline{u'^2}+\overline{v'^2}$ decreased in the narrow height range of 45–50 km.

The depressions coincided with the stratopause height, which can most clearly be recognized in scale range (b). Although such a tendency was not so clear in the mean profile in scale range (a), the individual profile shows a fairly deep narrow valley at 40–45 km, suggesting a large change in the characteristics of the gravity waves near the stratopause.

The values of $\overline{u'^2}+\overline{v'^2}$ again exponentially increased at 50–60 km. It is striking that $\overline{u'^2}+\overline{v'^2}$ exhibited constant values in the upper mesosphere above 65 km in all the three scale ranges, indicating that the wave amplitudes were limited by the wave saturation. Note, however, that such a saturated value can more clearly be recognized in the mean profiles, but considerable deviations can be seen in the individual profiles.

Comparison of the mean values between 25 and 65 km altitude shows that the increase in $\overline{u'^2}+\overline{v'^2}$ was only 6.6 in scale range (a), while it was about 12 and 18 in ranges (b) and (c), respectively, being generally consistent with the results in Fig. 3.7.

Effect of the Stratopause Structure on the Gravity Wave Propagation

We study here the vertical structure of the wind velocity variance, particularly, for the wave components with relatively small vertical scales, focusing on the effect of the decrease in the static stability near the stratopause on the upward propagation characteristics of gravity waves.

The profiles obtained with all the falling sphere soundings and the datasonde measurement on 20 January 1990 could not be included in the present analysis, since a temperature profile, which is essentially important for describing the underlying physical mechanism, was not obtained for any of them. Furthermore, the two cases observed with datasondes on 29 and 31 January were also not used, because the stratopause was not clearly detected. Therefore, only the two profiles obtained on 17 January and 5 February 1990 are treated in the following.

The profiles of wind velocity and temperature fluctuations, after applying band-pass filters with cut-offs at 1.5 and 3.5 km, are presented in Fig. 3.10 for the results obtained on 17 January. Investigation of Fig. 3.6 suggests that the components within the above-stated vertical scales were not fully saturated, but they seemed to be marginally saturated in the upper stratosphere. The stratopause, with a maximum temperature of about 268 K, was detected at 46 km altitude, coinciding with the sharp decrease in the N^2 values with a ratio of about 0.5. The amplitudes of the zonal and meridional wind velocity fluctuations, u' and v', in Fig. 3.10 linearly increased at 35–45 km, and then abruptly decreased above the stratopause. The wind velocity variance, $\overline{u'^2}+\overline{v'^2}$, in Fig. 3.10 decreased at 45–50 km to become 1/4 in comparison with the value below the stratopause.

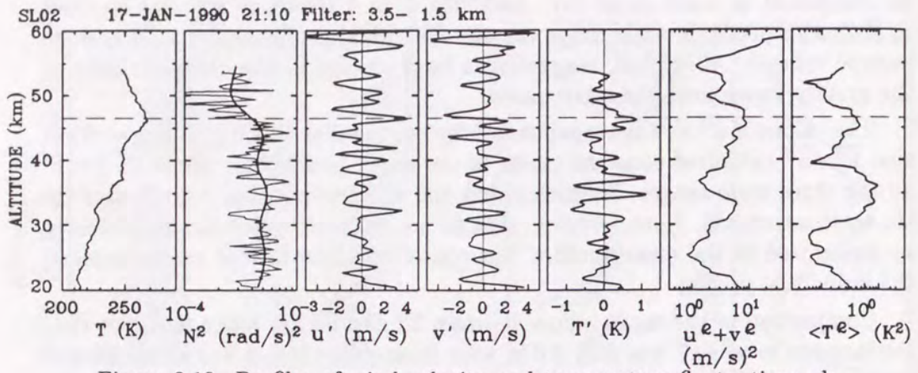

Figure 3.10: Profiles of wind velocity and temperature fluctuations observed with the rocketsonde launched at 21:10 LT on 17 January 1990. The left-most panel shows the temperature profile. The next panel shows the fine structure of N^2 with a resolution of 300 m, together with a smoothed profile after applying a low-pass filter with a cut-off of 10 km. Successive three panels show fluctuating components, after applying a band-pass filter (1.5–3.5 km), for the eastward and northward wind velocity and temperature. The right two panels show the variance of wind velocity and temperature. The horizontal thin dashed line indicates the altitude corresponding to $N = 4\times10^4$ (rad/s)^2.

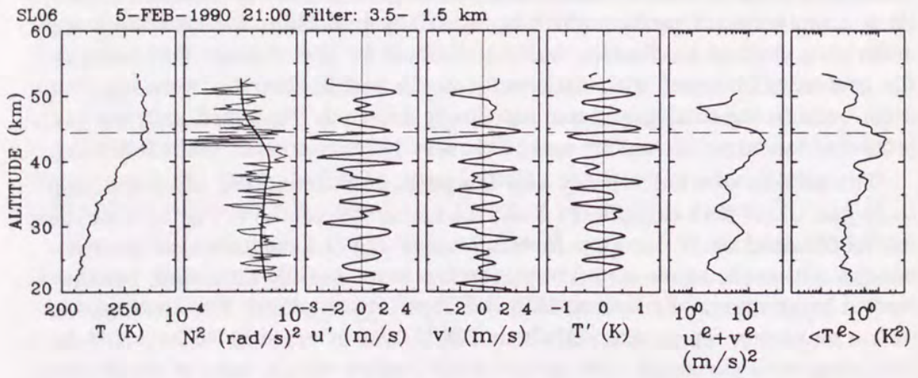

Figure 3.11: The same as Fig. 3.10 except that the results were obtained with the rocketsonde launched at 21:00 LT on 5 February 1990.

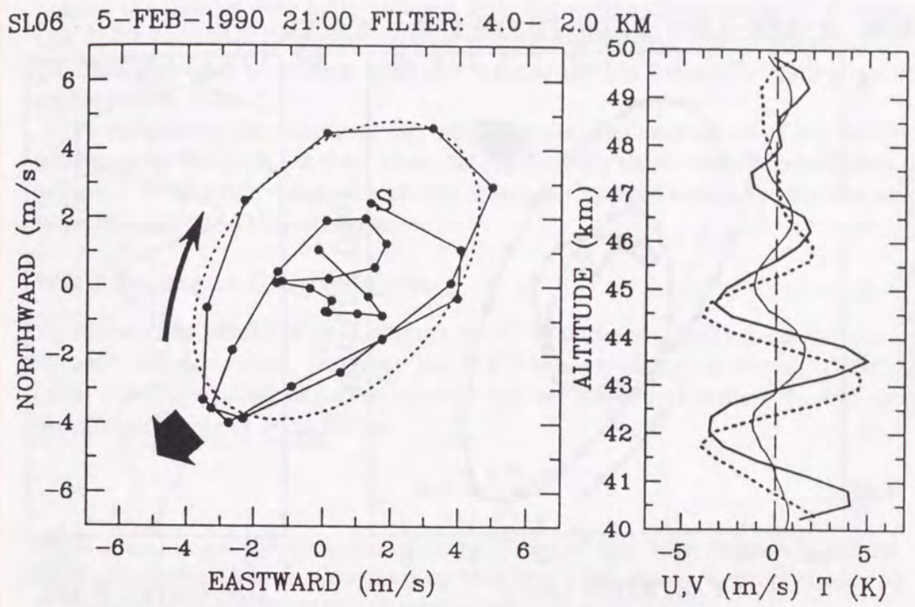

Figure 3.12: Hodograph (left) for the gravity wave, with relatively short vertical scales, determined from the wind velocity profiles collected on 5 February 1990 by applying a band-pass filter (2–4 km). The best-fitted ellipse is also illustrated by the dotted line. The lowest data point is indicated by "S", and the arrow indicates the rotation direction with altitude. The right panel shows the filtered profiles of the eastward (thick solid line) and northward wind velocity (dotted line), and temperature (thin solid line).

However, the variance of the temperature fluctuations, $\overline{T'^2}$, in Fig. 3.10 showed a relatively smaller decrease in amplitude in the corresponding altitude ranges.

Another example is presented in Fig. 3.11 for the measurements on 5 February. It can be clearly recognized that the wind velocity fluctuations suddenly stopped growing just above the stratopause, showing a decrease of $\overline{u'^2}+\overline{v'^2}$ by a factor of almost 1/10 around 45 km. Moreover, the temperature fluctuations also exhibited similar height variations accompanied with a decrease in $\overline{T'^2}$ by a factor of 1/5. Large variations in the N^2 values in Fig. 3.11 occurred at around 42 km, indicating the stratopause height, although the smoothed N^2 profile

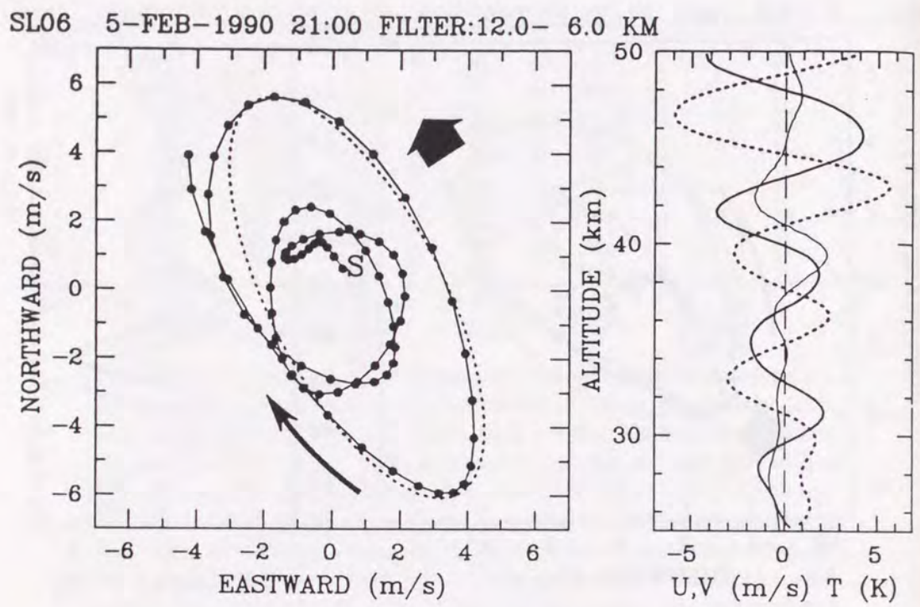

Figure 3.13: The same as Fig. 3.12 except for the gravity wave component with a larger vertical scale, obtained by changing the pass-band to 6–12 km.

showed a relatively small decrease in N^2, by a factor of about 0.6, below and above the stratopause.

In order to analyze the characteristics of the gravity waves detected in Fig. 3.11 in more detail, we present in Fig. 3.12 a hodograph for the components with $2 \leq \lambda_z \leq 4$ km. The hodograph clearly exhibits the clockwise rotation with altitude, which is consistent with a gravity wave with upward energy propagation [e.g., Hirota and Niki, 1986; Yamamoto et al., 1988b; Tsuda et al., 1990a]. The linear polarization relations of gravity waves, applied between the wind velocity and temperature fluctuations, suggest that the horizontal propagation direction of this gravity wave was south-westward. The amplitudes of u' and v' were about 5 ms^{-1} below 45 km, while they decreased to about 2 ms^{-1} above 47 km, giving an amplitude ratio of approximately 0.4.

Figure 3.13 shows a hodograph for the component with relatively large vertical scales ranging from 6 to 12 km, which again showed the clockwise rotation,

while the horizontal propagation was north north-westward. The height variations of the profiles were quite different from the results shown in Fig. 3.12, such that the amplitudes increased with an exponential growth rate of about 12–15 km, being roughly consistent with the scale height estimated for the variance profile in Fig. 3.7a.

To summarize the results so far, we found that the amplitudes of the small-scale gravity waves ($\lambda_z \sim 2$–3 km) became significantly small just above the stratopause. On the other hand, the gravity waves with larger vertical scales seemed to be insensitive to the stratopause.

WKB Scaling of Gravity Waves

We discuss the effects of the decrease in N^2 near the stratopause on the gravity wave characteristics, assuming the WKB scaling of gravity waves, which is based upon the proportionality between the vertical wavenumber, m, and the background value of N as follows

$$m = -\frac{kN}{\omega} \tag{3.3}$$

where k and ω are the horizontal wavenumber and the wave frequency, respectively. Equation (3.3) further predicts that the wave energy is proportional to N [VanZandt and Fritts, 1989 (hereafter referred to as VF89)].

On the basis of the saturation theory, VF89 discussed the effect of the increase of N^2 on the gravity wave characteristics, by assuming the condition near the tropopause or the mesopause, and predicted that the wave energy increases by a factor of N^3 due to WKB scaling of the wave, and then the energy increase is finally limited as to N^2 because of the enhanced dissipation of gravity waves.

Although VF89 did not explicitly describe it, the WKB scaling method seems to be applicable to the opposite case, being defined as "subsaturation", where the N^2 values decrease in the interface region between the atmospheric layers, as seen near the stratopause. In such a situation, the spectral amplitudes for $m \gg m_*$ decrease by a factor corresponding to the ratio of the N^3 values in the two regions above and below the stratopause.

In order to test the proportionality of m to N, as described in (3.3), we first investigate the case for $m \ll m_*$, as shown in Fig. 3.13. The values of m for the northward component in Fig. 3.13 can be estimated to be 1/6.7 and 1/7.9 c/km near 35 and 45 km altitude, respectively, giving a decrease of m by a factor of about 0.85 below and above the stratopause. While the reduction in N was about $\sqrt{0.6}$=0.77, showing reasonable agreement with the prediction of the WKB scaling. Although the WKB scaling also predicts the decrease in the wind velocity variance as N near the interface region, it was not clearly recognized

because of the small height range above the stratopause in comparison with the vertical wavelength of the gravity wave.

We now apply the WKB scaling to gravity waves with $m \gg m_*$. Using the smoothed profiles of N^2 in Figs. 3.10 and 3.11, the ratio of N^3 below and above the stratopause can be estimated to be 0.35 and 0.46, respectively. While, the decreases in $\overline{u'^2}+\overline{v'^2}$, as shown in Figs. 3.10 and 3.11, were 0.25 and 0.1, respectively. The fairly large discrepancy in the decrease ratios between the prediction and the observations suggests that the gravity waves might be very sensitive to sharp changes in the static stability, as detected in the detailed profiles of N^2 in Figs. 3.10 and 3.11, so the smoothed N^3 values may not be used to estimate the decrease in the gravity wave energy.

Investigation of the statistical results in Fig. 3.9 shows that the values of $\overline{u'^2}+\overline{v'^2}$ in scale range (b) were about 5.0 and 2.5 (m^2/s^2) at 40 and 48 km, which gives a decrease rate of 0.5, which is reasonably consistent with that for N^3. While in range (c), they were 12.0 and 9.0 (m^2/s^2) at 40 and 48 km, respectively, the ratio being estimated to be 0.75, which again approximately agreed with that for N. Therefore, WKB scaling can successfully explain the statistical behavior of the gravity wave variance, although it cannot fully account for the variations seen in the individual profiles.

In the case of subsaturation, the gravity waves are not saturated any more in the overlying region, thus they exponentially increase in amplitude, and finally again reach their saturation values, which is basically consistent with the profiles in Fig. 3.9.

3.4 General Behavior of the Profiles of Gravity Wave Energy

We describe here general characteristics of the gravity wave energy per unit volume, $E=1/2\rho(\overline{u'^2}+\overline{v'^2})$, using the results in Fig. 3.9, where ρ was taken from the CIRA 1986 model. Figure 3.14 clearly shows that E almost monotonously decreases through the entire height ranges, although the detailed structures were different depending on the scale ranges.

In scale range (b), E was fairly constant in the lower stratosphere below about 30 km, rather gradually decreased up to 45 km, then showed a rapid decrease at 45 km, and became fairly constant at 45–60km. Above 65 km, E again exponentially decreased at the scale height of ρ. The general characteristics were almost the same in scale ranges (a) and (c). However, the behavior of E at 45–60 km was not clearly recognized for scale range (a) because of the data gap between 50 and 60 km.

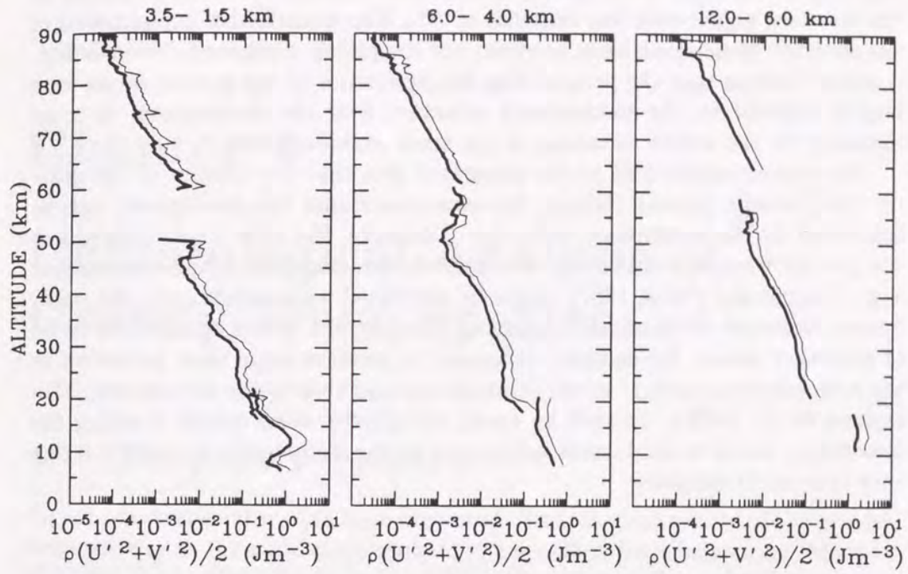

Figure 3.14: Profiles of $E=1/2\rho(\overline{u'^2}+\overline{v'^2})$ determined by using the profiles in Fig. 3.9.

It is noteworthy that the behavior of E at 45–60 km, being located just above the stratopause, was quite interesting, which strongly suggests that the gravity waves conserved their energy there, being quite different from the behavior in other height ranges. As a result, the dynamical coupling between gravity waves and the mean winds, which can be represented, for example, by the drag force due to wave breaking, seemed to cease in the lower mesosphere, and such a mechanism becomes predominant in the upper mesosphere.

The values of E at 65 km can be estimated to be 1.5×10^{-3}, 1.5×10^{-3} and 5.0×10^{-3} (J/m^3) for scale ranges (a), (b) and (c), respectively, the sum of which is 8.0×10^{-3} (J/m^3). Since E in the upper mesosphere approximately decreases as ρ, the empirical model of the E profile can be proposed to be $8.0\times10^{-3}\exp(65-h/6.5)$ (J/m^3), where h is the height in km. Because the vertical scale corresponding to m_* in the upper mesosphere seems to be close to or slightly larger than the maximum height coverage of the current observations, the total gravity wave energy seems to be a few times larger than the proposed model value.

To summarize the above discussion, the height variations of the wind velocity variance are related to the vertical structure of the static stability profiles, which

produces the changes in the gravity wave characteristics due to WKB scaling at the interface region with the decrease in N^2. The quantitative explanations of the observed phenomena were, however, not completely confirmed. Nevertheless, it seems obvious that the propagation characteristics of the gravity waves were largely affected by the temperature structure near the stratopause, or more explicitly by the height variations of the static stability there.

The current study lead to the important idea that the amount of the gravity wave energy, passing through the stratopause into the mesosphere, can be controlled by the stratopause structure. Therefore, the large time variations in the gravity wave activity in the mesosphere, detected with radar observations [e.g., Vincent and Fritts, 1987], might be correlated with variations in the stratopause structure. Stratospheric warming accompanied by the enhanced activity of planetary waves, for instance, is known to produce large time variations in the temperature structure in the stratosphere and even in the mesosphere [Murayama et al., 1992b]. In such an event, the gravity wave energy reaching the mesosphere could be modulated in response to the disturbed temperature structure near the stratopause.

Chapter 4

Climatological Analysis of Gravity Wave Spectra

4.1 Frequency Spectra

Recent observational studies have presented climatological results of the gravity wave activity in the middle atmosphere in a specified frequency range [Meek et al., 1985; Reid, 1986; Tsuda et al., 1990b; Vincent and Fritts, 1987]. Meek et al. [1985] and Vincent and Fritts [1987] showed time-height cross sections of power spectral density in the mesosphere and lower thermosphere. Tsuda et al. [1990b] presented seasonal variation of gravity wave activity in the mesosphere. Their results exhibited a semiannual variation of gravity wave activity in the mesosphere with summer and winter maxima, and equinoctial minima.

Yamamoto et al. [1986] showed bimonthly averaged frequency spectra in 1983–1985 by using the Kyoto meteor radar observations at 90–100 km, but they found no clear seasonal variation of the spectral density for the periods of 2–6 hr.

In this section, we present the climatological results of gravity wave spectra vs. frequency observed with the MU radar, and also show the spectral shape changes depending on the background wind.

4.1.1 Seasonal Variations

From the MU radar observations of wind velocity, continued for about four days a month, from December 1985 to December 1989 in the troposphere and lower stratosphere, we calculated monthly mean frequency spectra of vertical and zonal and meridional oblique wind velocities at a zenith angle of 10°. We picked up the spectra in a period range of 5 min–21 hr in three height ranges

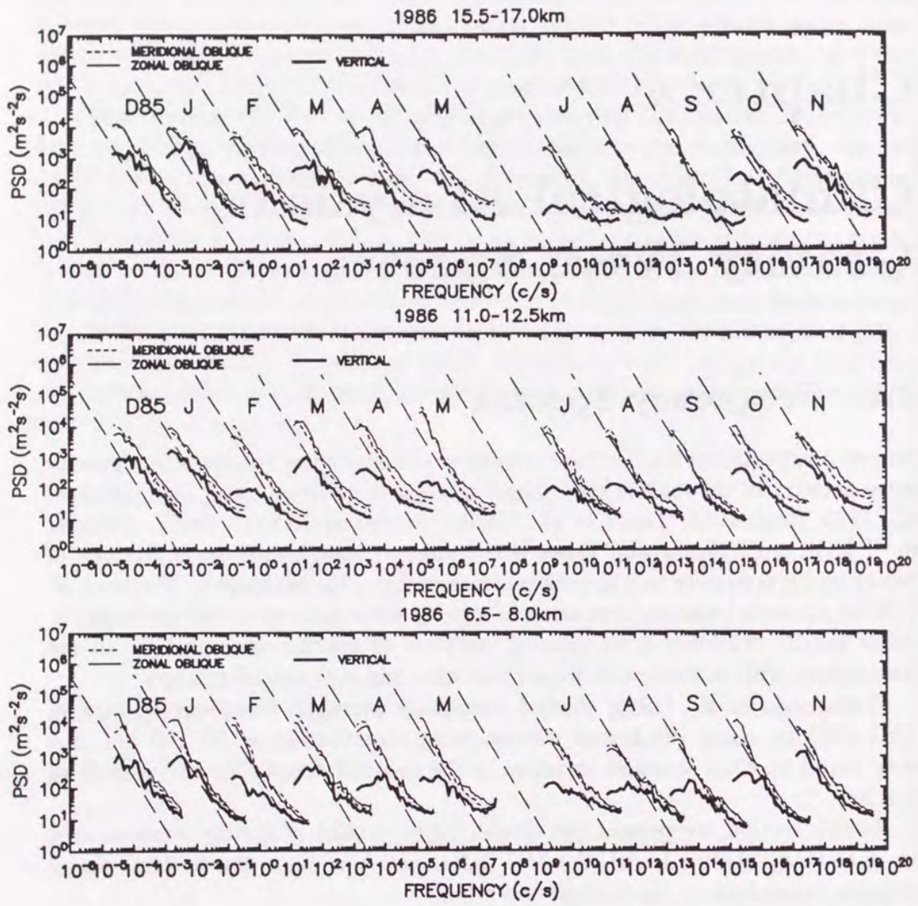

Figure 4.1: Monthly mean frequency spectra of vertical (thick solid), zonal oblique (thin solid) and meridional oblique (short dashed) wind velocity in the height ranges of 15.5–17 km (top), 11–12.5 km (middle) and 6.5–8 km (bottom) from December 1985 to November 1986. Spectra in each month are shifted by 10^2 Hz. Long dashed lines represent the curve with a slope of $-5/3$ and a fixed amplitude for reference.

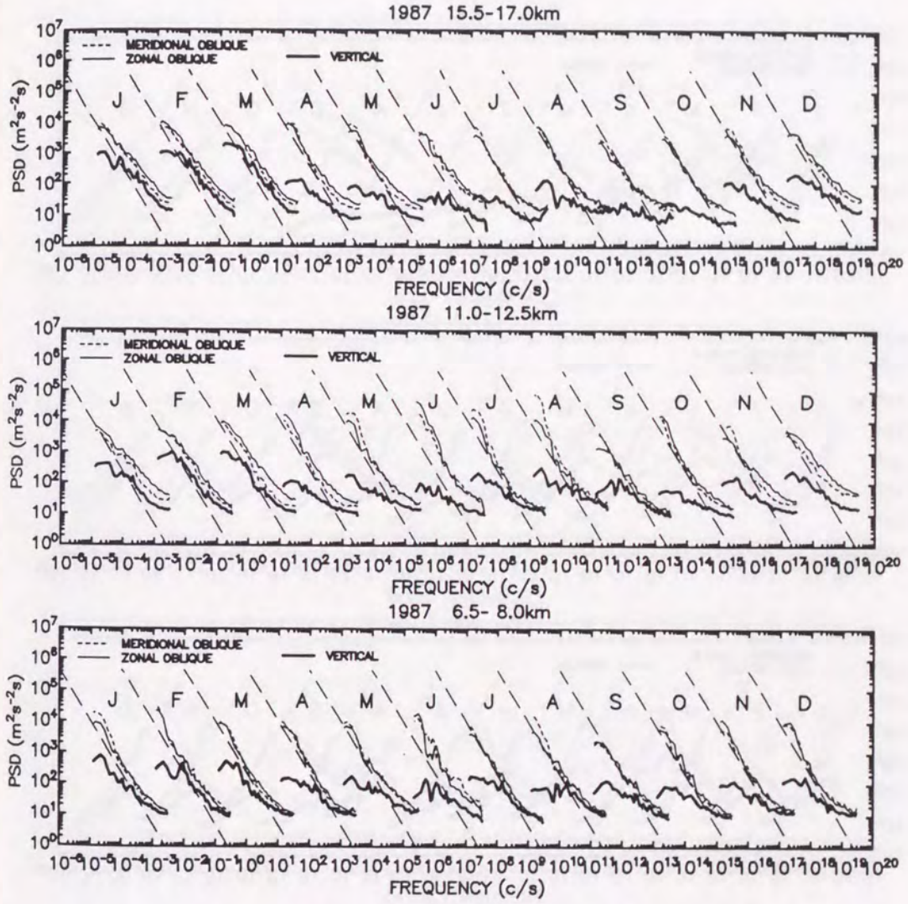

Figure 4.2: The same as Fig. 4.1 except for data in 1987.

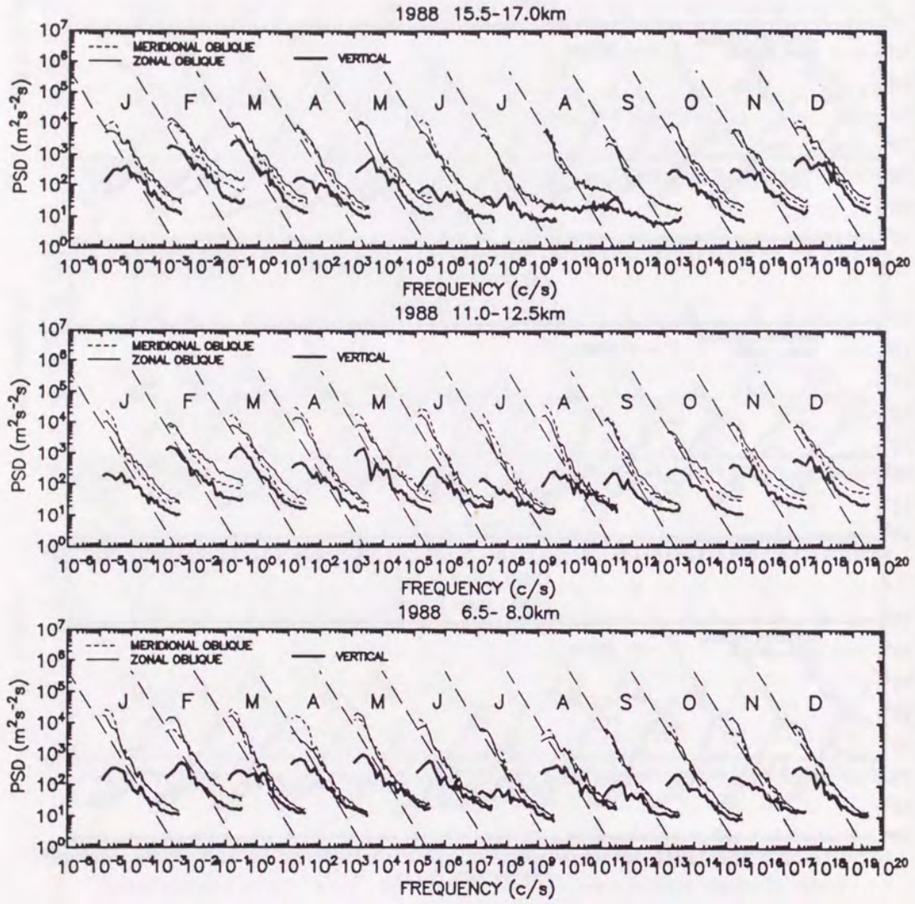

Figure 4.3: The same as Fig. 4.1 except for data in 1988.

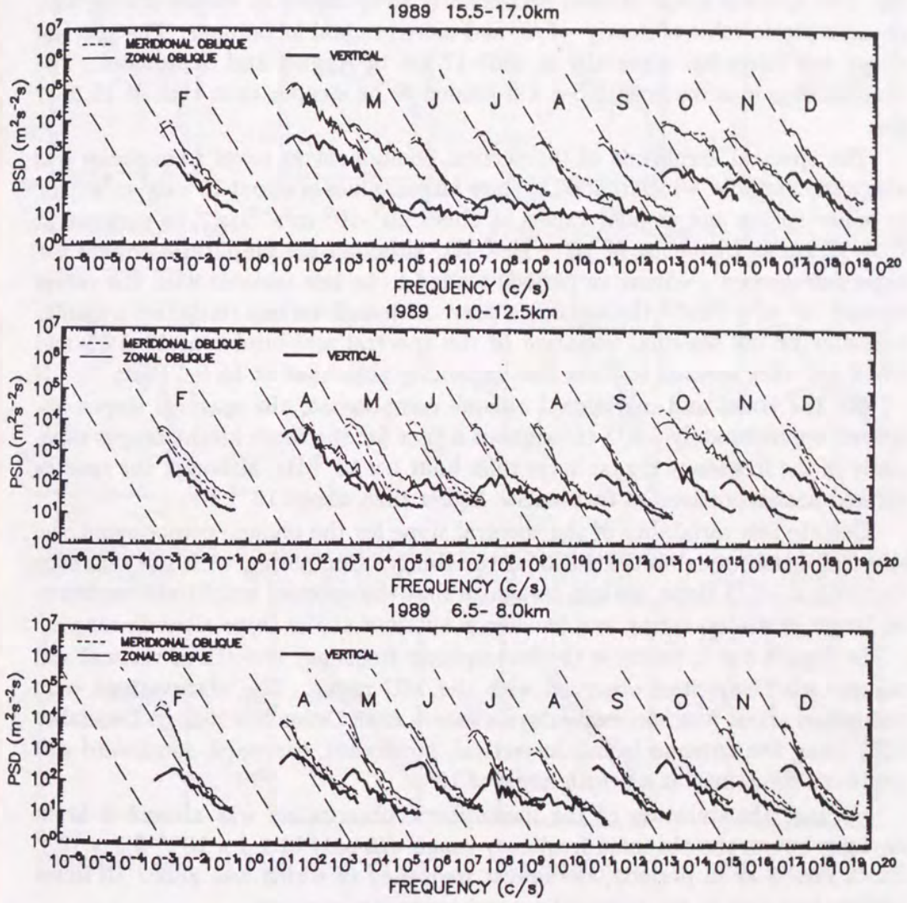

Figure 4.4: The same as Fig. 4.1 except for data in 1989.

of 15.5–17, 11–12.5 and 6.5–8 km, as shown in Figs. 4.1–4.4. 21 hr corresponds to the inertial period at the MU radar site, and 5 min is a typical value of the Background Brunt-Väisälä frequency in the middle atmosphere.

The monthly frequency spectra of vertical wind velocity showed large variability in both slope and amplitude in the frequency range lower than 1×10^{-3} Hz. The spectral shape showed significantly steep slopes in winter–spring with an asymptotic value of nearly $-5/3$, and more gradual in summer. The spectral shape was fairly flat especially at 15.5–17 km in August and September. The spectral slop in summer at 6.5–8 km tended to be steeper than that at 15.5–17 km.

The spectral amplitude of the vertical component at lower frequencies was also fairly variable, which tended to show larger values of about 10^2–10^3 $m^2s^{-2}Hz^{-1}$ in winer–spring and smaller values of about 10^1–10^2 $m^2s^{-2}Hz^{-1}$ in summer at 15.5–17 km at frequency of 1.3×10^{-5} Hz, although the amplitude around the highest frequency (∼5 min in period) tended to be less variable with the values around 10^1 $m^2s^{-2}Hz^{-1}$ throughout a year. Although we can recognize a similar tendency of the seasonal variation of the spectral amplitudes at 11–12.5 and 6.5–8 km, they seemed to show less variability than that at 15.5–17 km.

For the zonal and meridional oblique components, the spectral slopes appeared approximately $-5/3$ throughout a year for the three height ranges especially in the frequency region lower than bout 1×10^{-3} Hz, although the spectra showed flatter portions at frequencies higher than about 10^{-3} Hz.

Despite less variability of the spectral slope for the oblique components, the spectral densities exhibited seasonal variability. Comparing with the reference line with a $-5/3$ slope, we can recognize that the spectral amplitude tended to be larger in winter–spring and smaller in summer at the three altitude ranges.

In Figs. 4.5–4.7, we show the mesospheric frequency spectra of vertical and oblique wind velocities observed with the MU radar. The observations were conducted about four successive days a month from December 1985 to December 1988 using five antenna beams in vertical, northward, eastward, southward and westward directions at a zenith angle of 10°.

Because the duration of the mesospheric observation was around 8 hr in daylight hours, the obtained frequency range was only in 1.4×10^{-4}–3.3×10^{-3} Hz (5 min–2 hr in period), the lowest frequency of which was about 10 times higher than that in the troposphere and lower stratosphere.

We can recognize that the frequency spectra of vertical wind velocity was fairly variable, which at frequencies higher than 1×10^{-3} Hz agreed well with the oblique components. We can find that the slopes of the vertical component tended to be flat or positive in the lower frequency range. There exists steep fall off of the spectra with a slope smaller than $-5/3$ in the frequency range

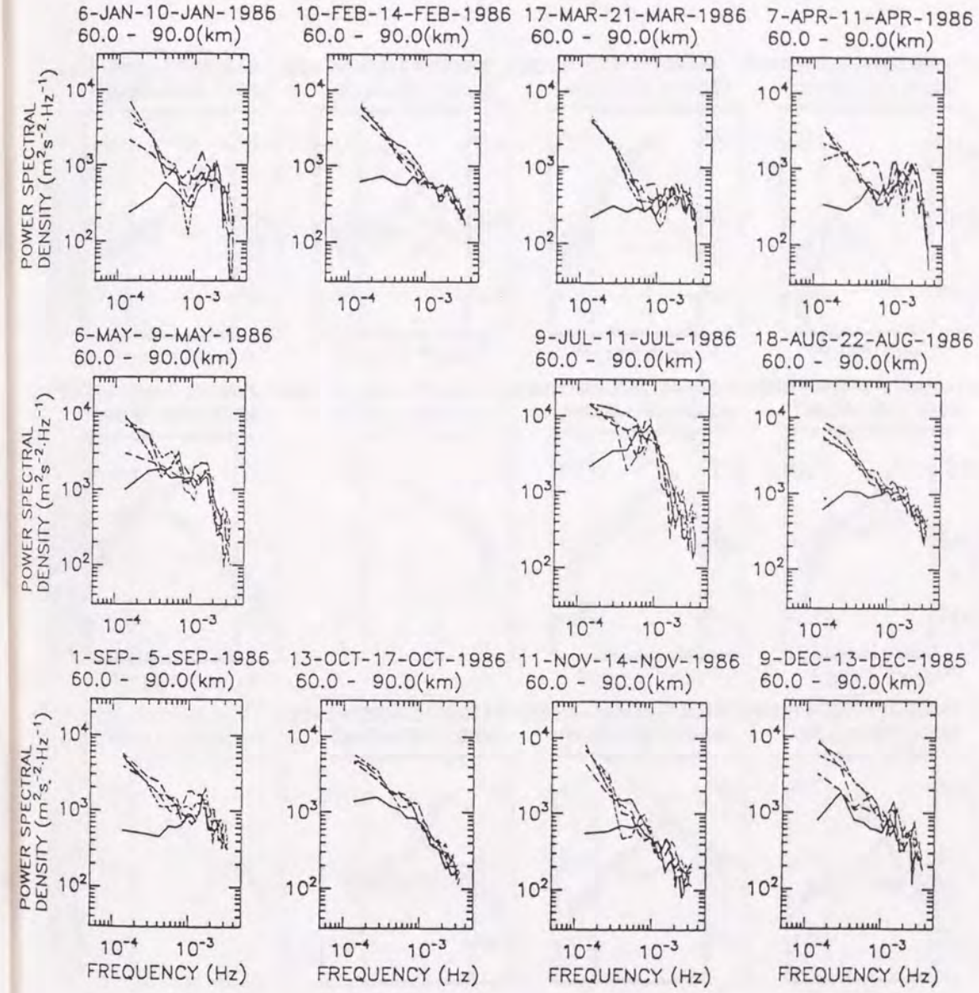

Figure 4.5: Monthly determined frequency spectra of vertical (thick solid) wind velocity and northward (thick short dashed), eastward (thick long dashed), southward (thin short dashed) and westward (thin long dashed) oblique wind velocity in the mesosphere observed with the MU radar from December 1985 to November 1986.

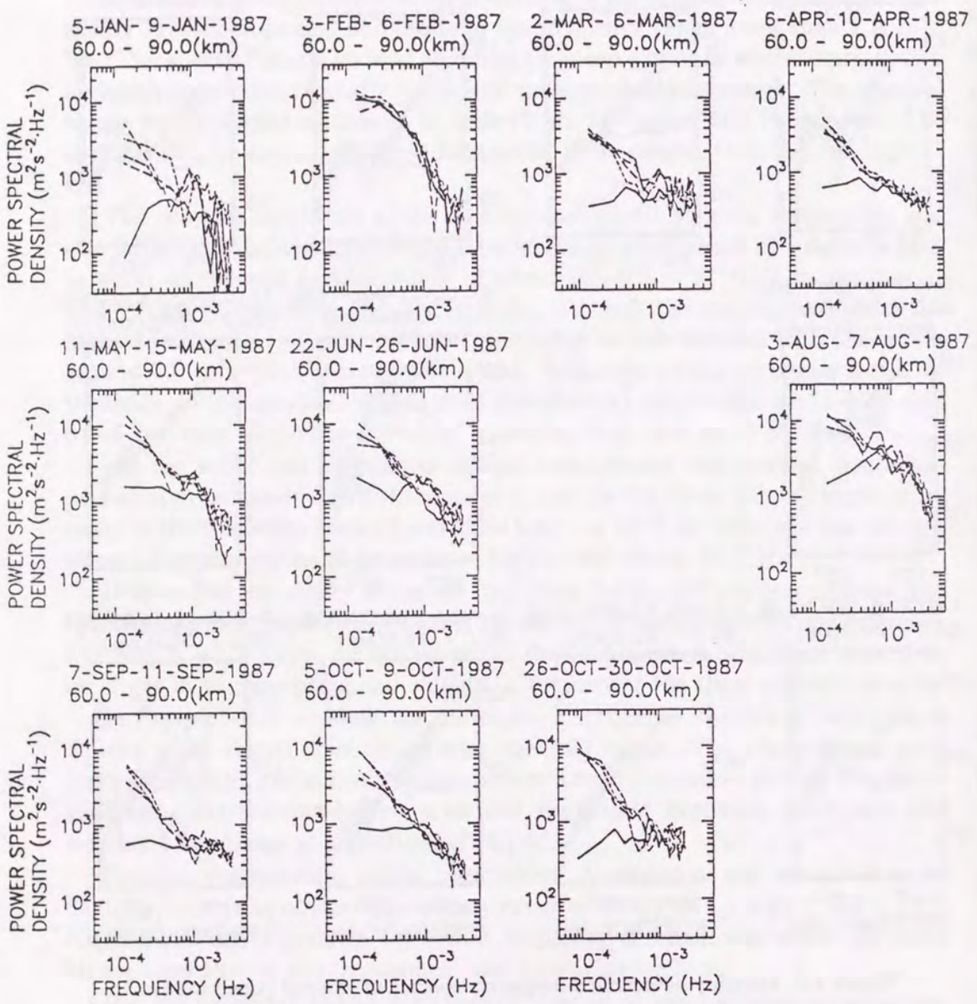

Figure 4.6: The same as Fig. 4.5 except for data in 1987.

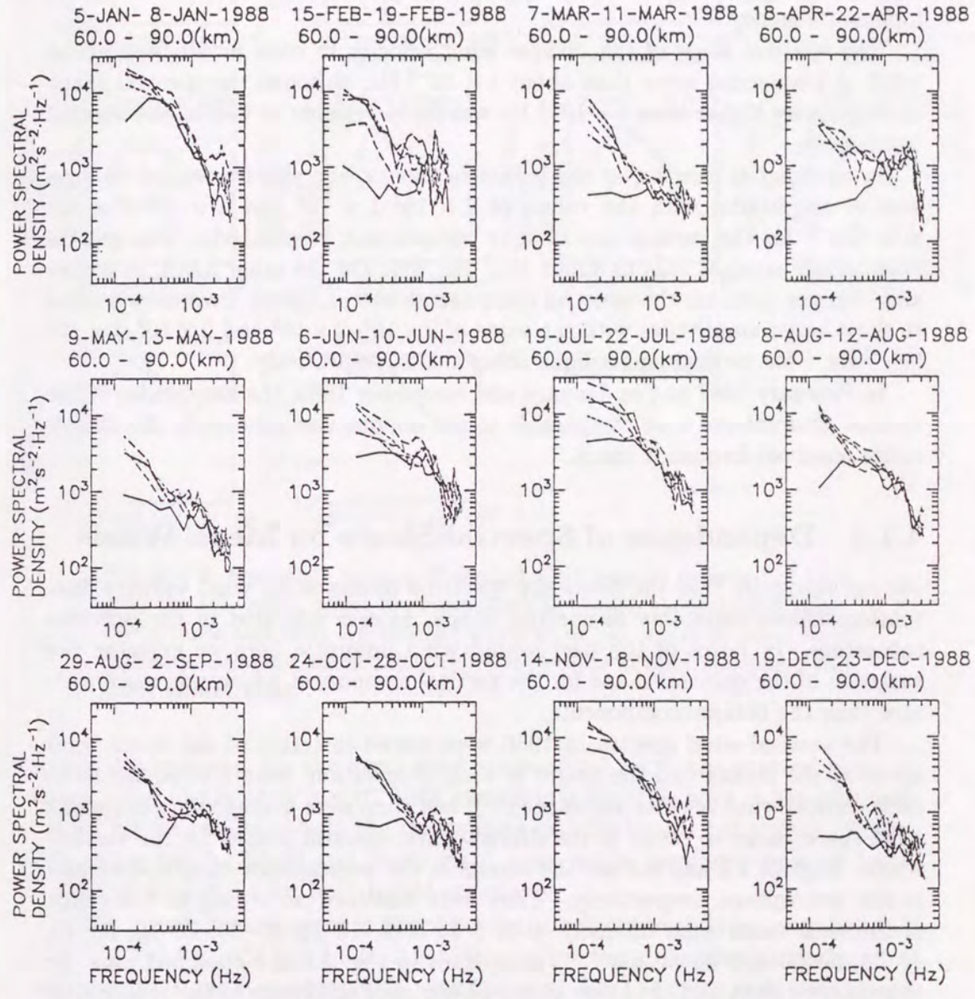

Figure 4.7: The same as Fig. 4.5 except for data in 1988.

higher than about 2×10^{-3}–3×10^{-3} Hz (~5–8 min) in January, March–May 1986, April 1988. These cutoff frequencies likely corresponded to the Brunt-Väisälä frequency in the mesosphere during these observation periods. Except for these months, the vertical spectra showed gradual negative slopes up to the observed highest frequency.

The spectral slope of the oblique wind velocity in each month was about $-5/3$ at frequencies lower than about 1×10^{-3} Hz, although the spectral shape at frequencies higher than 1×10^{-3} Hz was fairly variable as well as the vertical component.

In equinoctial months, at the lowest frequency, the spectra tended to have smaller amplitudes with the values of 2×10^2–1×10^3 and 1×10^3–7×10^3 $m^2s^{-2}Hz^{-1}$ for the vertical and oblique components, respectively. The spectra show nearly straight falls to about 10^{-3} Hz, too. On the other hand, in winter and summer months, the spectral components at the lowest frequency tended to show larger amplitudes with the value of 2×10^2–2×10^4 and 2×10^2–1×10^4 $m^2s^{-2}Hz^{-1}$ for vertical and oblique components, respectively.

In February 1987 and in January and November 1988, the amplitudes of the vertical components were comparable to the oblique components in the almost entire observed frequency range.

4.1.2 Dependence of Spectral Shape on Mean Winds

We can recognize that the frequency spectrum of mesoscale wind velocity fluctuations shows variability in spectral shape, as demonstrated in the previous subsection. In terms of the background wind intensity, here we examine the variation of the spectral shape for the vertical component which was more variable than the oblique components.

The vertical wind spectra in 1986 were sorted in terms of the mean wind speed at the month and the height of each observation, were normalized as to each vertical wind velocity variance ($\overline{w'^2}$), and then were averaged in each mean wind speed range to result in the characteristic spectral shapes for the vertical winds. Figures 4.8 and 4.9 are the results in the troposphere–stratosphere and in the mesosphere, respectively. They were classified according to the range of the local mean wind intensity; 0–3, 3–7, 7–10, 10–15, 15–20, 20–30, 30–40, 40–50, 50–60 and 60–80 ms^{-1}. The spectra in Fig. 4.8 are classified into the tropospheric data and the lower stratospheric ones according to the tropopause heights determined from the routine radiosonde measurements at Shionomisaki, Japan (33°27'N, 135°46'E).

From Fig. 4.8, we can clearly recognize the tendency that the spectral slope become steep when the mean wind intensity increases in the troposphere and

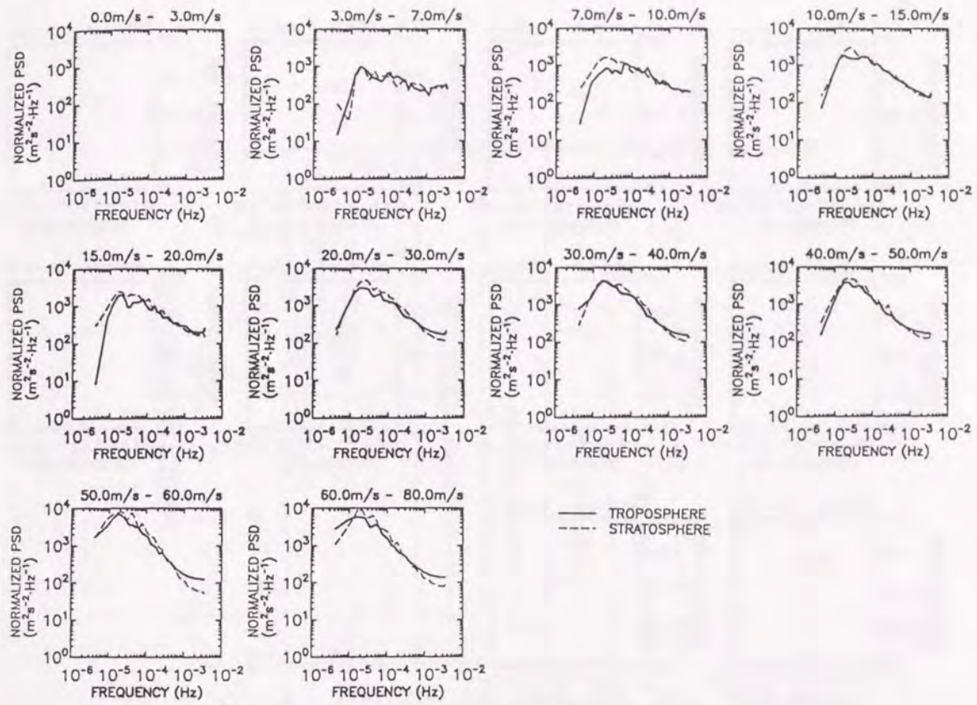

Figure 4.8: Frequency spectra of vertical wind velocity collected in 1986 with the MU radar, which are normalized as to each vertical wind velocity variance and then averaged separatively in ten ranges of mean wind intensity. Solid and dashed lines represent results in the troposphere and lower stratosphere.

lower stratosphere. For the mean wind range of 3–7 ms^{-1}, the spectral slope at frequencies higher than 2×10^{-5} Hz was slightly negative with values of about -0.02 for the results in both the troposphere and the lower stratosphere. While, the slopes for the 50–60 and 60–80 ms^{-1} mean winds became steeper with the values of around -1 for both height regions.

The mesospheric spectra in Fig. 4.9 were calculated in the frequency band of 1.4×10^{-4}–3.3×10^{-3} Hz (5 min–2 hr). We can recognize also similar tendency of the spectral slope steepening with wind intensity. For the mean wind intensity of 3–30 ms^{-1}, the slopes in the frequency range lower than 10^{-3} Hz were nearly flat and slightly negative, while the spectra for the 30–90 ms^{-1} mean winds showed clearly negative slopes at around -1 at frequencies higher than 3×10^{-4} Hz.

The change of the spectral shape according to the mean wind intensity could

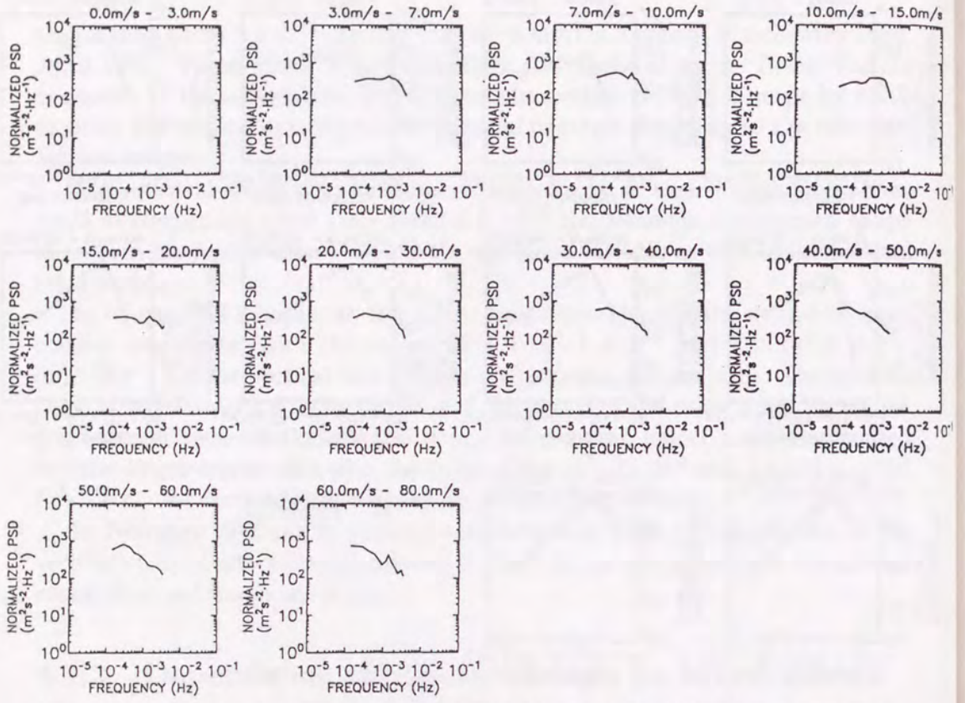

Figure 4.9: The same as Fig. 4.8 except that the mesospheric spectra are plotted.

be understood from the Doppler shifting effect of gravity waves in the mean flow [Scheffler and Liu, 1986; Fritts and VanZandt, 1987]. Fritts and VanZandt [1987] analytically showed the decay of spectral density of vertical wind velocity at higher frequencies induced by the Doppler shifted gravity waves. Consequently the negative slope was found in the frequency spectrum in the none-zero mean wind although it is flat without the mean flow. They also showed that the spectral slope of the horizontal wind velocity does not change very much according to the mean wind intensity, which is consistent with the observed oblique spectra with the slope of about $-5/3$ throughout the year, as shown in Figs. 4.1–4.7.

To clearly illustrate the dependency of the spectral shapes on the mean wind intensity, we estimated the slope of the spectra by using the least-squares fitting of a line to the log-log display of the spectrum (Fig. 4.10). For the observations in the troposphere and lower stratosphere, the fitting was applied to each spectra in the frequency range of about 2.8×10^{-5}–1.7×10^{-3} Hz and then averaged the slope values in each mean wind intensity range to obtain the mean value and its standard deviation.

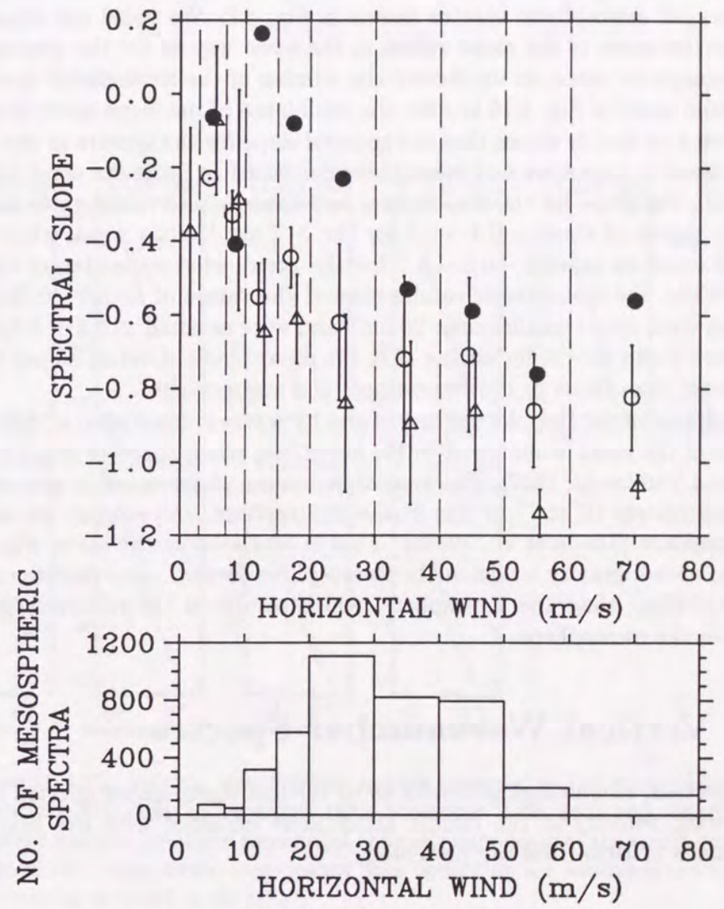

Figure 4.10: (Top panel) Spectral slopes of the frequency spectra vs. the mean wind intensity in the troposphere (open circle), lower stratosphere (triangle) and mesosphere (closed circle). Vertical bars represent standard deviation of the tropospheric and stratospheric slopes, the histogram (bottom panel) indicating the number of the averaged mesospheric spectra.

The estimation of the spectral slope was rather difficult for each of the mesospheric spectra because each spectrum shows large fluctuations due to the large number of missing data. Therefore the fitting was applied to the normalized and averaged mesospheric spectra shown in Fig. 4.9. We could not obtain the standard deviation of the slope values in the same way as for the tropospheric and stratospheric cases, so we showed the number of the mesospheric spectra in the bottom panel of Fig. 4.10 to infer the confidence of the mean spectral slopes.

Figure 4.10 clearly shows that the spectral slope for the spectra in the troposphere, lower stratosphere and mesosphere decreased as the mean wind intensity increased. The slope for the troposphere and stratosphere was slightly negative with the values of about -0.4–-0.2 for the 3–7 ms^{-1} mean wind, while it became as small as around -0.9–-0.7 for the mean wind speed larger than 40 ms^{-1}. While, the mesospheric results showed the values of about -0.05–0.2 at the mean wind speed smaller than 20 $ms^{-1}$and were as small as 0.8–-0.5 for the 30–80 ms^{-1}mean winds, indicating that the mesospheric spectral slopes tended to be larger than those in the troposphere and stratosphere.

The degree of the Doppler shifting of gravity waves is considered to depend on the ratio of the mean wind speed to the horizontal phase speed of gravity waves [Fritts and VanZandt, 1987]. The typical horizontal phase speed is estimated to be approximately 10 ms^{-1} or less in the stratosphere, and roughly 30 ms^{-1} in the mesosphere [Tsuda et al., 1990a]. That is why even in the mean wind with the same speed, gravity waves in the stratosphere seemed more sensitive to the Doppler shifting than the mesosphere, which results in the relatively gradual spectra in the mesosphere.

4.2 Vertical Wavenumber Spectra

In this section, climatological results as to vertical wavenumber spectra of horizontal wind velocity in the middle atmosphere obtained with the MU radar observations in 1986–1988 are presented.

4.2.1 Seasonal Variations of Spectral Shapes

From the long term observation in the mesosphere with the MU radar in December 1985–December 1988, the vertical wavenumber spectra of zonal and meridional oblique wind velocities are presented in Figs. 4.11–4.13. We calculated wavenumber spectra from bihourly mean profiles of oblique wind velocity observed for about four days a month, and then determined a monthly median spectrum from them. The zonal and meridional oblique spectra in the figures

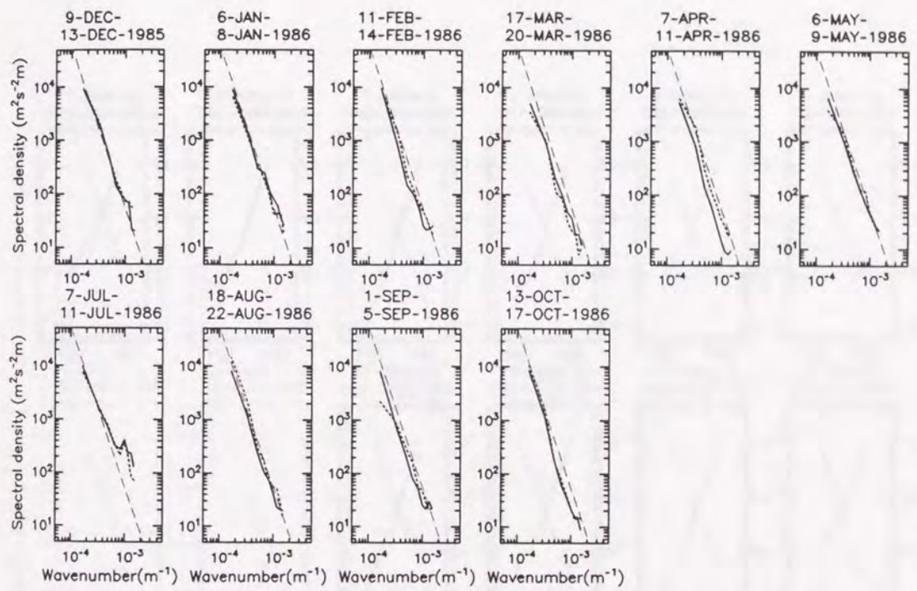

Figure 4.11: Vertical wavenumber spectra observed in the mesosphere with the MU radar in December 1985–November 1986. Solid and dashed lines represent zonal and meridional oblique components at the zenith angle of 10°, respectively, long-dashed lines indicating the saturated model spectrum of Smith et al. [1987].

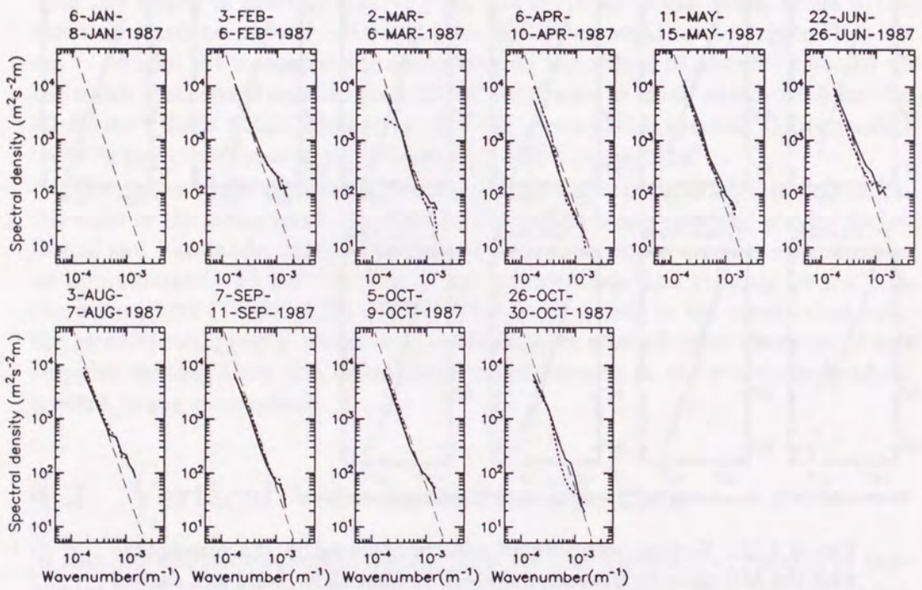

Figure 4.12: The same as Fig. 4.11 except for data in 1987.

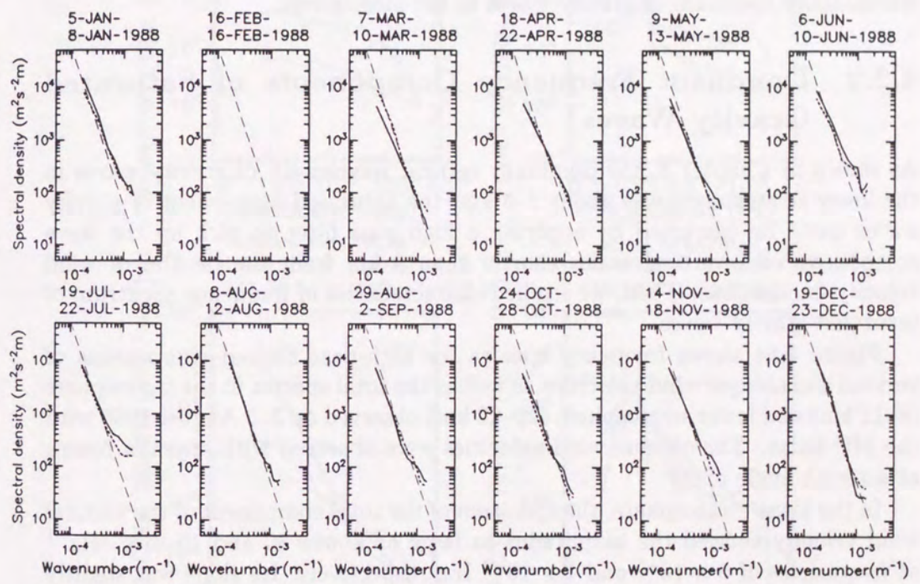

Figure 4.13: The same as Fig. 4.11 except for data in 1988.

were determined as the averages of the eastward and westward, and the northward and southward oblique components, respectively, of the median spectra. The long-dashed lines in the figure represent the saturated spectrum model of Smith et al. [1987] (Equation(1.8)), where the background Brunt-Väisälä frequency $\overline{N}$ was taken from CIRA 1986 model because of no observations of $\overline{N}$ in the mesosphere over the MU radar site.

Figures 4.11–4.13 show that the observed spectra in the vertical wavenumber range of 1.7×10^{-4}–1×10^{-3} cyc/m agreed well with the model spectrum both in amplitude and slope for both the zonal and meridional components throughout the year in 1986–1988, which suggests no significant seasonal variation in vertical wavenumber spectrum of gravity waves in the mesosphere.

4.2.2 Dominant Frequency Components of Saturated Gravity Waves

As shown in Chapter 3, the dominant vertical wavelength of gravity waves in the lower stratosphere was about 2–3 km, the saturated component of gravity waves could be extracted by applying a high pass filter to pick up the wave component with vertical scales shorter than 3 km from the profiles of wind velocity fluctuations. Then, we studied characteristics of frequency spectrum of saturated gravity waves.

Figure 4.14 shows frequency spectra for high-pass filtered components of vertical and oblique wind velocities as well as the total spectra in the troposphere (8–11 km) and lower stratosphere (20–22 km) observed on 3–8 August 1988 with the MU radar. The oblique wind velocities were observed with antenna beams at a zenith angle of 20°.

In the lower stratosphere, the spectrum of the total component of the vertical wind velocity showed the amplitudes as large as about 30 and 15 $m^2s^{-2}Hz^{-1}$ at frequencies of 5×10^{-5} and 1×10^{-3} Hz, respectively. Its slope was slightly negative with the value of about -0.16 in the frequency range of 4×10^{-5}–2×10^{-3} Hz and a small peak with the amplitude of 70 $m^2s^{-2}Hz^{-1}$ at the frequency of around 2×10^{-5} Hz.

The filtered component with vertical scales shorter than 3 km exhibited smaller amplitudes of 10 and 3 $m^2s^{-2}Hz^{-1}$ at 5×10^{-5} and 1×10^{-3} Hz, respectively, which were 1/10–1/5 of the total component. The spectral slope at frequencies of 4×10^{-5}–2×10^{-3} Hz was more negative with the value of about -0.3. While, there still existed a clear spectral peak with the value of 50 $m^2s^{-2}Hz^{-1}$ at 2×10^{-5} Hz, which showed the comparable value to that of the total component.

As a result, we can recognize that the filtered component was dominant

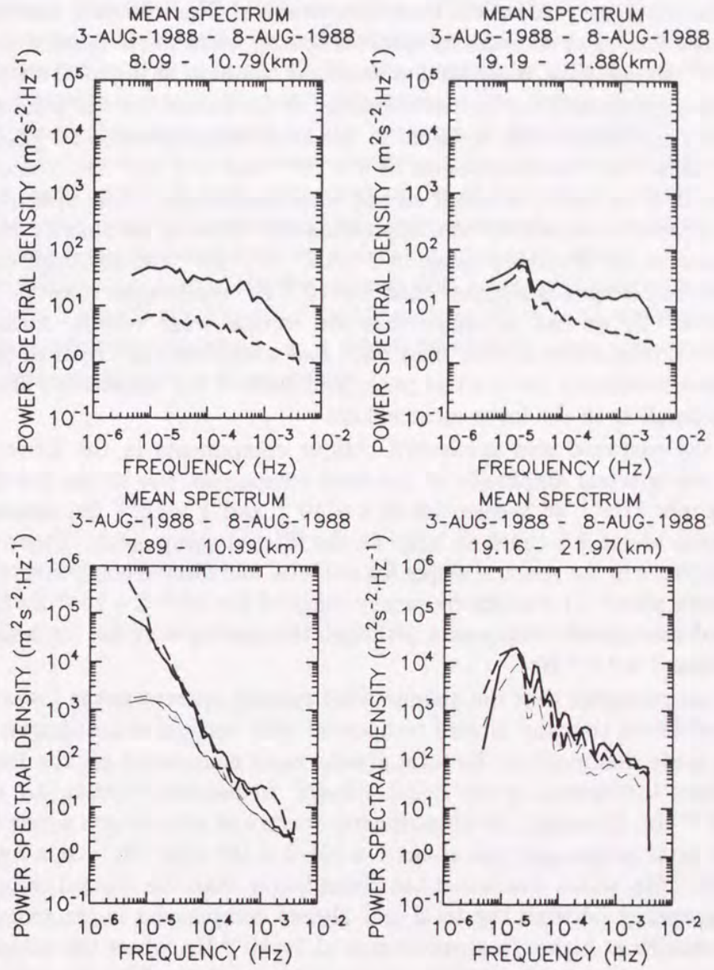

Figure 4.14: Frequency spectra of wind velocities high-pass filtered with a cutoff vertical wavelength of 3 km (thin lines) and the total component (thick) in the height ranges of 8–11 km (left two) and 20–22 km (right two) observed on 3–8 August 1988 with the MU radar, the vertical (top two panels) and oblique (bottom two panels) components being represented. The oblique eastward (dashed) and northward (solid) components in the bottom panels were observed with the off-zenith beam at 20°.

in the total component at the frequency of about 2×10^{-5} Hz, so the gravity wave component with vertical scales shorter than 3 km seemed to be saturated around the spectral peak in the lower stratosphere. The saturated gravity wave component tended to decrease its spectral density when the frequency increased in 4×10^{-5}–2×10^{-3} Hz, while the flat spectrum was seen in the total component.

In the troposphere, the spectral densities of the filtered vertical wind velocity showed no significant peak as found in the lower stratosphere, and were about 6 and 2 $m^2s^{-2}Hz^{-1}$ at frequencies of 5×10^{-5} and 1×10^{-3} Hz, respectively, which were 3–10 times as small as the total component. The spectral slope for the filtered components was approximately identical to that of the total component in the frequency range of 2×10^{-5}–8×10^{-4} Hz, although the total component at frequencies higher than 8×10^{-4} Hz was steeper than the filtered component. So we can recognize that the vertical wind velocity fluctuations with the vertical scales shorter than 3 km had a spectrum as broad as the total component indicating no spectral peak, and showed the amplitudes about 2/3 times as small as in the lower stratosphere.

For the eastward and northward oblique components in the lower stratosphere, the spectral amplitude of the total component was about 2×10^4 and 100–200 $m^2s^{-2}Hz^{-1}$ at frequencies of 2×10^{-5} and 1×10^{-3} Hz, respectively, which were about 1.5 times as large as the filtered component. There existed little difference in the spectral slopes for the total and filtered components, whose values were about -1.5 in the frequency range of 2×10^{-5}–2×10^{-4} Hz for both zonal and meridional components, although the spectra were flat for frequencies higher than 1×10^{-4} Hz.

We can recognize that the oblique wind velocity spectra in the lower stratosphere exhibited that the filtered component with vertical scales shorter than 3 km was fairly dominant in the total gravity wave component for the frequency region from the inertial to the Brunt-Väisälä frequencies, that is, 1.7×10^{-5}–3.3×10^{-3} Hz. However, the tropospheric spectra of the oblique winds showed that the total component was about 1×10^4–2×10^4 $m^2s^{-2}Hz^{-1}$ at a frequency of 2×10^{-5} Hz, which was about ten times larger than the filtered component. The discrepancy between the total and filtered components in the troposphere became smaller at higher frequencies around 5×10^{-4} Hz, where the values of the total component were 30 $m^2s^{-2}Hz^{-1}$ twice as large as the filtered components.

The spectral slopes in the frequency range of 2×10^{-5}–5×10^{-4} Hz were about -2 and -1.4 for the total and filtered components, respectively, the latter being the similar value to that in the lower stratosphere.

Although the spectral amplitude for the total component of the oblique wind velocity in the troposphere was approximately equal to that in the lower stratosphere at the frequency of 2×10^{-5} Hz, the amplitude for the filtered oblique

wind velocity with vertical scales shorter than 3 km in the lower stratosphere was about 5 times larger than that in the troposphere. Also for the filtered oblique wind velocity at the frequency of 5×10^{-4} Hz, the spectral amplitude in the lower stratosphere was about 3–6 times larger than that in the troposphere.

As reported by Tsuda et al. [1991], the amplitudes of horizontal wind velocities of gravity waves in the lower stratosphere were larger than in the troposphere, since they were scaled by the background Brunt-Väisälä frequency squared $\overline{N^2}$ if the gravity waves were saturated. So, if saturated gravity waves were dominant in the filtered component of the oblique wind velocity fluctuations, the larger spectral densities in the lower stratosphere than in the troposphere could be understood from the saturation of gravity waves.

The typical $\overline{N^2}$ values in the troposphere and lower stratosphere are considered to be $(10 \text{ min})^{-2}$ and $(5 \text{ min})^{-2}$, so the ratio of $\overline{N^2}$ in the lower stratosphere to $\overline{N^2}$ in the troposphere results in 4, which reasonably agree with the ratio of the spectral amplitudes in those regions.

Chapter 5

Seasonal Variation of Energy and Momentum Flux of Gravity Waves

Among various observations for clarifying excitation, propagation and saturation processes of gravity waves, the measurement of the upward flux of the horizontal momentum with a ground-based radar is one of the most important techniques [Vincent and Reid, 1983]. In this chapter, we present seasonal variations of wind velocity variance, wave-induced momentum flux, and the mean flow acceleration in the mesosphere and lower atmosphere derived from MU radar data.

5.1 MU Radar Observations in the Mesosphere

By integrating spectral densities shown in Figs. 4.5–4.7 in specific wave period ranges, we obtained the variance of the vertical and radial wind velocities in the four oblique directions [Tsuda et al., 1990b, 1992b]. According to the method developed by Vincent and Reid [1983], zonal and meridional components of the vertical flux of horizontal momentum, $\overline{u'w'}$ and $\overline{v'w'}$, respectively, are determined from the difference between the northward and southward and the eastward and westward variances.

5.1.1 Wind Velocity Variance

Figures 5.1–5.3 show the monthly variances for the vertical, meridional and zonal components, respectively, in period ranges of 5 min – 2 hr, 30 min – 2 hr and 5 – 30 min, where the horizontal axis indicates the center of each observation period. The variance for periods from 5 min to 2 hr shows a fairly regular and

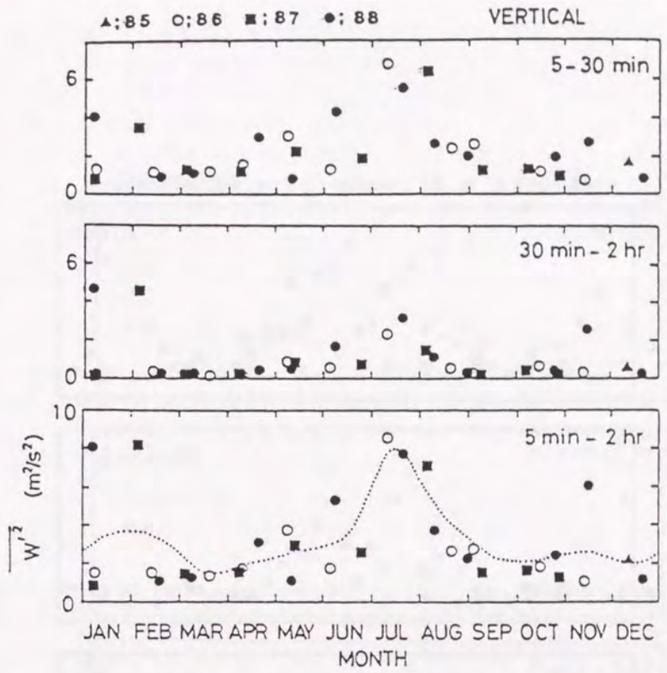

Figure 5.1: Variance of vertical wind velocity for periods from 5–30 min (top), 30 min – 2 hr (middle) and 5 min – 2 hr (bottom) observed with the MU radar for about four days every month from December 1985 to December 1988. Horizontal axis shows the center of the observation period.

persistent peak in summer for three successive years with amplitudes up to 8 m^2s^{-2} and about 10–14 m^2s^{-2} for the vertical and radial components, respectively. Large values of the variance were also detected in winter in November 1988, January 1988 and February 1987, although the peaks were less systematic than in summer, suggesting a large day-to-day variation of gravity wave activity in the winter mesosphere. In March–April and September–October the variance was generally as small as 2 m^2s^{-2} and about 2–4 m^2s^{-2} for vertical and radial components, respectively. On the average there is a semi-annual variation of the variance with maxima in summer and winter, and minima in equinoctial periods. General characteristics of the seasonal variations are similar for all three wind components. Furthermore, amplitudes of the variance are almost the same for the zonal and meridional winds throughout the year.

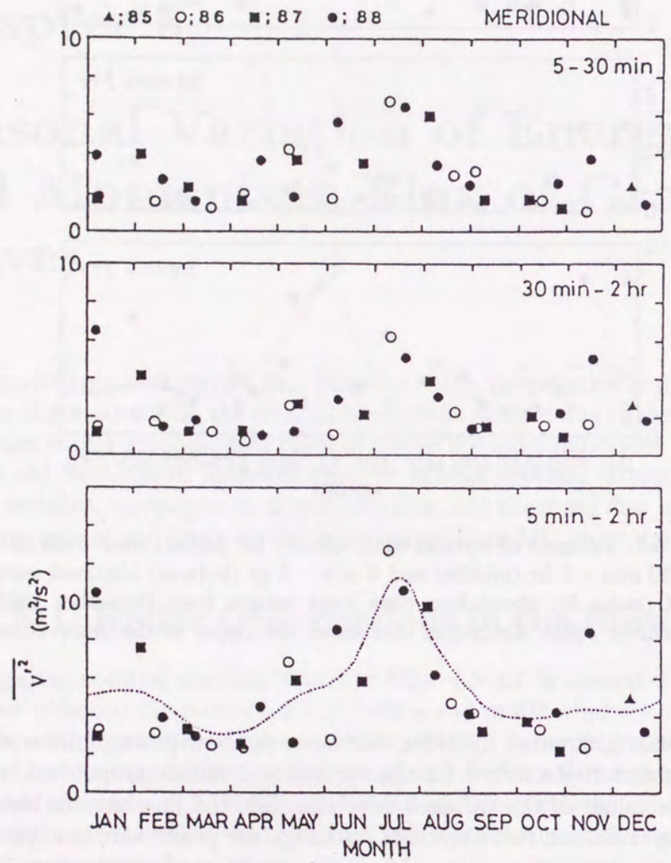

Figure 5.2: The same as Fig. 5.1 except for the meridional wind component collected at 10° off the zenith.

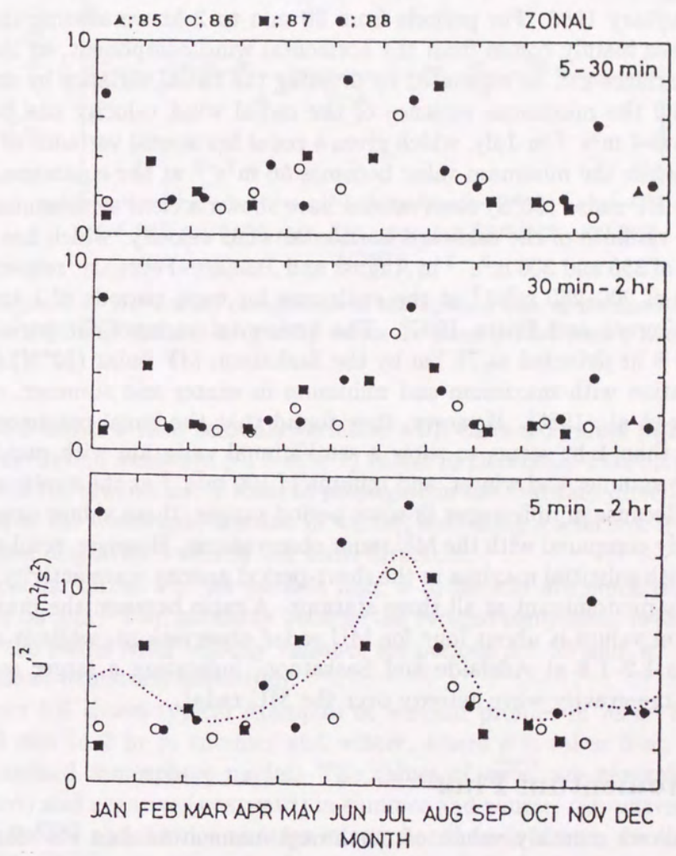

Figure 5.3: The same as Fig. 5.1 except for the zonal wind component collected at 10° off the zenith.

For periods from 5 to 30 min, the radial wind velocity variance is mainly determined by the vertical wind component. On the other hand, the contribution of the horizontal wind component to the radial variance becomes significant for periods from 30 min to 2 hr. However, the contribution of the vertical component is significant in winter when the enhancement is evident as in February 1987 and January 1988. For periods from 30 min to 2 hr we assume that the radial variance mainly comes from the horizontal wind component, so that the horizontal variance can be estimated by dividing the radial variance by $\sin^2 10°$. From Fig. 5.3 the maximum variance of the radial wind velocity can be estimated to be 6–7 m^2s^{-2} in July, which gives a zonal horizontal variance of about 200 m^2s^{-2}, while the minimum value becomes 50 m^2s^{-2} at the equinoxes.

Adelaide HF radar (35°S) observations have shown a clear semi-annual variation of the variance of the eastward horizontal wind velocity. which has maximum values of 350 and 300 m^2s^{-2} in August and January–February, respectively, and minima of 200–250 m^2s^{-2} at the equinoxes for wave periods of 1 to 24 hr at 86 km [Vincent and Fritts, 1987]. The horizontal variance for periods between 1 and 8 hr detected at 75 km by the Saskatoon MF radar (52°N) has an annual variation with maximum and minimum in winter and summer, respectively [Meek et al., 1985]. However, they found that the zonal component for periods less than 1 hr seems to show a semi-annual variation with maxima of 140 m^2s^{-2} in summer and winter, and minima of 100 m^2s^{-2} at the equinoxes, respectively. Because of differences in wave period ranges, these values cannot be quantitatively compared with the MU radar observations. However, semi-annual variations with solstitial maxima in the short-period gravity wave activity seems to be equally predominant at all three stations. A ratio between the maximum and minimum values is about four for MU radar observations, while it can be estimated as 1.2–1.8 at Adelaide and Saskatoon, indicating a larger seasonal variation of the gravity wave activity over the MU radar.

5.1.2 Momentum Flux

Figure 5.4 shows monthly values of northward momentum flux $\overline{v'w'}$ for wave periods from 5 min to 2 hr. Except for a large northward departure in July 1988 and several negative values in some winter and summer months, $\overline{v'w'}$ rarely exceeds ± 1 m^2s^{-2}. Although the variance shows a semi-annual variation as plotted in Fig. 5.2, there is no significant seasonal variation in $\overline{v'w'}$, which suggests that meridional propagation of gravity waves is not selective in direction. In other words, the resultant meridional momentum flux must be balanced between the northward and southward propagating components, giving very small $\overline{v'w'}$ throughout the year. On the other hand, the zonal component $\overline{u'w'}$ plotted

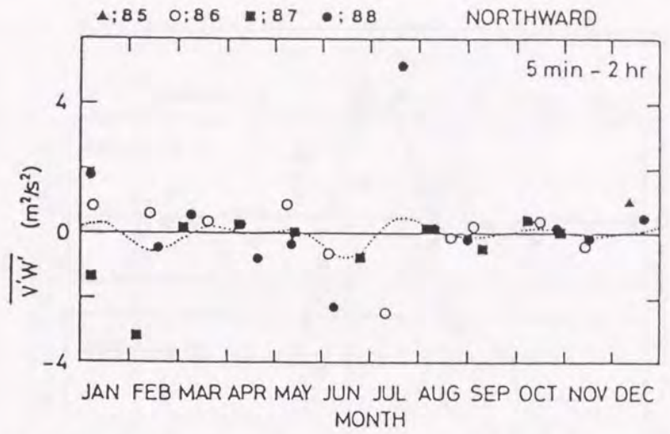

Figure 5.4: Northward component of the upward flux of horizontal momentum $\overline{v'w'}$ induced by gravity waves for wave period from 5 min to 2 hr.

in Fig. 5.5 shows a clear seasonal variation with eastward values (+2 m^2s^{-2}) in July–August and westward (–1.5 m^2s^{-2}) values in December–February. A larger fraction of the gravity waves seem to propagate in the eastward direction in summer and in the westward direction in winter, indicating a selective transmission or filtering of gravity waves in the zonal direction.

The zonal fluxes $\overline{u'w'}$ for periods from 5 to 30 min are much smaller than those for 30 min – 2 hr, probably because the vertical component is the principal part of the radial wind velocity variance for periods 5 – 30 min, so that it has only a small azimuthal anisotropy.

Figure 5.6 shows typical examples of vertical profiles of $\rho\overline{u'w'}$ for periods from 30 min to 2 hr in summer and winter, where ρ is taken from the CIRA 1972 standard atmosphere model. The values of $\rho\overline{u'w'}$ are generally positive (eastward) and negative (westward) in summer and winter, respectively, and the amplitudes are about twice as large in summer than in winter. In August 1986 and 1988 $\rho\overline{u'w'}$ decreasing trend from about 1.5×10^{-4} to 0.5×10^{-4} $kg{\cdot}m^{-1}s^2$ with altitude from 68 to 78 km, although there were significant fluctuations over vertical scales of several kilometers. In July 1988, $\rho\overline{u'w'}$, as well as the vertical gradient, were larger than those in August. In February $\rho\overline{u'w'}$ varied from -1.0×10^{-4} $kg{\cdot}m^{-1}s^2$ at 70 km to positive values above 77 km, while in December 1985 the $\rho\overline{u'w'}$ were larger than in February.

The mean flow acceleration or drag force per unit mass $-1/\rho{\cdot}d(\rho\overline{u'w'})/dz$ can be estimated from the vertical gradient of lines fitted to the $\rho\overline{u'w'}$ profiles

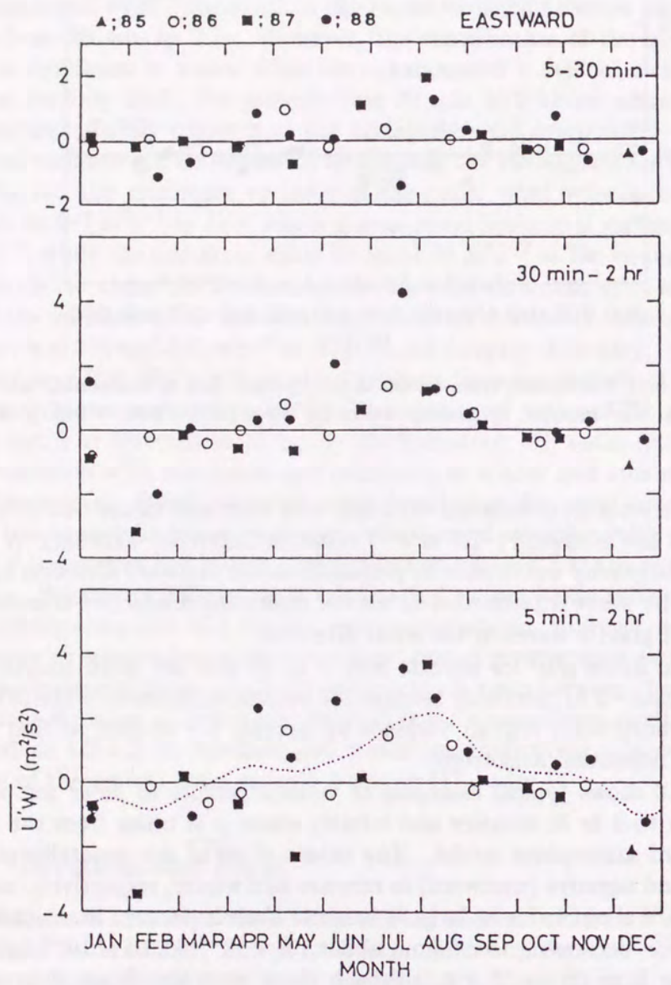

Figure 5.5: The same as Fig. 5.4 except for the eastward component $\overline{u'w'}$, and for wave periods from 5 to 30 min (top), from 30 min to 2 hr (middle) and 5 min to 2 hr (bottom).

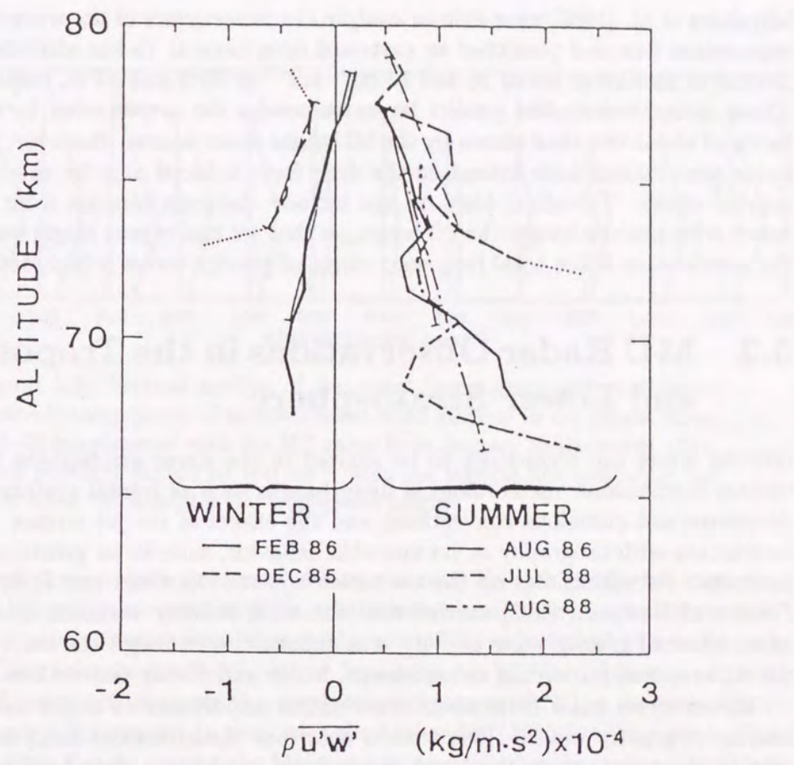

Figure 5.6: Typical profiles of eastward momentum flux $\rho\overline{u'w'}$ determined in winter (left side) and summer (right side). Thin lines show the best-fit for vertical gradient of $\rho\overline{u'w'}$.

plotted in Fig. 5.6. The results for the summer months were 7.2, 12.8 and 9.4 $ms^{-1}km^{-1}$ in the eastward direction at 70–77 km in August 1986, at 73–79 km in July 1988 and at 66–75 km in August 1988, respectively. For the winter profiles, the drag force was 7.6 and 11.0 $ms^{-1}km^{-1}$ in the westward direction at 70 – 78 km in February 1986 and at 73 – 77 km in December 1985, respectively.

Now, we compare the observed mean flow acceleration with the theoretical predictions. Holton and Wehrbein [1980] adopted Rayleigh friction damping of 0.35 day^{-1} at 75 km in their GCM simulation, which produces a drag force of 14 $ms^{-1}km^{-1}$ when the mean zonal wind of about 40 ms^{-1} at 35°N in summer is substituted into the Rayleigh friction damping force term. By extracting gravity wave components generated in the GFDL SKYHI general circulation model,

Miyahara et al. [1986] were able to analyze the convergence of the wave-induced momentum flux and predicted an eastward drag force at 75 km altitude at the December solstice of about 26 and 13 $ms^{-1}km^{-1}$ at 35°S and 35°N, respectively. These theoretical studies predict larger values for the acceleration by up to a factor of about two than shown by the MU radar observations. However, the MU radar observations have estimated the drag force induced only by short-period gravity waves. Therefore, they do not include the contributions from gravity waves with periods longer than 2 hours, so that we can expect larger values for the acceleration if the total frequency range of gravity waves is included.

5.2 MU Radar Observations in the Troposphere and Lower Stratosphere

Gravity waves are considered to be excited in the lower atmosphere through various mechanisms; meteorological disturbances such as frontal systems, thunderstorms and cumulous convections, and the effects of the jet stream, i.e., its interaction with orography or its unstable behavior, such as on geostrophic adjustment. Recent studies on the excitation sources [Nastrom and Fritts, 1992; Fritts and Nastrom, 1992] showed that the wind velocity variance, considered as an index of gravity wave activity, was enhanced over rough terrain, and also during events of jet stream enhancement, fronts and strong convections.

However, we know little about the relative importance of major excitation sources of gravity waves. This section describes climatological analysis of the gravity wave activity in the lower atmosphere involving a data-base collected with the MU radar, which is compared with the seasonal variation of the background mean wind. We further aim to clarify the dominant processes in the excitation of gravity waves, focusing on the difference between long (2–21 hr) and short (5 min – 2 hr) period components in the troposphere and lower stratosphere [Murayama et al., 1992c].

We integrated the monthly mean spectra which were shown in Figs. 4.1–4.4 in specific frequency ranges, in order to obtain the radial wind velocity variance, and finally derived the variance of vertical, zonal and meridional wind velocity components.

5.2.1 Jet Stream Activity

The eastward wind associated with the jet stream is normally dominant in the troposphere and lower stratosphere at mid-latitudes, and its intensity is generally larger in winter than in summer, which is due to a seasonal change in the global

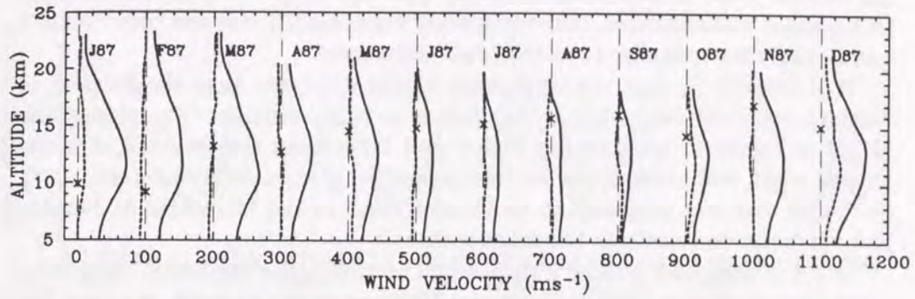

Figure 5.7: Vertical profiles of the zonal (solid lines) and meridional (dashed) components of monthly mean wind velocity in the height range of 5–25 km observed with the MU radar from January to December 1987. Each profile is shifted by 100 ms^{-1} with the vertical line indicating the zero value; '×' indicates the tropopause height.

meridional temperature gradient. Kitamura and Hirota [1989], for instance, reported the seasonal variation of the jet stream structure over Japan determined from rawinsonde observations, that is, the core of the subtropical jet was located at 11–12 km over the southern part of Japan (about 33°N) in January, while it exhibited lower activity over the northern part (about 45°N) in August. Thus, the jet core is considered to pass over the MU radar (35°N) twice a year. The distance from the jet core to the MU radar is normally longer (around 1000 km or more) in summer and shorter in winter, which further enhances the seasonal variation of the mean wind intensity over the MU radar.

Figure 5.7 shows the monthly profiles of zonal and meridional wind velocities observed with the MU radar in the height range of 5–25 km in 1987. The tropopause height, also plotted in Fig. 5.7, was determined from routine radiosonde observations at Shionomisaki (33°N, 136°E), which is located about 150 km south from the MU radar site.

The zonal winds were generally eastward, showing peaks at 11–13 km with maximum values of about 50–70 ms^{-1} in late autumn–winter–spring (October through May), while the maximum values were 15–30 ms^{-1} in summer to autumn (June–September). When the peaks were clearly detected in a height region of 10–15 km in winter–spring, the zonal wind amplitudes linearly decreased above the jet peaks. Zonal wind velocity at 5 km, i.e., the lowest observed height, was in the range of 20–40 ms^{-1} in autumn–winter–spring, and less than 20 ms^{-1} in summer, while at 20 km it was less than about 20 ms^{-1} throughout the year, with

particularly smaller values in summer. Therefore, it can also be recognized that the vertical shear of horizontal wind was generally large when the jet intensity at 10–15 km was enhanced. The meridional wind velocity was less than 30 ms^{-1} and it was always smaller than the zonal component.

It is noteworthy that the tropopause height was lower than the jet peak in January and February, while it was higher in other months. The tropopause height is known to be generally higher and lower than the jet peak at a site located south and north of the jet core, respectively [e.g., Andrews et al., 1987], so the jet core was supposed to be located south of the MU radar in January and February, and north in the other months.

In Fig. 5.8 we have plotted a time-height section of the horizontal mean wind speed from December 1985 to December 1989, where the jet peak, at about 10–13 km, is indicated as a dot. The maximum wind speed exceeded 60–70 ms^{-1} in winter and spring, while in summer it was persistently small each year. As a result, the background wind speed, or the jet stream intensity, over the MU radar demonstrated fairly clear annual variation, with a maximum and a minimum in winter and summer, respectively.

The detailed structure in the contour plots in Fig. 5.8 sometimes indicates two separate peaks at around 10 km in winter–spring, that is, in December–February and March–May in 1985/86, 1986/87 and 1988/89, while three peaks were found in winter in 1987/88. When the two peaks appeared in winter, the tropopause height seemed to be lower and higher than the jet peak height for the earlier and later peaks, respectively. So it is suggested that these two peaks are

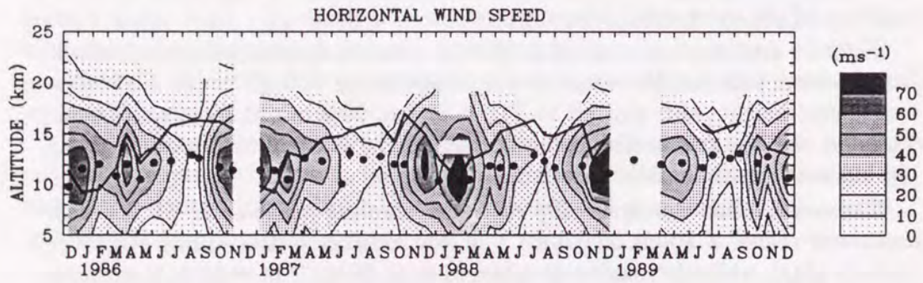

Figure 5.8: Height-time cross section of mean horizontal wind speed observed from December 1985 to December 1989. The horizontal axis indicates the center of the observation period. The heights of the tropopause (thick line) and the maximum wind speed (dots) are shown in the cross section.

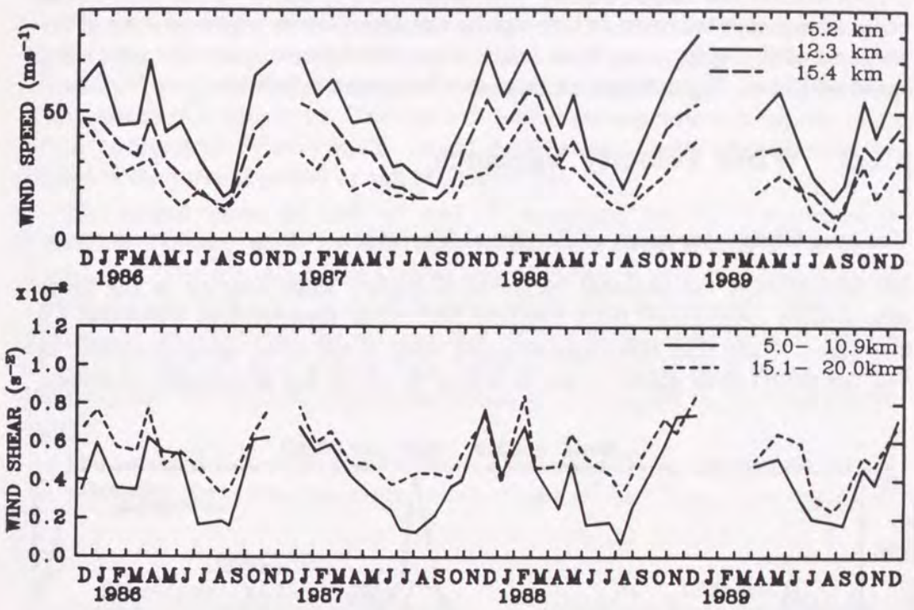

Figure 5.9: (Top panel) The mean wind speed at the heights of 5.2 km (short dashed line), 12.3 km (solid line) and 15.4 km (long dashed line), and (bottom panel) the mean vertical shear of horizontal wind velocity in the height ranges of 5–10.9 (solid line) and 15.1–20 km (dashed line).

associated with passage of the jet core toward the south and north over the MU radar. While, in winter in 1987/88, the tropopause height in February agreed with the jet peak height and was the lowest in that winter, which may suggest that the lowest latitude of the jet core was around the MU radar site. So, the three peaks in the 1987/88 winter may have been caused not only by the change in the latitude of the jet core but also by the jet intensity variation.

The structure of the mean wind profiles can be characterized by the intensity of the horizontal wind (at 5, 12 and 15 km) and the vertical shear of horizontal wind (at 5–11 and 15–20 km), as shown in Fig. 5.9. All of these quantities showed annual variations with maxima in winter, showing quite similar seasonal behavior, although the ranges of the variations were, of course, different from each other.

This implies that the mean wind speed and wind shear in the troposphere

and lower stratosphere are well correlated with the jet stream activity, which is dominant in this height region. The mean wind speed at 12 km showed the most conspicuous variation, which can be considered to be representative of the variation of the background mean wind. So, we hereafter employ the mean wind speed at 12 km, $\overline{U}_{12km}$, as an index of the jet stream intensity.

5.2.2 Wind Velocity Variance

General Characteristics of Seasonal Variation

We here present the seasonal variation of gravity wave activity in the lower stratosphere determined from monthly MU radar observations continued for four years. Note that the effective upper limit of the wind velocity profiles in Fig. 5.8 varied from about 22 km in winter to 15–19 km in summer, therefore,

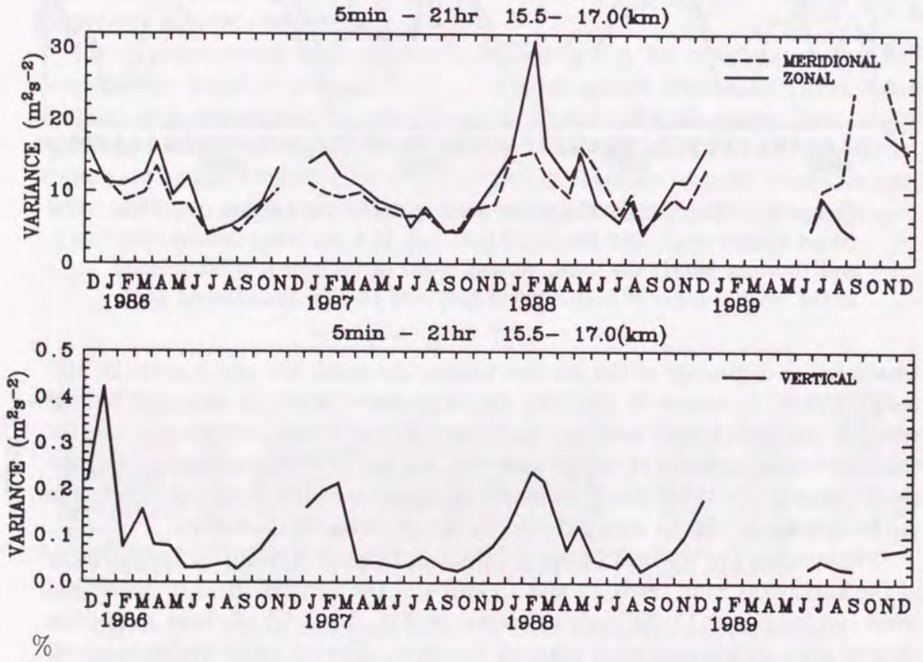

Figure 5.10: (Top) Variance of zonal (solid line) and meridional (dashed) wind velocity fluctuations at 15.5–17 km altitudes for the periods of 5 min–21 hr. The vertical velocity variance is also shown (bottom).

for analysis of gravity waves in the lower stratosphere, we utilized data in the height range of 15.5–17 km.

Figure 5.10 shows monthly determinations of the wind velocity variance at 15.5–17 km for zonal, meridional and vertical wind velocity components ($\overline{u'^2}$, $\overline{v'^2}$ and $\overline{w'^2}$, respectively), which were estimated for the fluctuating components with periods of 5 min–21 hr. The shortest period corresponds to a typical value of the background Brunt-Väisälä period in the stratosphere, while the longest period is the inertial period at the MU radar site.

The largest values of both $\overline{u'^2}$ and $\overline{v'^2}$, exceeding 14 m^2s^{-2}, appeared in December–January, while the minimum values were about 4–5 m^2s^{-2} in July–September. The $\overline{w'^2}$ values also showed annual variation with persistently small values of about 0.02 m^2s^{-2} in June–October, while they were greatly enhanced in winter, the ratio between the maxima and minima being larger than 10. Values of both $\overline{u'^2}$ and $\overline{v'^2}$ were greater than that for $\overline{w'^2}$ roughly by a factor of ten, implying that the horizontal component mainly contributed to the total kinetic energy.

The seasonal variations of $\overline{u'^2}$ at 15.5–17 km and $\overline{U}_{12km}$ are simultaneously plotted in Fig. 5.11. The maximum values of both $\overline{u'^2}$ and $\overline{U}_{12km}$ were collocated

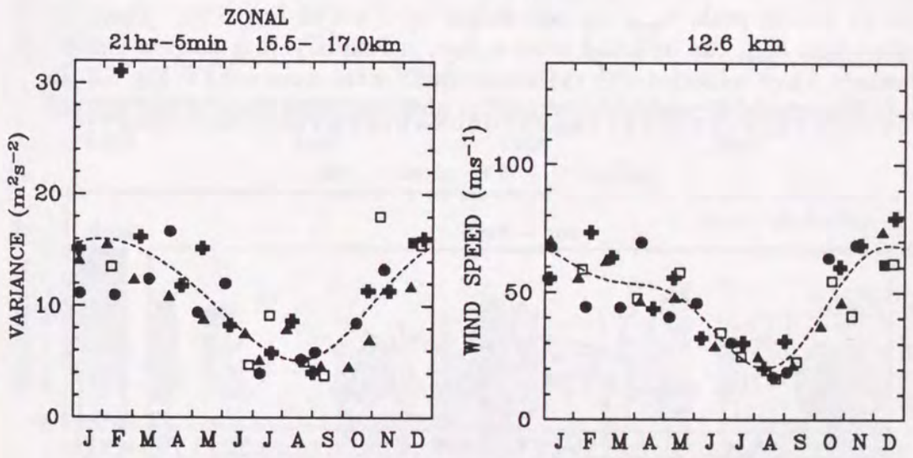

Figure 5.11: (Left) Variance of zonal wind velocity at the heights of 15.5–17 km for the periods of 5 min–21 hr. (Right) Mean horizontal wind speed at 12.6 km. The dashed lines indicate a least-squares fit of a mean, annual and semiannual components. Closed boxes, circles, triangles, crosses and open boxes represent the data in 1985, 1986, 1987, 1988 and 1989, respectively.

in January–December, and the minimum in August. The maxima to minima ratios for both quantities were nearly equal to each other. As a result, their seasonal variations in both amplitude and phase were quite similar to each other, indicating that $\overline{u'^2}$ at 15.5–17 km and $\overline{U}_{12km}$ are very well correlated.

To summarize, the wind velocity variance in the lower stratosphere showed clear annual variation with a maximum in winter and a minimum in summer, which agreed fairly well with the seasonal variation of the mean winds. That is, the excitation and/or filtering process of gravity waves seems to be closely related to the jet stream activity.

Short Period (5 min–2 hr) Component

We now separately analyze two wave period ranges: short (5 min–2 hr) and long (2–21 hr) period gravity waves. In Fig. 5.12, we show a time-height section of the energy density per unit volume for the short period components (5 min–2 hr), E_s ($= \rho(\overline{u'^2} + \overline{v'^2} + \overline{w'^2})$, where ρ is air density taken from the CIRA 1986 model atmosphere).

We can clearly recognize that E_s became large at about 10–15 km in winter–spring, the enhancement appearing at a height approximately corresponding to the jet stream peak, h_{peak} (as represented by a dot in Fig. 5.12). Large E_s values near h_{peak} can be found twice a year, in February–May and November–January, which coincided with the enhancement of the mean wind in Fig. 5.8. In July–September, E_s was normally small at altitudes higher than 10 km, and the

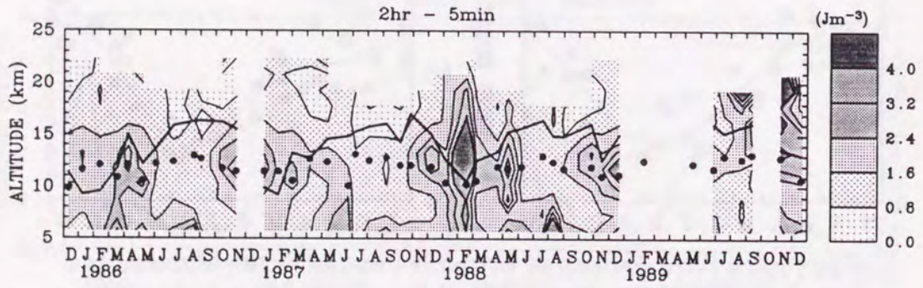

Figure 5.12: Time-height sections of the energy density per unit volume of wind velocity fluctuations for the periods of 5 min–2 hr. The bold line and the dots indicate the heights of the tropopause and the maximum wind speed, respectively.

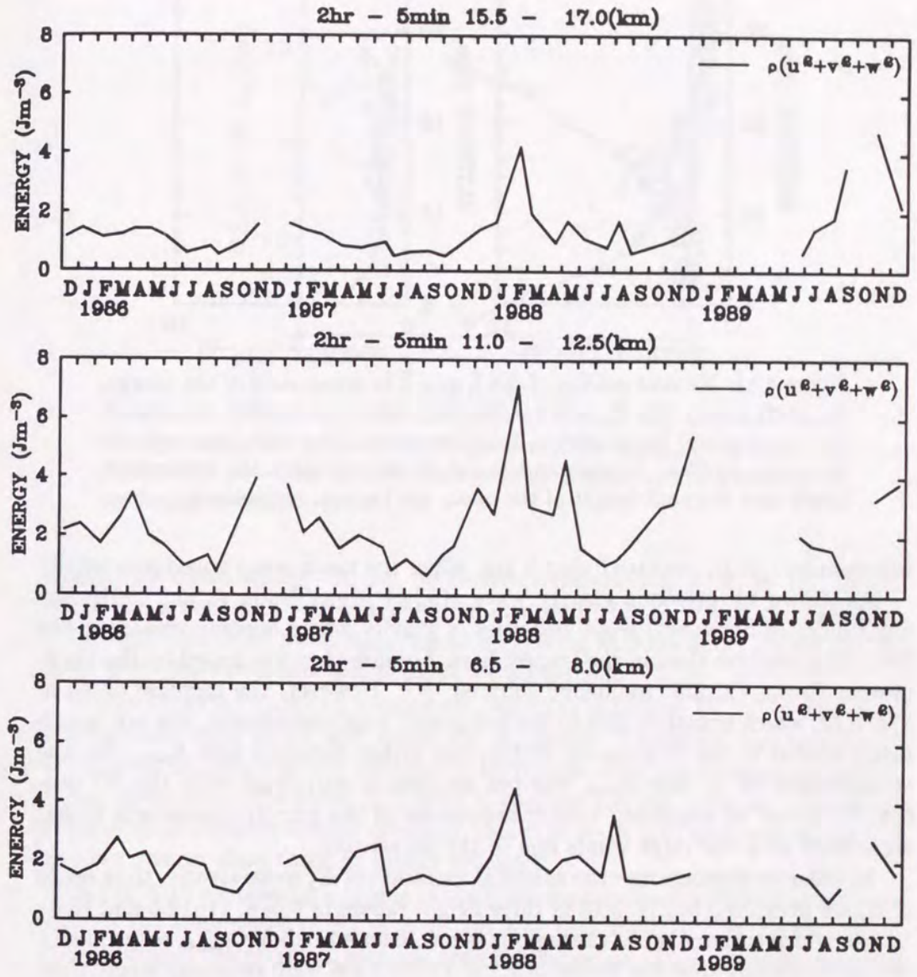

Figure 5.13: The energy density of wind velocity fluctuations for the periods of 5 min–2 hr at the height ranges of 6.5–8, 11–12.5 and 15.5–17 km.

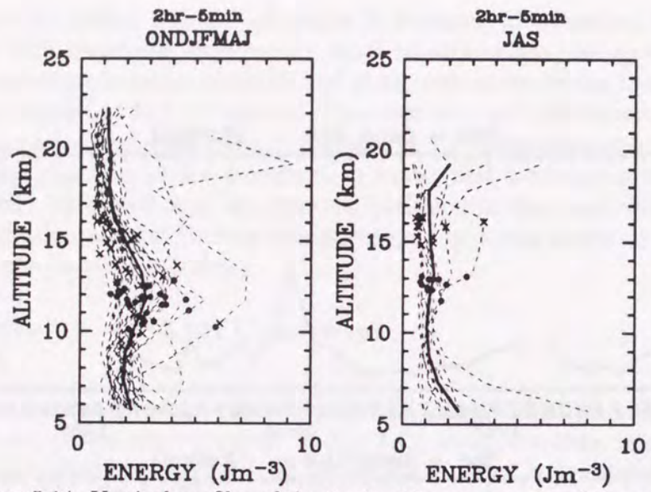

Figure 5.14: Vertical profiles of the 5 min–2 hr component of the energy, E_s. (Left panel) The E_s values in January–June and October–December, and (right panel) the profiles in July–September. The thick lines indicate the mean profiles. Crosses and closed circles represent the tropopause height and the peak height of the mean wind speed, respectively.

enhancement of E_s occurred near 5 km, when the mean wind speed was small.

As shown by previous gravity wave studies [e.g., Tsuda et al., 1991], the amplitudes of horizontal wind velocities of gravity waves become greater in the lower stratosphere than in the troposphere, because they are scaled by the background Brunt-Väisälä frequency squared, $\overline{N^2}$. However, the increase of E_s in Fig. 5.12, which is mainly due to the horizontal wind component, was not necessarily related to the tropopause height, but rather occurred near h_{peak}. So, the enhancement of E_s near h_{peak} was not necessarily correlated with the $\overline{N^2}$ profile, but it can be suggested that enhancement of the gravity energy was rather associated with the large winds due to the jet stream.

In order to demonstrate the seasonal variation of E_s more clearly, time series of E_s are presented in Fig. 5.13 in three height ranges of 6.5–8, 11–12.5 and 15.5–17 km, which correspond to the regions below, near and above h_{peak}, respectively. We can recognize that the values of E_s at 11–12.5 km were generally larger than those at 6.5–8 and 15.5–17 km. At 11–12.5 and 15.5–17 km, E_s showed fairly clear annual variation with larger values in winter and regular minima in summer (July–September).

Profiles of E_s in two periods are shown in Fig. 5.14: from October through June and July to September, which represent the periods of large and small

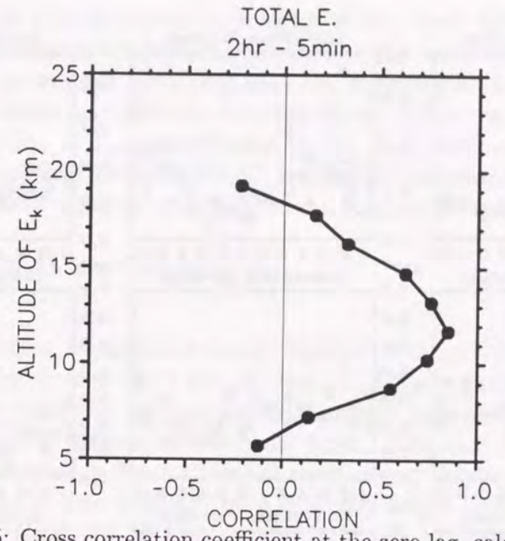

Figure 5.15: Cross correlation coefficient at the zero lag, calculated from the time series of the 12 km wind speed and the energy density for the periods of 5 min–2 hr. The correlation value is presented as a function of the height of the energy.

background mean winds. It can be clearly recognized that E_s in the former period had a peak at 10–15 km, centered at around 12 km, which corresponded to the height of the jet peak, h_{peak}, again suggesting that the short period gravity waves were generated near the peak of the jet stream.

It is noteworthy that the tropopause, which is indicated by '×' in Fig. 5.14, is distributed both above and below the E_s peaks. Therefore, the location of the E_s peak heights was not necessarily correlated with the tropopause height. On the other hand, the other E_s profile in summer did not show any significant enhancement, showing almost constant values at 9–18 km, although E_s at 5–8 km were greater than those at higher altitudes.

In Fig. 5.15 we present a profile of the cross-correlation coefficient at zero lag between the time series of E_s at 5–20 km and that for $\overline{U}_{12km}$ at 12 km. That is, we analyzed the correlation of the seasonal variation of the jet peak intensity and the gravity wave energy in the troposphere and lower stratosphere. The CCF values thus calculated were generally positive except for those at 5–6.5 and 18.5–20 km, and the maximum value of about 0.9 was obtained at 11–12.5 km altitude.

Next, we separately present seasonal variations of the energy for horizontal

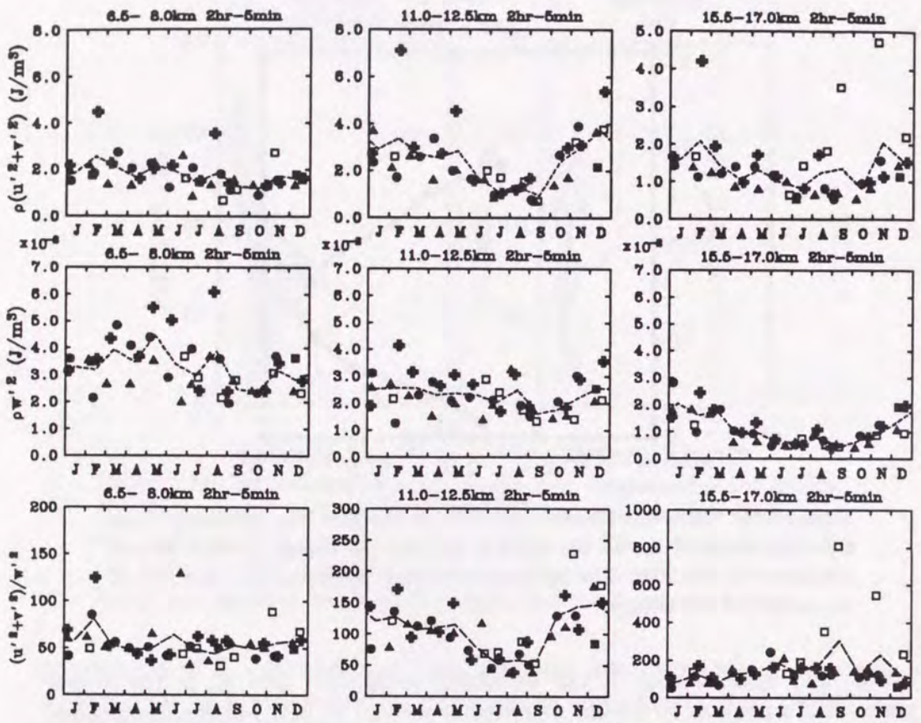

Figure 5.16: The energy density of horizontal motions, E_{sh} (top three panels), and vertical motions, E_{sw} (middle three), and the ratio of E_{sh} to E_{sw} (bottom three), for the periods of 5 min–2 hr. The left, center and right columns present data in the height regions of 6.5–8, 11–12.5 and 15.5–17 km, respectively. The dashed lines represent the monthly averages for the four years, the symbols being the same as in Fig. 5.11.

and vertical motions, E_{sh} and E_{sw}, respectively, together with their ratio. Figure 5.16 shows the monthly means of E_{sh} and E_{sw} and E_{sh}/E_{sw} in the height ranges of 6.5–8, 11–12.5 and 15.5–17 km. Since E_{sh} is dominant in E_s, seasonal variation of E_{sh} becomes similar to that of E_s, showing an annual cycle with winter maxima and summer minima.

Comparing E_{sw} at three different height ranges in Fig. 5.16, it can be recognized that E_{sw} generally decreased with altitude, such that they were 0.02–0.06, 0.01–0.04 and 0.002–0.03 Jm^{-3} at 6.5–8, 11–12.5 and 15.5–17 km, respectively. In January the E_{sw} value at 15.5–17 km was only about 0.6 of the value at 6.5–8

km, while E_{sw} in July decreased by a factor of 0.17 from the 6.5–8 to 15.5–17 km region. It is noteworthy that the decrease of E_{sw} with altitude was smaller in winter than in summer, implying that the characteristics of vertical winds due to gravity waves were different between winter and summer.

The ratio of E_{sh} to E_{sw}, also plotted in Fig. 5.16, did not show significant seasonal variations at 6.5–8 and 15.5–17, but annual variation was fairly evident at 11–12.5 km, with a winter maximum and a summer minimum.

Long Period (2–21 hr) Component

In this subsection, we discuss seasonal variation of the gravity wave energy for the long period component (2–21 hr), E_ℓ. Figure 5.17 shows a time-height section of E_ℓ, indicating that the E_ℓ values were generally larger in the troposphere, while E_ℓ in the lower stratosphere became small. Note that the contour levels are different from those in Fig. 5.12 for the short period (5 min–2 hr) component.

The E_ℓ values at 5 to 8–12 km were generally larger in winter, while their enhancement at about 10–13 km was significant in spring–early summer, as indicated by the contour of 7.5 Jm^{-3}. The region of large E_ℓ values seemed to be restricted below the tropopause, not penetrating into the stratosphere.

In the lower stratosphere, E_ℓ showed fairly clear annual variation with maxima centered in January and with minima in September, which can be recognized, e.g., from the contour line of 2.5 Jm^{-3}. Time series of E_ℓ in the height regions of 6.5–8, 11–12.5 and 15.5–17 km are presented in Fig. 5.18. The annual variation, with winter maxima and summer minima, was rather clear at 6.5–8 and 15.5–17 km, although the amplitudes in the latter height range were 1/4–1/3

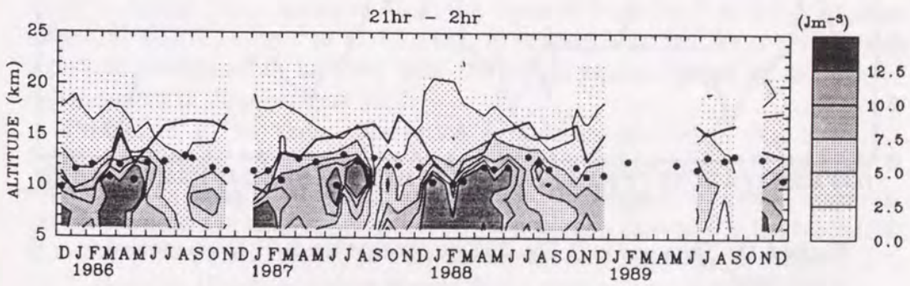

Figure 5.17: The same as in Fig. 5.12 except that the 2–21 hr component is presented with different contour levels.

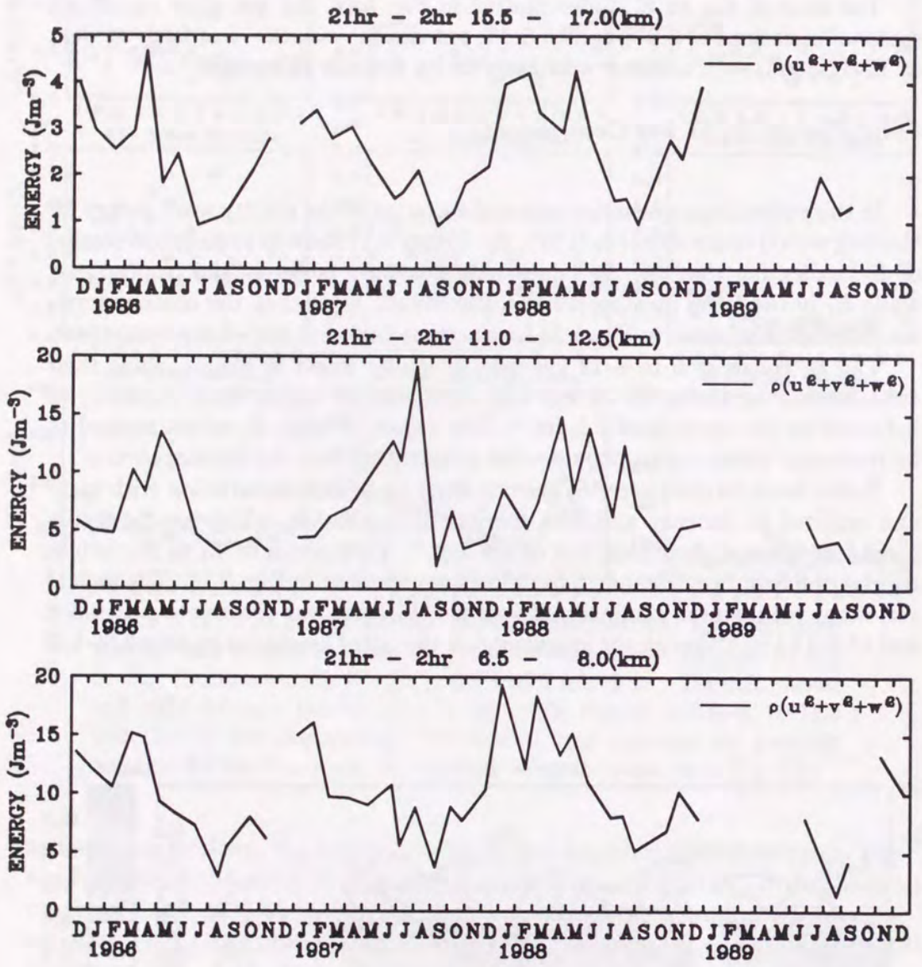

Figure 5.18: The same as in Fig. 5.13 except that the 2–21 hr component is presented.

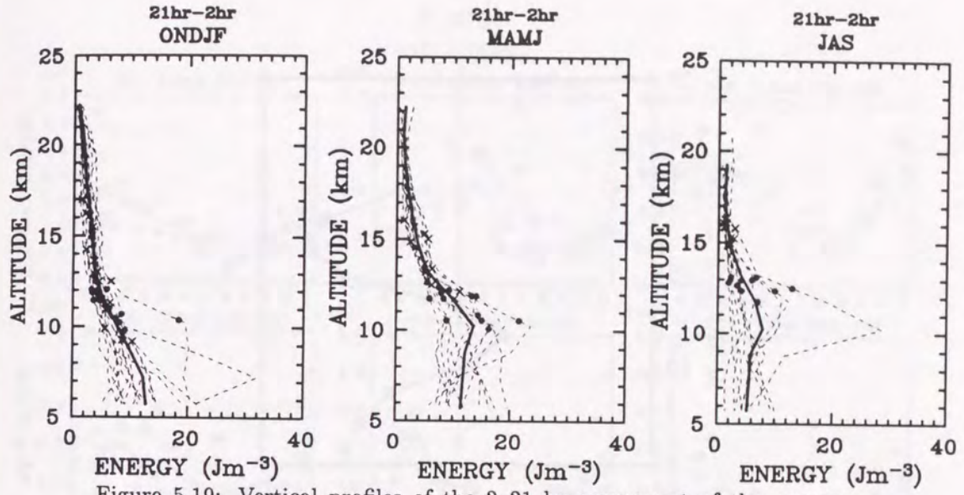

Figure 5.19: Vertical profiles of the 2–21 hr component of the energy density, E_ℓ. (Left panel) E_ℓ mainly in winter months such as January, February and October–December, the data in the center panel being for spring–early summer (March–June). (Right panel) The profiles in summer (July–September). The thick lines indicate the mean profiles. Crosses and closed circles represent the tropopause height and the peak height of the mean wind speed, respectively.

of those in the former region. While, E_ℓ at 11–12.5 km was mainly enhanced in March–August, showing a different seasonal cycle from those at 6.5–8 and 15.5–17 km.

In winter (e.g., January, February and December), the E_ℓ value at 6.5–8 km was about 8–20 Jm^{-3}, which was roughly twice as large as that at 11–12.5 km, while in spring (e.g., March to May) the value of 8–18 Jm^{-3} at 6.5–8 km was comparable to 6–14 Jm^{-3} at 11–12.5 km. In summer–autumn, we could not find significant change of E_ℓ between these two height ranges, except for anomalous enhancement in June–August 1987.

Profiles of E_ℓ for three observation periods are plotted in Fig. 5.19: (i) October–February, (ii) March–June, and (iii) July–September. In period (i), corresponding to a period of large mean winds, the E_ℓ profiles showed large values only within the troposphere, that is, E_ℓ generally showed the largest values of 8–20 Jm^{-3} at 5 km, tended to decrease almost monotonously to values of 1–3 Jm^{-3} at about 13 km, and then showed fairly small values above.

In period (ii), E_ℓ showed a slight increase at 5–10 km and then rapidly decreased above 10 km. Note that these peaks near 10 km can be identified as

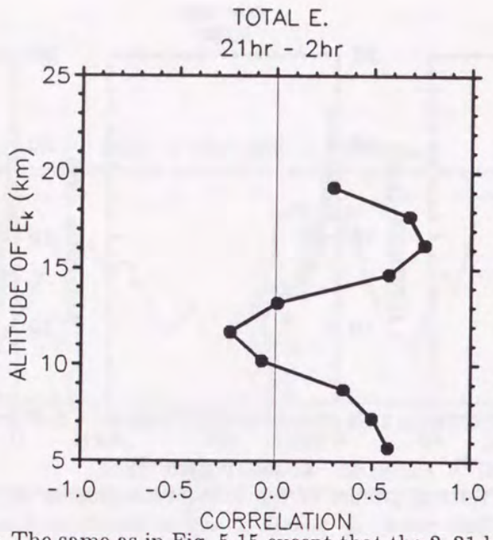

Figure 5.20: The same as in Fig. 5.15 except that the 2–21 hr component is presented.

the spring maxima in the time-height section in Fig. 5.12, a peculiar seasonal variation being produced at 11–12.5 km, which was different from those in the regions above and below.

In period (iii), the E_ℓ values were smaller than in other periods, and the general characteristics of the profile were similar to those in period (ii).

The cross correlation coefficients at zero lag between E_ℓ and $\overline{U}_{12km}$ in Fig. 5.20 were positive at 5–9.5 and 9.5–20 km, and negative at 9.5–14 km. This suggested that the seasonal variations of E_ℓ in the lower stratosphere as well as in the middle troposphere agreed with the $\overline{U}_{12km}$ variation, although we found that the stratospheric values of E_ℓ were generally smaller than the tropospheric ones, as can be seen in Fig. 5.19.

For long period gravity waves, horizontal and vertical components of kinetic energy, $E_{\ell h}$ and $E_{\ell w}$, and their ratio are plotted in Fig. 5.21 in three height regions. Since $E_{\ell h}$ is a major part of E_ℓ, the behavior of $E_{\ell h}$ was quite similar to that of E_ℓ, showing clear annual variation with winter maxima and summer minima at 6.5–8 and 15.5–17 km, while at 11–12.5 km the maxima appeared in spring. The ratio of the maximum to the minimum values of $E_{\ell h}$ were in the range of 2.8–3.6 in the three height regions. Kinetic energy for the vertical motion, $E_{\ell w}$, exhibited a clear annual cycle with a winter maximum and a summer minimum in all three height ranges, although the ranges of the seasonal changes

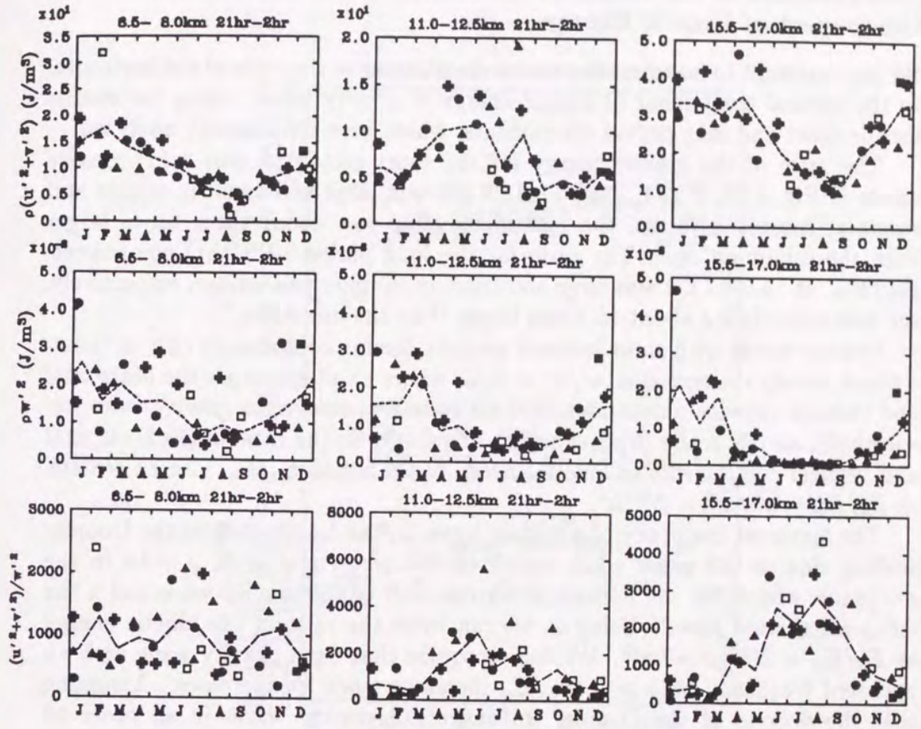

Figure 5.21: The same as in Fig. 5.16 except that the 2–21 hr component is presented.

differed among the three altitude regions, such that at 6.5–8 and 11–12.5 km, the maxima were larger than the minima by a factor of about 5–6, while at 15.5–17 km the factor was as large as about 42.

The ratio, $E_{\ell h}/E_{\ell w}$, demonstrated an annual cycle with persistently small values in winter at 11–12.5 and 15.5–17 km altitudes, although the maxima occurred in June and August at 11–12.5 and 15.5–17 km, respectively. While, it showed no significant seasonal variation at 6.5–8 km. In particular, $E_{\ell h}/E_{\ell w}$ at 15.5–17 km showed large values, ranging from about 200 to 2900, while it ranged from 700 to 1200 at 6.5–8 km.

Interpretation of the Ratios of the Horizontal to the Vertical Component of Kinetic Energy

We here attempt to interpret the seasonal variations of the ratio of the horizontal to the vertical component of kinetic energy of gravity waves, using the results for the short and long period components, which were separatively analyzed.

The ratio of the kinetic energy for the short period (5 min–2 hr) gravity waves in Fig. 5.16, E_{sh}/E_{sw}, at 11–12.5 km was large and small in winter and summer, respectively, and the maximum value was about three times larger than the minimum one. The ratio for the long period (2–21 hr) component, $E_{\ell h}/E_{\ell w}$, at 15.5–17 km was large and small in summer and winter, respectively, the maximum being about 15 times larger than the minimum.

Gravity waves with short intrinsic periods, having components only in the x-z plane, satisfy the equation, $u'/w' = N/\hat{\omega}$, where u', w' and $\hat{\omega}$ are the horizontal and vertical velocity amplitudes, and intrinsic frequency of a gravity wave, respectively, and N is the Brunt-Väisälä frequency. So the ratio of the horizontal and vertical components of kinetic energy of the wave, E_h/E_w, can be written as $E_h/E_w = \overline{u'^2}/\overline{w'^2} = N^2/\hat{\omega}^2$.

The apparent frequency of a gravity wave, ω, can be affected by the Doppler shifting due to the mean wind, which can be written as $\omega = \hat{\omega} + ku$ in the x-z plane, where k is the horizontal wavenumber of the gravity wave and u the mean zonal wind speed. Using ω, we can write the ratio of the kinetic energy as $E_h/E_w = N^2/(\omega - ku)^2$. We can recognize that for a gravity wave with an apparent frequency of $\omega > 0$, E_h/E_w increases when ku increases. Assuming that the degrees of the Doppler shifting of all gravity waves in an observed frequency range (5 min–2 hr or 2–21 hr) are approximately identical, we can apply the behavior of E_h/E_w of a wave to the observed results for E_{sh}/E_{sw} and $E_{\ell h}/E_{\ell w}$.

The observed annual variation of the short period component, E_{sh}/E_{sw}, at 11–12.5 km could be qualitatively understood as the N^2 variation with a large value in winter and a small value in summer, because the height region of 11–12.5 km was in the troposphere in summer (where typically $N \sim 1/10$ min) and in the stratosphere in winter ($N \sim 1/5$ min).

For the long period component, the seasonal variation of $E_{\ell h}/E_{\ell w}$ at 15.5–17 km with a summer maximum could not be explained by the N^2 variation. The long period gravity waves dominantly propagated westward ($k < 0$), as inferred from the zonal momentum flux, which is described in the next section, and the mean wind direction was generally eastward ($u > 0$), so the mean wind variation with a winter maximum suggests that ku was negative, and was large and small in summer and winter, respectively, which implies the variation of $E_{\ell h}/E_{\ell w}$ with

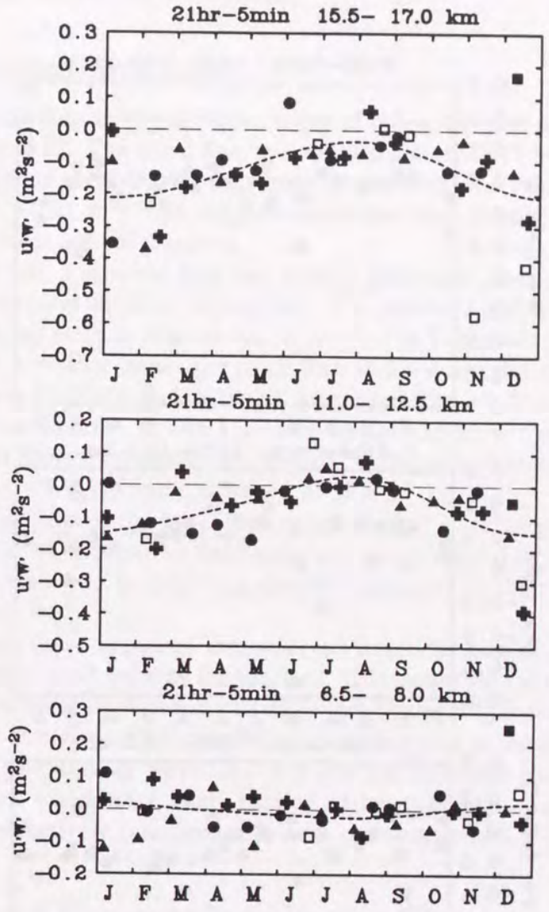

Figure 5.22: Zonal momentum flux for the periods of 5 min–21 hr at the heights of 15.5–17 (top), 11–12.5 (middle) and 6.5–8 km (bottom). Each dashed line indicates the least-squares fit of a mean, annual and semiannual components. The symbols represent data for 1985 to 1989, as described in Fig. 5.11.

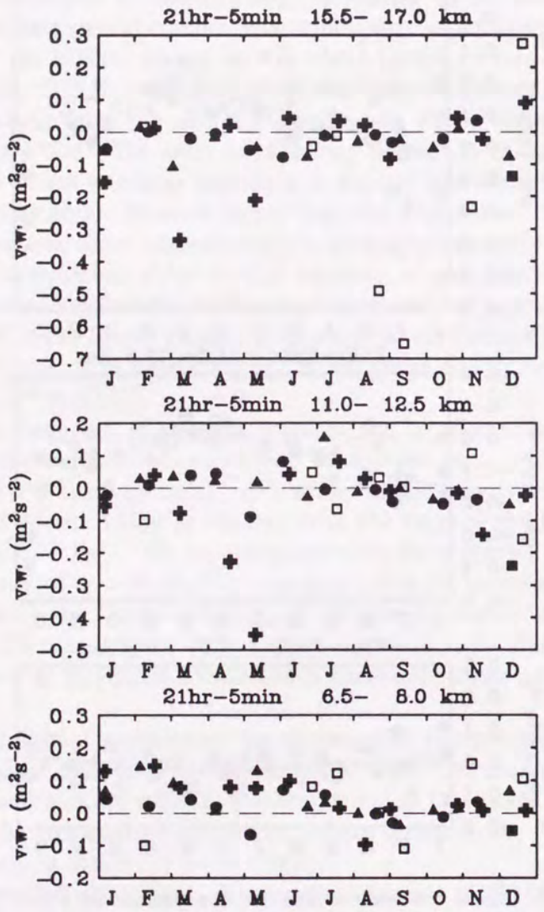

Figure 5.23: The same as in Fig. 5.22 except that meridional momentum flux is presented without a fitted curve.

large and small values in summer and winter, respectively. Therefore, considering the Doppler shifting effect, the observed seasonal variation of E_{th}/E_{tw} could be understood to be caused by the variation in the mean wind speed a with winter maximum and a summer minimum.

5.2.3 Momentum Flux

Zonal momentum flux in the altitude ranges of 6.5–8, 11–12.5 and 15.5–17 km is shown in Fig. 5.22. The zonal flux was westward at 15.5–17 km in almost all months throughout the four successive years, moreover, the values varied from about –0.03 to –0.21 m^2s^{-2} in August–September and January, respectively, showing fairly clear annual variation.

At 11–12.5 km, the zonal flux was mostly westward throughout the year except for some cases in June–September. The seasonal variation was nearly annual, with values ranging from about –0.15 m^2s^{-2} in December to +0.05 m^2s^{-2} in August. On the other hand, the zonal flux at 6.5–8 km did not exhibit any significant seasonal variations, but the values ranged from –0.15 to +0.25 m^2s^{-2}.

Meridional momentum flux in the three height ranges is also presented in Fig. 5.23, which showed no significant seasonal variations, although it tended to be northward at 6.5–8 km and southward at 15.5–17 km.

The westward bias of the zonal momentum flux at 11–12.5 and 15.5–17 km in Fig. 5.22 could be understood if the eastward winds, caused by the jet stream, filtered out the eastward propagating gravity waves due to their interaction at the critical level.

At 6.5–8 km, there appeared the observed less clear bias of the zonal flux but large energy of wind velocity fluctuations. It is suggested that a comparable amount of the momentum flux was carried by gravity waves propagating zonally but in opposite directions. One possibility to explain this is that the zonal flux due to upward propagating waves at 6.5–8 km was balanced with that due to downward waves, which were likely excited at lower heights and near the jet stream peak, respectively [Yamanaka, *private communication*].

5.3 Lidar Observations in the Stratosphere and Lower Mesosphere

While the MU radar observations has revealed distributions of the kinetic energy of gravity waves in terms of the wind velocity variance, the potential energy of gravity waves can be observed with Rayleigh lidars by analyzing the density fluctuations and temperature. Wilson et al. [1991b] investigated the potential

energy of gravity waves in the stratosphere and mesosphere to show the seasonal variations of gravity wave activity over two sites, that is, Observatoire de Haute Provence (OHP) (44° N, 6° E) and Biscarosse (BIS) (44° N, 1° W).

Here we present the potential energy density values observed with the Rayleigh lidar of NIES, Tsukuba (36°N, 140°E), comparing with the results of Wilson et al. [1991b] at the different latitudes and longitudes.

The available potential energy density per unit mass, E_p, could be inferred from the relative density fluctuations ρ'/ρ_0 and the Brunt-Väisälä frequency N as:

$$E_p = \frac{1}{2}N^2\overline{\zeta^2} = \frac{1}{2}\left(\frac{g}{N}\right)^2\overline{\left(\frac{\rho'}{\rho_0}\right)^2} \tag{5.1}$$

where ζ is the vertical displacement of an air parcel and g is the gravitational acceleration [Chanin and Hauchecorne, 1981, 1984; Wilson et al., 1991b]. N was calculated from the vertical derivative of the observed temperature.

We obtained the daily mean vertical wavenumber spectrum of the relative density fluctuations calculated from hourly density profiles, estimated the noise level of the spectra, then integrated the spectrum in the wavenumber range of 6.7×10^{-5}–1×10^{-3} cyc/m (1–15 km in wavelength), and subtracted the energy of noise inferred from noise level of the spectra to obtain the daily value of E_p. Data were eliminated when the temperature fluctuations occurred due to the enhancements of planetary wave activity, in order to extract only the variance mainly due to gravity waves. Data were removed when the S/N ratio was smaller than 1.5 and/or the energy of noise was larger than 10 and 200 Jkg^{-1} at 30–45 and 45–60 km, respectively.

The seasonal variation of E_p in the upper stratosphere (30–45 km) is shown in Fig. 5.24 in comparison with the results by Wilson et al. [1991b] in the same height range observed at OHP and BIS. The monthly mean value was as large as 7–12 Jkg^{-1} in January, February and October–December, while it was small with the values of 3–5 Jkg^{-1} in May–August. The monthly means at Tsukuba reasonably agreed with the results at BIS indicating the tendency of the decrease of E_p from January to June. Although the E_p values at OHP were about 1.1–1.7 times larger than the determinations at Tsukuba in January–March, they tended to agree with the Tsukuba data in June and August. The mean E_p values in October and November were approximately twice as large as the values of OHP and BIS, while E_p in December was about 1.2 times as large as the OHP and BIS observations.

We can recognize that the E_p values at Tsukuba showed an annual variation illustrating the tendency of larger and smaller values in winter and summer, respectively, as is also shown by the results of the OHP and BIS observations, although E_p in autumn–early winter exhibited enhancements with values as large as in January at OHP.

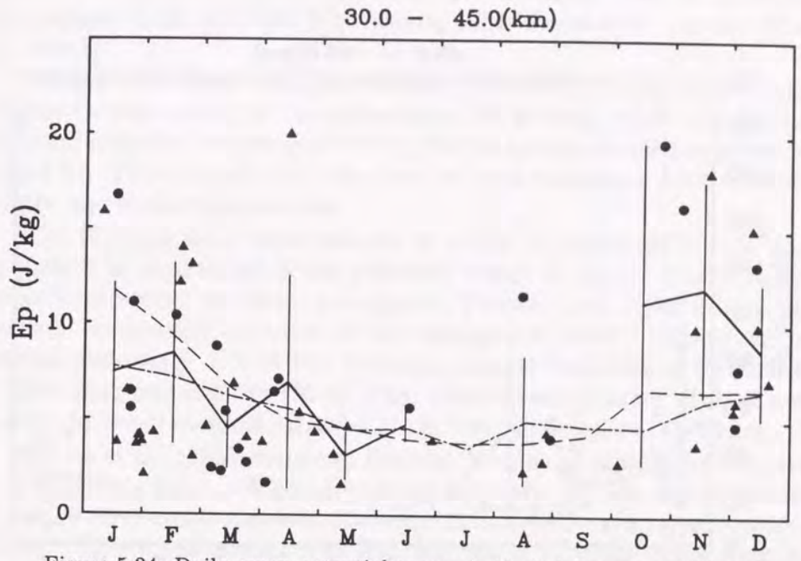

Figure 5.24: Daily mean potential energy in the height range of 30–45 km observed with Rayleigh lidar of NIES, in 1990 (circle) and 1991 (triangle), solid lines and vertical bars indicating the monthly means and standard deviations. Dashed and dot-dashed lines represent the monthly means of E_p observed at OHP (44°N, 6°E) and BIS (44°N, 1°W) in 1986–1989 [after Wilson et al. 1991b].

The daily mean values in the lower mesosphere (45–60 km) is presented in Fig. 5.25. Although it is difficult to discuss the seasonal variation of E_p at 45–60 km due to a fairly long period of the missing data in June, July, September and October, we can recognize that the monthly means in January–May, August, November and December showed the values comparable to the results at OHP and BIS. The monthly means of E_p could be found to be in the range of 20–50 Jkg^{-1}, about 1–2.5 times as large as the OHP and BIS determinations.

From the above results, the mean value at 30–45 km was found to be about 7.2 Jkg^{-1}, while the values at OHP and BIS were 6.5 and 5.8 Jkg^{-1}, respectively, thus the value at Tsukuba was larger than those in France by a factor of 1.1 and 1.2, respectively. In the height range of 45–60 km, the average of all data at Tsukuba, OHP and BIS were 31.7, 24.2 and 15.8 Jkg^{-1}, respectively, the ratios of the value at Tsukuba to OHP and BIS being about 1.3 and 2.0, respectively.

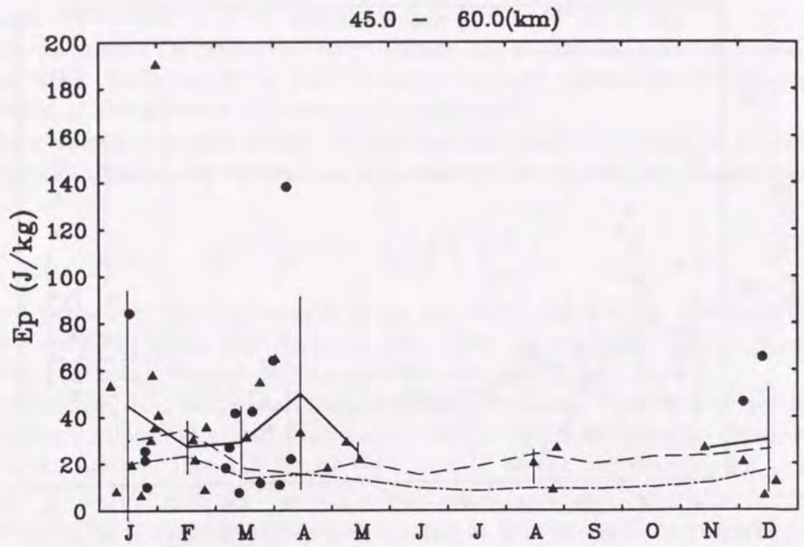

Figure 5.25: The same as Fig. 5.24 except for the results in the lower mesosphere (the height range of 45–60 km).

So, although the sampled data at Tsukuba were significantly missing especially in the height range of 45–60 km, the gravity wave activity at Tsukuba (35°N) seemed slightly larger than those at OHP and BIS (44°N) by a factor of roughly 1.1–2.0.

From the rocketsonde observations, Hirota [1984] reported that the annual mean value of the intensity of the temperature fluctuations induced by gravity waves was larger at middle latitudes centered in 25°N than those at higher latitudes, which showed that the annual mean at 35°N was larger than at 44°N by a factor of about 1.3. The results of the observations at Tsukuba, OHP and BIS seem to agree with the tendency of the latitudinal variation shown by Hirota [1984], despite Hirota's analysis of the different component of gravity waves.

5.4 Discussions

In previous observational studies, statistical analyses of gravity wave activity were performed at different height ranges, such as the stratosphere and mesosphere, by means of various measurement techniques, such as rocketsondes, atmospheric radar and lidar [e.g., Hirota, 1984; Tsuda et al., 1990b; Wilson et al., 1991b].

Using the MU radar data, we revealed in Section 5.1 a semiannual variation of gravity wave energy in the mesosphere (65–85 km), which was determined by integrating the frequency spectrum of wind velocity in the period range of 5 min–2 hr. The seasonal cycle was found to have maxima in both summer and winter, and equinoctial minima.

The Rayleigh lidar measurements at NIES, Tsukuba (36°N, 140°E) were employed for observation of the potential energy of gravity waves, E_p, in the upper stratosphere and lower mesosphere. We calculated E_p by integrating the vertical wavenumber spectrum of the atmospheric density fluctuations in the vertical scale range of 1–15 km. Dominant annual variations of E_p were shown in the upper stratosphere (30–45 km), although the number of data was not enough to reveal seasonal variation in the lower mesosphere (45–60 km).

Wilson et al. [1991b] employed Rayleigh lidar measurements at mid-latitude in France (e.g., 44°N, 6°E) for climatological study of the seasonal variation of E_p in the three height ranges in the upper stratosphere–middle mesosphere (30–75 km). They found dominant annual variation of E_p in the upper stratosphere (30–45 km) as well as the results at Tsukuba. An annual cycle in the lower mesosphere (45–60 km) was also shown although the range of the seasonal change in E_p became smaller there. Semiannual variation with maxima in summer and winter was detected in the middle mesosphere (60–75 km).

These results mentioned above are summarized in Fig. 5.26. The top and bottom panels present the gravity wave energy inferred from the wind velocity variance including the entire wavenumber component, while the middle three panels show the potential energy of gravity waves which was inferred from the vertical wavenumber spectrum of the atmospheric density fluctuations, which includes the entire frequency component. Thus we are unable to compare quantitatively these components of the wave energy, but we may qualitatively compare the seasonal behaviors in these height regions with each other.

We can recognize the dominant annual variation with a maximum in winter and a minimum in summer in the lower stratosphere (15.5–17 km), and the semiannual variation with maxima in summer and winter in the upper mesosphere (65–85 km). The lidar results for the upper stratosphere to the middle mesosphere showed reasonable interpolation of the seasonal variations in the lower stratosphere and upper mesosphere, illustrating that the annual variation with a winter maximum seemed depressed with altitude and the semiannual component became evident in the mesosphere.

We described the agreement between the annual cycles of the gravity wave

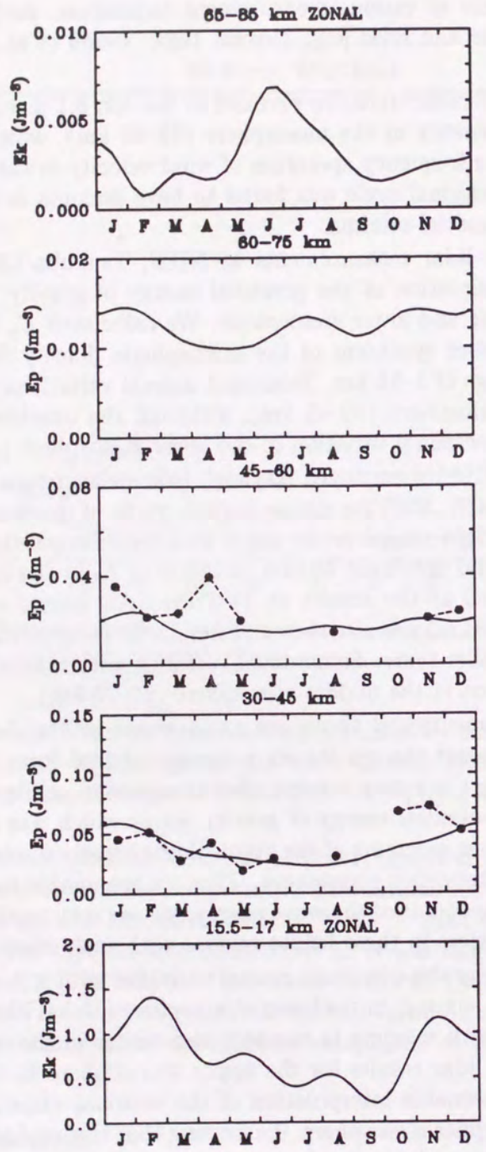

Figure 5.26: The seasonal variations of gravity wave activity observed with the MU radar (35°N, 136°E) (top and bottom panels) and Rayleigh lidars. Lidar results (middle three panels) are shown for the observation at Tsukuba, Japan (36°N, 140°E) (dashed lines) and OHP, France (44°N, 6°E) (solid lines) (After Tsuda et al. [1990b] and Wilson et al. [1991b]).

energy in the lower stratosphere and the mean wind intensity, while Wilson et al. [1991b] also detected a positive correlation between the wave energy variation at 30–45 km and the mean wind intensity at 5 mb. These seasonal cycles with winter maxima at mid-latitudes imply that the mean flow in the lower atmosphere, where the jet stream is dominant, may play an important role in the excitation and filtering process in the propagation of gravity waves in the troposphere and stratosphere.

In the mesosphere, semiannual cycles were demonstrated with both summer and winter maxima, and equinoctial minima, and we know that the mean wind speed at mesospheric heights shows maxima also in summer and winter at mid-latitudes, although the wind direction is generally westward and eastward, respectively. So a relation between the gravity wave activity and the mean wind amplitude could also be suggested in the mesosphere. More investigation of the climatology of mesospheric dynamics is expected.

Chapter 6

Summary

We have studied altitude and seasonal variations of gravity wave characteristics in the middle atmosphere employing the MU radar observations and also using the complementary measurement techniques such as rocketsondes and lidars. These observations enabled us to cover the height range throughout the middle atmosphere at middle latitudes.

Theoretical studies have pointed out that gravity waves may play an important role for the momentum budget and energy transport in the middle atmosphere, where momentum deposition due to gravity wave dissipation has been expected to cause mean flow acceleration. As a wave dissipation process, saturation of gravity waves has been proposed, which is thought to contribute to breaking of the waves and consequently to interaction with the larger scale motions.

The linear saturation theory of gravity waves was briefly reviewed, which explains the dependency of amplitudes of gravity waves on vertical wavenumber. It can be further applied to interpretation of altitude variation of dominant vertical scales of the waves.

In Chapter 2, we described the experimental technique of the MU radar, which is the main facility to provide wind velocity data for gravity wave analysis in this thesis. Spectral analysis and data reduction for the MU radar data was briefly stated, which was employed for description of the gravity wave field as there was superposition of many waves with various wavenumbers and frequencies. Observation techniques of rocketsondes and a Rayleigh lidar were also described, which complement the MU radar observations that have a data gap region of 25–60 km.

The rocketsonde experiments were conducted at Uchinoura (31°15'N, 131°05'E) employing three types of rockets equipped with datasondes and a passive falling sphere, which can observe horizontal wind velocity and temperature in the height

range from 20 km to 60–100 km, although only snap-shot profiles are obtained. Using spectral analysis, we estimated the maximum height for depicting wind velocity fluctuations induced by gravity waves, and it was about 60 km when the height resolution was 3 km.

The atmospheric density and temperature observations in the upper stratosphere and lower mesosphere were carried out in 1990–1991 with a Rayleigh lidar at NIES (the National Institute for Environmental Studies), Tsukuba (36°N, 140°E), Japan. Temperature profiles were derived from differentiation of air density profiles with respect to altitude, assuming a hydrostatic equilibrium.

In Chapter 3, we showed the altitude variation of gravity wave characteristics in the middle atmosphere, and attempted to explain them in terms of the linear saturation theory of gravity waves. Analysis of snap-shot profiles of the wind velocity fluctuations in the middle atmosphere observed with the MU radar and rocketsondes led to the results as follows.

(3-1) The vertical scale and amplitude of the dominant gravity wave clearly increased with altitude. The dominant scale was 2–3 km in the lower stratosphere, about 5–10 km in the upper stratosphere, and became larger than 10 km in the mesosphere.

(3-2) Vertical wavenumber spectra of horizontal wind fluctuations were determined in the middle atmosphere. Spectral shape was more gradual in the lower stratosphere than the saturated spectrum model, became steeper as altitude increased, and then reached the model value in the upper mesosphere. Spectral densities at large vertical scales of about 5–10 km were generally smaller than the model in the stratosphere, grew with height, and approached the model values in the upper mesosphere.

The spectra indicate that gravity waves, with vertical scales larger than 2–3 km, were not fully saturated in the stratosphere, while in the mesosphere the observed spectra were well described by the model.

(3-3) Detailed investigation of vertical profiles of the wind velocity variance was conducted. The variance generally increased with altitude in the stratosphere, diminished just above the stratopause, and greatly increased again in the lower mesosphere. Mean variance profiles in the upper mesosphere indicated fairly constant values with altitude, implying that wave amplitudes were restricted by the wave saturation.

(3-4) By scaling the wind velocity variance by the atmospheric density, it was found that the gravity wave energy per unit volume generally decreased in the stratosphere and upper mesosphere, while it was fairly constant just above the stratopause, indicating that wave dissipation may not be significant in this region.

In Chapter4, the results of the climatological analysis of gravity wave spectra

were presented from the MU radar observations.

(4-1) In the lower stratosphere in December 1985–December 1989, monthly frequency spectra were obtained in the period range of 5 min–21 hr. The vertical component at lower frequencies around 21 hr showed large and small values in winter and summer, respectively, and the spectral slopes were negative and steep in winter and nearly flat in summer. Oblique wind spectra showed a slope of around –5/3 throughout a year, and the amplitudes at the lower frequencies were larger and smaller in winter–spring and in summer, respectively.

(4-2) Mesospheric spectra were calculated in the period range of 5 min–2 hr in December 1985–December 1988. While the shapes for vertical wind velocity were gradual or flat in equinoctial months and steep in summer and winter, spectral slopes for the oblique component were around –5/3 at the periods longer than 20 min throughout a year. Spectral densities of both the vertical and the oblique components at low frequencies ($\sim$ 2 hr) tended to be large and small in equinoxes and solstices, respectively.

(4-3) Mean wind dependence of the spectral shape for the vertical component both in the troposphere–lower stratosphere and in the mesosphere was examined. It was shown that spectral slopes became steeper as the mean wind intensity increased.

(4-4) Vertical wavenumber spectra in the mesosphere in December 1985–December 1988 agreed well with the saturated spectrum model, without a significant seasonal variation. It is suggested that gravity waves with vertical scales smaller than at least about 10 km are always saturated in the mesosphere.

(4-5) From a case study in August 1988, the vertical component of saturated gravity waves in the lower stratosphere showed a dominant component around the long period of $\sim$14 hr.

In Chapter 5, we investigated seasonal variations of gravity wave activity and wave momentum flux using the MU radar observations in the troposphere–lower stratosphere in 1985–1989 and the mesosphere in 1985–1988. Gravity wave activity in the upper stratosphere and lower mesosphere was observed with a Rayleigh lidar at NIES, Tsukuba, Japan (36°N), combined with the lidar results at Haute Provence (OHP) and Biscarosse (BIS), France (44°N for both sites) by Wilson et al. [1991b].

(5-1) For gravity wave activity with the periods of 5 min–2 hr in the mesosphere, the MU radar observations showed semiannual variation with fairly persistent summer peaks and rather irregular winter peaks, and with equinoctial minima.

(5-2) The zonal momentum flux observed with the MU radar showed a clear annual cycle with eastward and westward maxima in summer and winter, respectively, although no significant seasonal variation was detected for the meridional flux. Furthermore, the zonal mean flow acceleration in the upper mesosphere was westward and eastward in summer and winter, respectively, which was quantitatively consistent with theoretical predictions.

(5-3) From MU radar observations in the lower atmosphere, the seasonal variation of gravity wave energy was shown in comparison with jet stream activity. The wind velocity variance exhibited a clear annual variation, having a maximum in winter, which correlated quite well with the variation of the jet stream intensity.

(5-4) The kinetic energy per unit volume for the short period (5 min–2 hr) range enhanced near the peak mean wind height ($\sim$ 12 km). The long period (2–21 hr) component showed clear annual variation with winter maxima in the middle troposphere and lower stratosphere (larger in the troposphere).

(5-5) A detailed analysis of the energy of the vertical and horizontal motions was conducted. It was implied that the excitation mechanisms of the waves with periods longer and shorter than two hours seemed to be an interaction of the local topography with the jet steam and the mean wind peak due to the jet, respectively.

(5-6) Annual cycles with winter maxima were also detected in the 30–45 km range from the lidar observations at Tsukuba as well as those at two sites (OHP and BIS) in France [Wilson et al., 1991b], but at 45–60 km the seasonal variations were rather featureless. The lidar results at OHP and BIS in the height range of 60–75 km showed semiannual variations with similar enhancements both in summer and in winter.

(5-7) The mean values of the potential energy of gravity waves in the height range of 30–45 and 45–60 km at Tsukuba (36°N) were a little larger than those at OHP and BIS (44°N) [Wilson et al., 1991b]. This latitudinal variation seemed consistent with the results shown by Hirota [1984], although other factors such as the local topography might also be important for the determination of gravity wave activity.

(5-8) Combining the MU radar and lidar results, the height variation of the seasonal cycle of gravity wave activity could be recognized. Annual variations with winter maxima were dominant in the stratosphere, while semiannual variations with solstitial peaks were found in the mesosphere.

As summarized above, the climatologies and the case studies have provided evidence for the important role of gravity waves which has been theoretically predicted. They have also given the findings on the gravity wave saturation, the wave behavior around the stratopause, and the results related to the wave excitation in the lower atmosphere. The revealed vertical transport of the wave energy and momentum, as well as the climatology, at middle latitudes provides quantitative understanding of a part of the coupling processes between different

height regions, a target of the Solar Terrestrial Energy Program (STEP).

These results enable us to suggest a plausible simple scenario about the behavior of gravity waves in the middle atmosphere as follows. Gravity waves, which are excited in the lower atmosphere mainly due to effects related to the jet stream, propagate upward without being fully saturated in the stratosphere. The gravity wave activity in the stratosphere shows an annual variation with a winter maximum, which seems to occur in line with the climatology of wave excitation due to effects related to the jet stream.

The upward propagating waves reach the stratopause region, above which the wave amplitudes apparently become smaller than the saturation level, according to the rapid decrease of the background static stability. Therefore the upward waves grow exponentially with altitude and conserve the wave energy in the lower mesosphere. It is suggested that the background temperature structure probably controls the wave propagation through the stratopause.

Finally the waves are fully saturated in the upper mesosphere and deposit the wave momentum to decelerate the mean wind, which forms the weak zonal wind layer around the mesopause. However, all the wave energy does not necessarily seem to be lost there, and a part of the energy may penetrate into the thermosphere. This may have a significant effect on the larger scale motions in the lower thermosphere, which is related to mesosphere-thermosphere coupling. The relative effects of gravity and tidal waves (the latter also become significant in the thermosphere) should be considered.

The seasonal variation in the upper mesosphere was semiannual with maxima in summer and winter, when the large wave activity tends to coincide with the strong middle atmosphere jet, as well as maxima of wave momentum. However, we have no clear explanation of the reason why the mesospheric cycle does not agree with the annual cycle in the stratosphere which is probably caused by wave excitation. A possible candidate to cause the mesospheric cycle is the interaction with the middle atmosphere jet, but any such mechanism is not clearly understood.

Atmospheric phenomena in regions at other latitudes such as the equatorial and polar regions, are also of great interest. In particular, comprehensive observations of the equatorial atmosphere do not seem enough to date, even though wave excitation is considered to be more significant there because of more active disturbances due to the maximum in solar heat input and weaker wave dumping due to the smaller Coriolis force. In the polar regions, the dynamical transport of ozone as well as the horizontal and vertical large scale motions can be important problems. Extensive observations are expected on the more global basis.

References

Andrews, D. G., J. R. Holton, and C. B. Leovy, *Middle Atmosphere Dynamics*, Academic Press, 259–294, 1987.

Balsley, B. B. and D. A. Carter, The spectrum of atmospheric velocity fluctuations at 8 and 86 km, *Geophys. Res. Lett.*, **9**, 465–468, 1982.

Blackman, R. B. and J. W. Tukey, *The measurement of power spectra from the point of view of communications engineering*, Dover, New York, 1959.

Bollermann, G., A study of 30 km to 200 km meteorological rocket sounding systems, *Contractor Report*, **NASA CR-1529**, 1970.

Chanin, M. L. and A. Hauchecorne, Lidar observation of gravity and tidal waves in the stratosphere and mesosphere, *J. Geophys. Res.*, **86**, 9715–9721, 1981.

Chanin, M. L. and A. Hauchecorne, Lidar studies of temperature and density using Rayleigh scattering, *MAP Handbook*, **13**, edited by R. A. Vincent, pp. 87–99, SCOSTEP, Urbana, Illinois, 1984.

CIRA 1972, *COSPAR International Reference Atmosphere*, Akademie-Verlag, Berlin, 1972.

CIRA 1986, *COSPAR International Reference Atmosphere: 1986*, Part II: Middle Atmosphere Models (D. Rees, J. J. Barnett and K. Labitzke, eds.), Pergamon Press, 1990.

Cornish, C. R. and M. F. Larsen, Observations of low-frequency inertia-gravity waves in the lower stratosphere over Arecibo, *J. Atmos. Sci.*, **46**, 2428–2439, 1989.

Desaubies, Y. J. F., Analytical representation of internal gravity wave spectra, *J. Phys. Oceanogr.*, **6**, 976–981, 1976.

Dewan, E. M., N. Grossbard, A. F. Quesada, and R. E. Good, Spectral analysis of 10 m resolution scalar velocity profiles in the stratosphere, *Geophys. Res. Lett.*, **11**, 80–83, 1984 (Correction, *Geophys. Res. Lett.*, **11**, 624, 1984).

Dewan, E. M., and R. E. Good, Saturation and "universal" spectrum for vertical profiles of horizontal scalar winds in the atmosphere, *J. Geophys. Res.*, *91*, 2742–2748, 1986.

Ebel, A., A. H. Manson, and C. E. Meek, Short period fluctuations of the horizontal wind measured in the upper middle atmosphere and possible relationships to internal gravity waves, *J. Atmos. Terr. Phys.*, **49**, 385–401, 1987.

Eckermann, S. D., and R. A. Vincent, Falling sphere observations of anisotropic gravity wave motions in the upper stratosphere over Australia, *Pure Appl. Geophys.*, **130**, 509–532, 1989.

Ecklund, W. L., D. A. Carter and B. B. Balsley, Continuous measurement of upper atmospheric winds and turbulence using a VHF Doppler radar: Preliminary results, *J. Atmos. Terr. Phys.*, **41**, 983–994, 1979.

Endlich, R. M. and R. C. Singleton, Spectral analysis of detailed vertical wind speed profiles, *J. Atmos. Sci.*, **26**, 6975–6983, 1969.

Ference, M., W. G. Stroud, J. R. Walsh, and A. G. Weinsner, Measurement of temperatures at elevations of 30 to 80 kilometers be the rocket-grenade experiment, *J. Atmos. Sci.*, **13**, 5–12, 1956.

Fritts, D. C., Gravity wave saturation in the middle atmosphere: A review of theory and observations, *Rev. Geophys. Space Phys.*, *22*, 275-308, 1984.

Fritts., D. C., A numerical study of gravity wave saturation: nonlinear and multiple wave effects, *J. Atmos. Sci.*, **42**, 2043–2058, 1985.

Fritts, D. C., and T. E. VanZandt, Effects of Doppler shifting on the frequency spectra of atmospheric gravity waves, *J. Geophys. Res.*, **92**, 9723–9732, 1987.

Fritts, D. C., and G. D. Nastrom, Sources of mesoscale variability of gravity waves. Part II: Frontal, convective, and jet stream excitation, *J. Atmos. Sci.*, **49**, 101–110, 1992.

Fritts, D. C., and R. A. Vincent, Mesospheric momentum flux studies at Adelaide, Australia: observations and a gravity wave-tidal interaction model, *J. Atmos. Sci.*, **44**, 605–619, 1987.

Fritts, D. C., and D.-Y. Wang, Doppler-shifting effects on frequency spectra of gravity waves observed near the summer mesopause at high latitude, *J. Atmos. Sci.*, **48**, 1535–1544, 1991.

Fritts, D. C., T. Tsuda, T. Sato, S. Fukao and S. Kato, Observational evidence of a saturated gravity wave spectrum in the troposphere and lower stratosphere, *J. Atmos. Sci.*, **45**, 1741–1759, 1988.

Fukao, S., T. Sato, T. Tsuda, S. Kato, K. Wakasugi and T. Makihira, The MU radar with an active phased array system, 1. Antenna and power amplifiers, *Radio Sci.*, **20**, 1155–1168, 1985a.

Fukao, S., T. Tsuda, T. Sato, S. Kato, K. Wakasugi and T. Makihira, The MU radar with an active phased array system, 2. In-house equipment, *Radio Sci.*, **20**, 1169–1176, 1985b.

Gage, K. S., B. B. Balsley and R. Garello, Comparisons of horizontal and vertical velocity spectra in the mesosphere, stratosphere and troposphere: observations and theory, *Geophys. Res. Lett.*, **13**, 1125–1128, 1986.

Garrett, C., and W. Munk, Space-time scales of internal waves: A progress report, *J. Geophys. Res.*, **80**, 291–297, 1975.

Geller, M. A., Dynamics of the middle atmosphere, *Space Science Reviews*, **34**, 359–375, 1983.

Gille, J. C., and L. V. Lyjak, An overview of wave-mean flow interactions during the winter of 1978–79 derived from LIMS observations, *Dynamics of the Middle Atmosphere* (J. R. Holton and T. Matsuno, eds.), 289–306, Terr. Pub., Tokyo, 1984.

Hauchecorne, A., Observation par lidar et modelisation des echaouffments brusques et des ondes planetaires dans l'atmosphere moyenne, Ph. D. thesis, Paris University VI, 1983.

Hauchecorne, A., and M.-L. Chanin, A mid-latitude ground-based lidar study of stratospheric warmings and planetary wave propagation, *J. Atmos. Terr. Phys.*, **44**, 577–583, 1982.

Hines, C. O., Tropopausal mountain waves over Arecibo: a case study, *J. Atmos. Sci.*, **46**, 476–488, 1989.

Hines, C. O., The saturation of gravity waves in the middle atmosphere. Part I: Critique of linear-instability theory, *J. Atmos. Sci.*, **48**, 1348–1359, 1991a.

Hines, C. O., The saturation of gravity waves in the middle atmosphere. Part II: Development of Doppler-spread theory, *J. Atmos. Sci.*, **48**, 1360–1379, 1991b.

Hines, C. O., The saturation of gravity waves in the middle atmosphere. Part III: Formation of the turbopause and of turbulent layers beneath it, *J. Atmos. Sci.*, **48**, 1380–1385, 1991c.

Hirooka, T., K. Hayashi, and S. Yamada, Stratospheric Circulations of the Northern Hemisphere Winter during 1989–90, *J. Geomag. Geoelectr.*, **44**, 1097–1106, 1992.

Hirota, I., Climatology of gravity waves in the middle atmosphere, *J. Atmos. Terr. Phys.*, **46**, 767–773, 1984.

Hirota, I., and T. Niki, A statistical study of inertia-gravity waves in the middle atmosphere, *J. Meteorol. Soc. Japan*, **63**, 995–999, 1986.

Hodges, R. R.., Jr., Generation of turbulence in the upper atmosphere by internal gravity waves, *J. Geophys. Res.*, **72**, 3455–3458, 1967.

Holton, J. R., The role of gravity waves-induced drag and diffusion in the momentum budget of the mesosphere, *J. Atmos. Sci.*, *39*, 791-799, 1982.

Holton, J. R., and W. M. Wehrbein, A numerical model of the zonal circulation of the middle atmosphere, *Pure Appl. Geophys.*, **118**, 284-306, 1980.

Hyson, P., Wind finding data from radar tracking of high altitude sensors, *Q. J. Royal Meteorol. Soc.*, *94*, 592–597, 1968.

Iikura, Y., N. Sugimoto, Y. Sasano, and H. Shimizu, Improvement on lidar data processing for stratospheric aerosol measurements, *Appl. Opt.*, **26**, 5299–5306, 1987.

Jasperson, W. H., G. D. Nastrom, and D. C. Fritts, Further study of terrain effects on the mesoscale spectrum of atmospheric motions, *J. Atmos. Sci.*, **47**, 979–987, 1990.

Kitamura, Y. and I. Hirota, Small-scale disturbances in the lower stratosphere revealed by daily rawin sonde observations, *J. Meteorol. Soc. Japan*, **67**, 817-831, 1989.

Kanzawa, H., The behavior of mean zonal wind and planetary-scale disturbances in the troposphere and stratosphere during the 1973 sudden warming, *J. Meteorol. Soc. Japan*, *58*, 329–356, 1980.

Leovy, C., Radiative equilibrium of the mesosphere, *J. Atmos. Sci.*, **21**, 238–248, 1964a.

Leovy, C., Simple models of thermally driven mesospheric circulation, *J. Atmos. Sci.*, **21**, 327–341, 1964b.

Lindzen, R. S., Turbulence and stress due to gravity wave and tidal breakdown, *J. Geophys. Res.*, **86**, 9707-9714, 1981.

Manson, A. H., and C. E. Meek, Gravity wave propagation characteristics (60-120 km) as determined by the Saskatoon MF Radar (GRAVNET) system: 1983-85 at 52°N, 107°W, *J. Atmos. Sci.*, **45**, 932–946, 1988.

Maekawa, Y., S. Fukao, T. Sato, S. Kato, and R. F. Woodman, Internal inertia-gravity waves in the tropical lower stratosphere observed by the Arecibo radar, *J. Atmos. Sci.*, **41**, 2359–2367, 1984.

Matsuno, T., A quasi-one-dimensional model of the middle atmospheric circulation interacting with internal gravity waves, *J. Meteorol. Soc. Japan*, **60**, 215–226, 1982.

Matsuno, T., Dynamics of minor stratospheric warmings and "preconditioning", *Dynamics of the Middle Atmosphere* (J. R. Holton and T. Matsuno, eds.), 333–351, Terr. Pub., Tokyo, 1984.

Matsuno, T., and T. Shimazaki, *The Stratosphere and Mesosphere*, Lectures in Atmospheric Sciences: 3, Univ. Tokyo Press, 141–145, 241–255, 1981 (in Japanese).

Meek, C. E., I. M. Reid, and A. H. Manson, Observations of mesospheric wind velocities 2. Cross sections of power spectral density for 48-8 h, 8-1 h, 1 h-10 min over 60-110 km for 1981, *Radio Sci.*, **20**, 1383–1402, 1985.

Murayama, Y., T. Tsuda, M. Yamamoto, T. Nakamura, T. Sato, S. Kato, and S. Fukao, Dominant vertical scales of gravity waves in the middle atmosphere observed with the MU radar and rocketsondes, *J. Atmos. Terr. Phys.*, **54**, 339–346, 1992a.

Murayama, Y., K.-I. Oyama, T. Tsuda, H. Kanzawa, F. J. Schmidlin, M. Bittner, T. Nakamura, M. D. Yamanaka, S. Fukao, and S. Kato, Rocketsonde observations of the middle atmosphere dynamics at Uchinoura (31°N, 131°E) during the DYANA campaign. Part I: Outline of experiments and background conditions, *J. Geomag. Geoelectr.*, **44**, 995–1007, 1992b.

Murayama, Y., T. Tsuda, and S. Fukao, Seasonal variation of gravity wave activity in the lower atmosphere, *J. Geophys. Res.*, *submitted*, 1992c.

Murphy, D. J., Measurement of energy and momentum in the mesosphere, Ph. D. thesis, Dept. of physics and mathematical physics, University of Adelaide, 1990.

Miyahara, S., Y. Hayashi, and J. D. Mahlman, Interactions between Gravity Waves and Planetary-Scale Flow Simulated by the GFDL 'SKYHI" General Circulation Model, *J. Atmos. Sci.*, *43*, 1844-1861, 1986.

Nakamura, T., T. Tsuda, M. Yamamoto, S. Fukao, and S. Kato, Characteristics of gravity waves in the mesosphere observed with the MU radar, 1. Momentum flux, *J. Geophys. Res.*, *in press*, 1993a.

Nakamura, T., T. Tsuda, M. Yamamoto, S. Fukao, and S. Kato, Characteristics of gravity waves in the mesosphere observed with the MU radar, 2. Propagation direction, *J. Geophys. Res.*, *in press*, 1993b.

Nakane, H., S. Hayashida, Y. Sasano, N. Sugimoto, I. Matsui, and A. Minato, *J. Geomag. Geoelectr.*, **44**, 1071–1083, 1992a.

Nakane, H., S. Hayashida, I. Matsui, N. Sugimoto, A. Minato, and Y. Sasano, Lidar observation of ozone over Tsukuba (36°N, 140°E), *Proc. of the Quadrennial Ozone Symposium 1992 and tropospheric ozone workshop, in press*, 1992b.

Nastrom, G. D. and D. C. Fritts, Sources of mesoscale variability of gravity waves. Part I: Topographic excitation, *J. Atmos. Sci.*, **49**, 111–127, 1992.

Nastrom, G. D., D. C. Fritts, and K. S. Gage, An investigation of terrain effects on the mesoscale spectrum of atmospheric motions, *J. Atmos. Sci.*, **44**, 3087–3096, 1987.

Offermann, D., M. Bittner and F. J. Schmidlin, Falling sphere and datasonde experiments, *DYANA Campaign Handbook*, distributed by D. Offermann and M. Bittner, Physics Department, University of Wuppertal, FRG, 172pp., July, 1989.

Oyama, K.-I., Summary of Ground and Rocket Observations during the DYANA Campaign in Japan, available from Institute of Space and Astronautical Science, September 1991.

Oyama, K.-I., Activity overview in Japan during DYANA campaign, *J. Geomag. Geoelectr.*, **44**, 987–993, 1992.

Pinkel, R., On the use of Doppler sonar for internal wave measurements, *Deep Sea Res.*, **28 A**, 269–289, 1981.

Rastogi, P. K. and S. A. Bowhill, Gravity waves in the equatorial mesosphere, *J. Atmos. Terr. Phys.*, **38**, 51–60, 1976

Reid, I. M., Gravity wave motions in the upper middle atmosphere (60–110km), *J. Atmos. Terr. Phys.*, **48**, 1057–1072, 1986.

Sato, T and R. F. Woodman, Fine altitude resolution radar observations of upper-tropospheric and lower-stratospheric winds and waves, *J. Atmos. Sci.*, **39**, 2539–2545, 1982.

Scheffler, A. O. and C. H. Liu, The effects of Doppler shift on the gravity wave spectra observed by MST radar, *J. Atmos. Terr. Phys.*, **48**, 1225–1231, 1986.

Schmidlin, F. J., Rocket techniques used to measure the middle atmosphere, *MAP Handbook*, *19*, 1–28, 1986.

Schoeberl, M. R., and D. F. Strobel, The zonally averaged circulation of the middle atmosphere, *J. Atmos. Sci.*, **35**, 577–591, 1978

Senft, D. C., and C. S. Gardner, Seasonal variability of gravity wave activity and spectra in the mesopause region at Urbana, *J. Geophys. Res.*, **96**, 17229–17264, 1991.

Smith, S. A. and D. C. Fritts, Poker Flat MST radar and meteorological rocketsonde wind profile comparisons, *Geophys. Res. Lett.*, **11**, 538–540, 1984.

Smith, S. A., D. C. Fritts, and T. E. VanZandt, Comparison of mesospheric wind spectra with a gravity wave model, *Radio Sci.*, **20**, 1331–1338, 1985.

Smith, S. A., D. C. Fritts, and T. E. VanZandt, Evidence for a saturated spectrum of atmospheric gravity waves, *J. Atmos. Sci.*, *44*, 1404–1410, 1987.

Sugimoto, N., Y. Sasano, H. Nakane, S. Hayashida-Amano, I. Matsui, and A. Minato, Multiple wavelength lase radar for measuring the stratospheric and tropospheric ozone profiles, *Oyobutsuri*, **56**, 1385–1397, 1989 (in Japanese).

Stroud, W. G., W. Nordberg, W. R. Bandeen, F. L. Bartman,and P. Titus, Rocket-grenade measurements of temperatures and winds in the mesosphere over Churchill, Canada, *J. Geophys. Res.*, **65**, 2307–2323, 1960.

Tsuda, T., T. Inoue, D. C. Fritts, T. E. VanZandt, S. Kato, T. Sato, and S. Fukao, MST Radar Observations of a Saturated Gravity Wave Spectrum, *J. Atmos. Sci.*, *46*, 2440–2447, 1989.

Tsuda, T., S. Kato, T. Yokoi, T. Inoue, M. Yamamoto, T. E. VanZandt, S. Fukao, and T. Sato, Gravity waves in the mesosphere observed with the MU radar, *Radio Sci.*, **26**, 1005–1018, 1990a.

Tsuda, T., Y. Murayama, K.-I. Oyama, F. J. Schmidlin, M. Bittner, H. Kanzawa, T. Nakamura, M. D. Yamanaka, S. Fukao, and S. Kato, Rocketsonde observations of the middle atmosphere dynamics at Uchinoura (31°N, 131°E) during DYANA campaign. Part II: Characteristics of gravity waves, *J. Geomag. Geoelectr.*, **44**, 1009–1023, 1992a.

Tsuda, T., Y. Murayama, T. Nakamura, R. A. Vincent, A. H. Manson, C. E. Meek and R. L. Wilson, Variations of the gravity wave characteristics with height, season and latitude revealed by comparative observations, *J. Atmos. Terr. Phys.*, *in press*, 1992b.

Tsuda, T., Y. Murayama, M. Yamamoto, S. Kato, and S. Fukao, Seasonal variation of momentum flux in the mesosphere observed with the MU radar, *Geophys. Res. Lett.*, **17**, 725–728, 1990b.

Tsuda, T., T. E. VanZandt, M. Mizumoto, S. Kato and S. Fukao, Spectral analysis of temperature and Brunt-Bäisälä frequency fluctuations observed by radiosondes, *J. Geophys. Res.*, **96**, 17265–17278, 1991.

US standard atmosphere, 1976, U. S. Government Printing Office, Washington, D. C., 1976.

VanZandt, T. E., A universal spectrum of buoyancy waves in the atmosphere, *Geophys. Res. Lett.*, **9**, 575–578, 1982.

VanZandt, T. E., A model for gravity wave spectra observed by Doppler sounding system, *Radio Sci.*, **20**, 1323–1330, 1985.

VanZandt, T. E., and D. C. Fritts, A theory of enhanced saturation of the gravity wave spectrum due to increases in atmospheric stability, *Pure Appl. Geophys.*, *130*, 399–420, 1989.

VanZandt, T. E., G. D. Nastrom, and J. L. Green, Frequency spectra of vertical velocity from Flatland VHF radar data, *J. Geophys. Res.*, **96**, 2845–2855, 1991.

Vincent, R. A., Gravity wave motions in the mesosphere, *J. Atmos. Terr. Phys.*, **46**, 119–128, 1984

Vincent, R. A., and D. C. Fritts, A climatology of gravity wave motions in the mesopause region at Adelaide, Australia, *J. Atmos. Sci.*, **44**, 748–760, 1987.

Vincent, R. A., and I. M. Reid, HF Doppler Measurements of Mesospheric Gravity Wave Momentum Fluxes, *J. Atmos. Sci.*, *40*, 1321-1333, 1983.

Wherbein, W. M., and C. B. Leovy, An accurate radiative heating and cooling algorithm for use in a dynamical model of the middle atmosphere, *J. Atmos. Sci.*, **39**, 1532–1544, 1982.

Weinstock, J., Gravity waves saturation and eddy diffusion in the middle atmosphere, *J. Atmos. Terr. Phys.*, **46**, 1069–1082, 1984.

Weinstock, J., Saturated and unsaturated spectra of gravity waves and scale-dependent diffusion, *J. Atmos. Sci.*, **47**, 2211–2225, 1990.

Wilson, R., Climatologie des ondes de gravite dans l'atmosphere moyenne: observation par lidar Rayleigh et interpretation, Ph. D. thesis, Paris University VI, 1989.

Wilson, R., A. Hauchecorne, and M. L. Chanin, Gravity wave spectra in the middle atmosphere as observed by Rayleigh lidar, *Geophys. Res. Lett.*, **17**, 1585–1588, 1990.

Wilson, R., M. L. Chanin, and A. Hauchecorne, Gravity waves in the middle atmosphere observed by Rayleigh lidar: 1. Case studies, *J. Geophys. Res.*, **96**, 5153–5167, 1991a.

Wilson, R., M. L. Chanin, and A. Hauchecorne, Gravity waves in the middle atmosphere observed by Rayleigh lidar: 2. Climatology, *J. Geophys. Res.*, **96**, 5169–5183, 1991b.

Woodman, R. F. and A. Guillén, Radar observations of winds and turbulence in the stratosphere and mesosphere, *J. Atmos. Sci.*, **31**, 493–505, 1974.

Yamamoto, M., T. Tsuda and S. Kato, Gravity waves observed by the Kyoto meteor radar in 1983–1985, *J. Atmos. Terr. Phys.*, **48**, 597–603, 1986.

Yamamoto, M., T. Tsuda, S. Kato, T. Sato and S. Fukao, A saturated inertia gravity wave in the mesosphere observed by the MU radar, *J. Geophys. Res.*, **92**, 11993–11999, 1987.

Yamamoto, M., T. Sato, P. T. May, T. Tsuda, S. Fukao and S. Kato, Estimation error of spectral parameters of MST radars obtained by least squares fitting method and its lower bound, *Radio Sci.*, **23**, 1013–1021, 1988a.

Yamamoto, M., T. Tsuda, S. Kato, T. Sato and S. Fukao, Interpretation of the structure of mesospheric turbulence layers in terms of inertia gravity waves, *Physica Scripta*, **37**, 645–650, 1988b.

Publication List

1. Tsuda, T., Y. Murayama, M. Yamamoto, S. Kato, and S. Fukao, Seasonal variation of momentum flux in the mesosphere observed with the MU radar, *Geophys. Res. Lett.*, **17**, 725–728, 1990.

2. Murayama, Y., T. Tsuda, M. Yamamoto, T. Nakamura, T. Sato, S. Kato, and S. Fukao, Dominant vertical scales of gravity waves in the middle atmosphere observed with the MU radar and rocketsondes, *J. Atmos. Terr. Phys.*, **54**, 339–346, 1992.

3. Murayama, Y., K.-I. Oyama, T. Tsuda, H. Kanzawa, F. J. Schmidlin, M. Bittner, T. Nakamura, M. D. Yamanaka, S. Fukao, and S. Kato, Rocketsonde observations of the middle atmosphere dynamics at Uchinoura (31°N, 131°E) during the DYANA campaign. Part I: Outline of experiments and background conditions, *J. Geomag. Geoelectr.*, **44**, 995–1007, 1992.

4. Tsuda, T., Y. Murayama, K.-I. Oyama, F. J. Schmidlin, M. Bittner, H. Kanzawa, T. Nakamura, M. D. Yamanaka, S. Fukao, and S. Kato, Rocketsonde observations of the middle atmosphere dynamics at Uchinoura (31°N, 131°E) during DYANA campaign. Part II: Characteristics of gravity waves, *J. Geomag. Geoelectr.*, **44**, 1009–1023, 1992.

5. Tsuda, T., Y. Murayama, H. Wiryosumarto, S. Kato, S. W. B. Harijono, S. Fukao, M. Karmini, C. M. Mangan, S. Saraspriya, and A. Suripto, A preliminary report on radiosonde observations of the equatorial atmosphere dynamics over Indonesia, *J. Geomag. Geoelectr.*, **44**, 1041–1055, 1992.

6. T. Tsuda, Y. Murayama, T. Nakamura, R. A. Vincent, A. H. Manson, C. E. Meek and R. L. Wilson, Variations of the gravity wave characteristics with height, season and latitude revealed by comparative observations, *J. Atmos. Terr. Phys.*, *in press*, 1992.

7. Murayama, Y., T. Tsuda, and S. Fukao, Seasonal variation of gravity wave activity in the lower atmosphere, *J. Geophys. Res.*, *submitted*, 1992.